THE EFFECT OF AN AIRCRAFT FOREBODY ON THE PERFORMANCE OF A Y-DUCT INLET IN HIGH SUBSONIC FLOW.

L'INFLUENCE DU FUSELAGE AVANT SUR LA PERFORMANCE D'UNE TUYÈRE D'ADMISSION «Y» DANS UN ÉCOULEMENT A VITESSE SUBSONIQUE ÉLEVÉE.

A Thesis Submitted to the Division of Graduate Studies
of the Royal Military College of Canada
by

Benjamin Gilbart, BEng, *rmc*
Second Lieutenant

In Partial Fulfillment of the Requirements for the Degree of
Masters of Applied Science in Aeronautical Engineering

April, 2024

Acknowledgements

This work would not have been possible without the immense efforts of many individuals whom I will try to thank here. I would like to first thank my supervisor, Dr. Billy Allan. Dr. Allan has been a fantastic mentor from whom I have learned a lot over the past two years, both inside and out of the classroom. He has provided me with many amazing opportunities and his knowledge, advice, and outlook have always helped point me in the right direction. I also need to thank Dr. Asad Asghar for his extreme dedication and support through his guidance, expertise, and long hours of assistance whenever I needed help. There was not a single question I asked Dr. Asghar that he was unable to answer, or at least point me to resources that would be able to. His assistance, dedication, and time commitment to the experimental work ensured that it was completed on time and to a high standard.

The experimental campaign of this work would not have been possible without the technicians of the RMC Mechanical and Aerospace Engineering Laboratory. Their countless hours of designing, manufacturing, and providing technical insight made the campaign a success. I also would like to thank Mr. Ben Frosst and Conor Seetal for their help during the experimental campaign. Finally, I also would like to thank my parents, my friends, and my girlfriend Ryley for their tireless support, encouragement, and reminders that there is a world outside of school throughout my time as a graduate student. I would not have been able to do this without all of them and they deserve my sincere thanks and gratitude.

Abstract

Many single-engine jet aircraft use twin-scoop Y-duct inlets to route external air to an embedded gas turbine engine. Despite Y-ducts being common to many aircraft types, both present and historical, there exists a distinct lack of research into the influence of an aircraft forebody on their performance at high subsonic speeds. In this work, a representative double-offset Y-duct was designed for a slender body aircraft operating in the high subsonic regime. Two test articles were designed based on this duct and subsequently fabricated: the isolated Y-duct, and a representative air vehicle model integrating the Y-duct design. Angle-of-attack and yaw of the vehicle model were adjustable. Both test articles were tested in the RMC trisonic wind tunnel, the isolated Y-duct at Ma=0.80 and Ma=0.63, and the air vehicle at Ma=0.8. Both articles used different experimental setups. Static pressure measurements were made along four main meridians of the isolated Y-duct while total pressure and swirl data were also recorded at the duct exhaust. The embedded Y-duct allowed total pressure measurements to be taken at the duct exhaust to compare total pressure results with those of the isolated Y-duct. Without incidence and yaw angles on the model, the embedded duct experienced just over a 4% increase in total pressure loss compared to the isolated duct at Ma=0.63. The highest angle-of-attack investigated, 8°, was found to increase total pressure recovery 4.1% compared to no angle-of-attack or yaw. At 8° angle-of-attack and 4° yaw this increase was found to be 5.4% compared to 0° angle-of-attack and 4° yaw. No trends in traditional pressure distortion coefficients at the Y-duct exhaust were noted with angle-of-attack for both 0° and 4° yaw. Total pressure non-uniformity at the duct exhaust was found to increase at 4° yaw. The data acquired from the experimental test campaign highlighted the profound impact a forebody has on the performance of a Y-duct. This work provides a baseline for understanding these effects and also guidance for the design and implementation of Y-ducts in future high subsonic applications.

Résumé

De nombreux avions à réaction monomoteurs utilisent des entrées d'air en Y à deux bouches pour acheminer l'air extérieur vers la turbine à gaz intégré. Il existe un manque flagrant de recherche sur l'influence de l'avant-corps d'un aéronef sur les performances à des vitesses subsoniques élevées des conduits en Y, bien qu'ils soient communs à de nombreux types d'aéronefs, actuels et anciens. Dans ce travail, un conduit en Y à double bouches représentatif a été conçu pour un aéronef à corps élancé opérant en régime subsonique élevé. Deux articles d'essai ont été conçus sur la base de ce conduit et fabriqués par la suite : le conduit en Y isolé et un modèle de véhicule aérien représentatif intégrant la conception du conduit en Y. Les deux articles ont été testés dans la soufflerie trisonique du CMR, le conduit en Y isolé à $Ma = 0{,}8$ et $Ma = 0{,}63$, et le véhicule aérien à $Ma = 0{,}8$. Deux montages expérimentaux différents ont été utilisés pour chaque article. Des mesures de pression statique ont été effectuées le long des quatre méridiens principaux de la conduite en Y isolée, ainsi que la pression totale et le tourbillonnement ont été enregistrées à l'échappement cette conduite. Des mesures de pression totale à la sortie de la conduite en Y encastrée furent comparée aux résultats de la pression totale de la conduite en Y isolée. Le conduit encastré a connu une augmentation d'un peu plus de 4% de la perte de pression totale par rapport au conduit isolé à Ma=0,63 pour les essais sans angles d'attaque et de lacet. L'angle d'attaque le plus élevé étudié, soit 8°, montre une augmentation la récupération de la pression totale de 4,1% par rapport à celle sans angle d'attaque ou de lacet. Avec un angle d'attaque de 8° et un lacet de 4°, l'augmentation est de 5,4% par rapport à celle sans angle d'attaque et 4° de lacet. Aucune tendance dans les coefficients traditionnels de distorsion de la pression à l'échappement du conduit en Y n'a été observée en fonction de l'angle d'attaque, tant pour un angle d'attaque de 0° que pour un lacet de 4°. On a constaté que la non-uniformité de la pression totale à l'échappement du conduit augmentait à un angle d'attaque de 4°. Les données obtenues lors des essais expérimentaux ont mis en évidence l'impact profond de l'avant-corps sur les performances d'un conduit en Y. Ce travail

fournit une base pour la compréhension de l'impact d'un corps avant sur les performances du conduit. Ce travail fournit une base pour la compréhension de ces effets ainsi que des conseils pour la conception et la mise en œuvre des conduits en Y dans les futures applications subsoniques élevées.

Contents

List of Tables

List of Figures

Nomenclature

Latin

$Æ$	Aspect ratio [-]
C_p	Coefficient of pressure [-]
D	Exit diameter [in]
$DC(60)$	Distortion coefficient [-]
$DPCP$	Circumferential distortion descriptor [-]
$DPRP$	Radial distortion descriptor [-]
i	radial coefficient [-]
k	circumferential coefficient [-]
p	Pressure [Pa]
R	Ratio of duct parameters [-]
r	radius [m]
SD	Swirl directivity [-]
SI	Swirl intensity [-]
SP	Swirl pairs [-]
SS	Average swirl angle [°]
u	Axial velocity [$\frac{\mathrm{m}}{\mathrm{s}}$]
v	Secondary velocity [$\frac{\mathrm{m}}{\mathrm{s}}$]
x	Axial distance [m]

Greek

α	Swirl angle [°]
δ	Uncertainty [-]
$\overline{\gamma}$	Time and area-averaged pressure loss coefficient [-]

$\overline{\pi}$ Time and area-averaged pressure recovery coefficient [-]

θ Azimuth angle [°]

Acronyms

3-D Three dimensional

AIP Aerodynamic interface plane

AoA Angle-of-attack

ASME American Society of Mechanical Engineers

CRV Counter rotating vortice

csv Comma seperated value

DRDC Defence Research and Development Canada

RMC Royal Military College of Canada

SAE Society of Automotive Engineers

Dimensionless groups

Re Reynolds number, [-]

Ma Mach Number, [-]

Superscripts and subscripts

$+$ Positive direction

$-$ Negative direction

0 Time-averaged total value

1 Inlet entrance condition

2 Inlet exhaust condition

ave Averaged

max Maximum

θ Circumferential

h Horizontal

i Annulus counter

j 60° Sector counter

k Sector of annulus counter

LD Length-to-diameter

m Number of annulus sectors

OD	Offset-to-diameter
OL	Offset-to-length
S	Swirl
s	Static
V	Vertical

1 Introduction

Y-duct inlets are a type of intake commonly used in aircraft configurations that feature a single embedded gas turbine engine. These twin-scoop designs have two limbs converging into a single duct, leading to the engine face. The design of these inlets is specific to their application, but they are often offset in at least one direction, as well as cross-sectional area increased to diffuse the flow to acceptable engine conditions. An example of a Y-duct inlet is shown in Fig. 1.1.

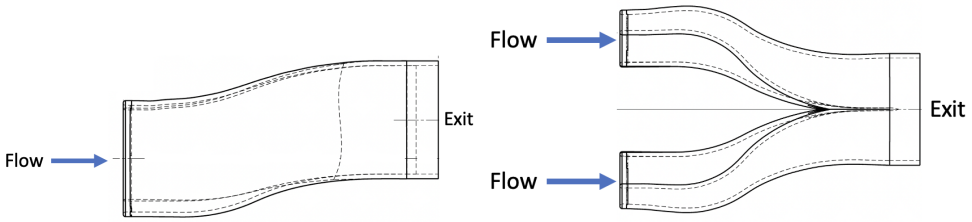

(a) Side View. (b) Top View.

Figure 1.1: Schematic View of a Y-duct.

Aerospace applications of this duct type are plentiful, with most being used in military type aircraft. The design of a Y-duct can be optimized for internal aircraft configurations, allowing for better use of internal space resulting in increased manœuvrability and decreased cross-sectional area, and hence drag of an aircraft. Figure 1.2 shows two aircraft that use Y-duct intakes, the Canadair CT-114 Tutor and the Lockheed Martin F-35 Lightning II.

(a) CT-114 Tutor [6]. (b) F-35 Lightning II [7].

Figure 1.2: Aircraft With Y-duct Intakes.

Both aircraft have cheek intake entrances adjacent to their canopies that converge into a single duct within the aircraft, feeding air to the centreline embedded gas turbine engine. Figure 1.2a highlights the two degrees of offset featured in the Tutor's Y-duct intake. Flow is directed both upwards and towards the centreline of the aircraft, where the turbojet engine is located. The effect of offsets and flow diffusion within Y-ducts can cause adverse flow conditions to develop in the duct, such as separated flow, secondary flows, and pressure distortion. Flow turning in the duct is known to cause the creation of Dean vortices, first noted in 1928 [8] this phenomena is sketched in Fig. 1.3.

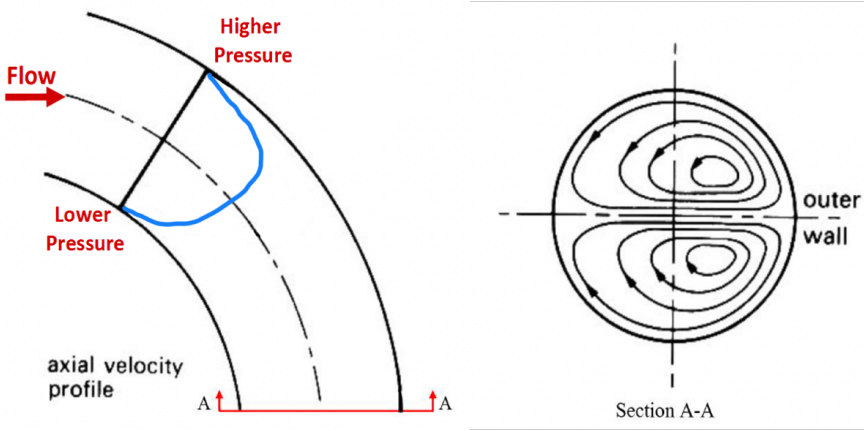

(a) Side View. (b) Streamwise View.

Figure 1.3: Flow Turning in a Duct. Adapted From [1].

The turning of flow within a duct causes increased pressure on the outer radius of the turn and decreased pressure on the inner radius in order to balance the centrifugal acceleration of the turning flow. The change in local static pressure reduces flow velocity near the outer radius while increasing it near the inner. As the flow navigates the turn, the inertia of the core flow forces it towards the outer radius of the turn. This causes flow to recirculate circumferentially towards the lower pressure region at the inner radius as shown in Fig. 1.3b. The development of these secondary flows can lead to local swirl at the engine face, which itself can cause deteriorated engine conditions [9]. Local adverse pressure gradients from the combination of offset and area diffusion can also lead to flow separation in the duct. The presence of separated flow can cause subsequent unequal distributions of total pressure, or *distortion*, at the face of the engine resulting in reduced engine performance and stall margin, and increased mechanical stress on gas turbine engines [10]. It is desirable to mitigate these flow features as much as possible.

Y-duct intakes first garnered interest in 1948 based on the work by Davis and Goldstein [11]. Their work determined that a twin scoop intake had higher pressure recovery than an annular intake of the same area. Martin and Holzhauser [12] determined that the individual limbs of a Y-duct performed similarly to those of an isolated S-duct, but their performance was particularly susceptible to asymmetric flow at the inlet, such as yaw of an aircraft in flight. Since those early days, Y-ducts have been successfully applied to many aircraft types; nevertheless, there is a notable gap in the open literature regarding their performance. The available literature will be thoroughly discussed in Chapter 2. Of note, very little research focused on the high subsonic performance of Y-duct intakes, and even less into the effect of a forebody on the performance of Y-duct inlets. Considering this is the domain where most Y-duct applications are used, the lack of available information in open literature is surprising and merits further investigation.

1.1 Research Motivations

Y-ducts are almost always integrated within an aircraft's fuselage, located some distance downstream from the nose. The upstream forebody has an influence on the performance of the duct. Some previous work on the effect of a forebody on the performance of a Y-duct intake is available in the open literature. Initial supersonic work by Stroud investigated different aircraft nose shapes and found a link between increased nose finesse and pressure recovery

[13]. Incompressible numerical work completed at intake speeds corresponding to low Reynolds numbers by Saha *et al.* [14] investigated the effect on the performance of a yawed Y-duct in the presence of a simple forebody. That work found that increasing yaw angle increased pressure distortion and non-uniformity at the engine face. There exists a large gap in relevant academic work in the high subsonic regime either on isolated Y-ducts or for those embedded within a fuselage. The motivation behind this work is to investigate the performance of an isolated Y-duct design in a high subsonic flow, and the same Y-duct embedded within a representative aircraft fuselage. This work aims to be a baseline that presents performance differences between the same Y-duct in both an isolated and embedded configurations. Furthermore, the influence of vehicle angle-of-attack and yaw on inlet performance will be evaluated.

1.2 Scope, Research Goals, and Objectives

This thesis reports experimental testing of two Y-ducts of the same design: one isolated duct and one duct embedded within the fuselage of a representative high subsonic air vehicle. The results compare total pressure recovery, loss, and distortion for both ducts. Two different inlet entrance Mach numbers were investigated for the isolated Y-duct: 0.8 and 0.63, while the air vehicle was tested in a freestream of Ma=0.8. Swirl and static pressure data were obtained for the isolated Y-duct and compared between the two entrance Mach numbers. Total pressure was measured at the aerodynamic interface plane (AIP) of the Y-duct to better understand the flow behaviour and effect of the entrance Mach number at the engine face.

There are two main goals of this thesis: First, to compare the performance of the isolated duct with that of the vehicle-embedded duct with zero incidence or yaw angle. This assessed the baseline effects of a forebody on performance. The second goal was to vary the angles of attack and yaw on the air vehicle with embedded Y-duct to further understand the effects of a forebody in operationally representative flight conditions. The overall experimental objectives are as follows:

- To design, fabricate, and test the isolated Y-duct inlet at Ma=0.80 and at Ma=0.63.
- To design and manufacture an internal aerodynamics model incorporating the Y-duct.
- To design and construct a suitable test section for the internal aerodynamics model.
- To test the internal aerodynamics model with Y-duct integrated at Ma=0.8.

1.3 Thesis Outline

This thesis is divided into six chapters. The next chapter, Chapter 2, discusses and highlights relevant academic work in the field of Y-duct intakes, including inlet performance, Y-duct design parameters, and external effects on performance. Chapter 3 discusses the methods and practices used in the experimental campaign, including the design and construction of the test articles. Chapter 4 compares and discuss the findings and results of this work. Respectively, Chapters 5 and 6 conclude key findings from the work completed, and present recommendations for future work on this topic.

2 Literature Review

Since the beginning of the jet age, aircraft propulsion technology has required new and refined solutions for air intake integration to support advances in aircraft speed, manœuvrability and stealth. Y-duct inlets have proven to be a popular choice especially in military aviation applications due to their versatility and aerodynamic performance. A comprehensive literature review of current and historical aerospace intake research has been conducted, focusing on topics such as inlet performance parameters, secondary flows, flow control, geometric design parameters, and external effects such as angle-of-attack or yaw. This section analyzes and synthesizes the relevant literature on these subjects and their relation to Y-duct inlets in order to set the stage for the work conducted in this thesis.

2.1 Aircraft Design

Aircraft have many different and widely varying design configurations depending on their intended role. Military fighter aircraft necessitate design philosophies suited to their unique roles which require high manœuvrability and performance with a low radar cross section. In order to fulfill these requirements, the majority of aircraft mass needs to be concentrated close to the centre of gravity to mitigate the structural effects of high manœuvre loads and to promote a smaller overall footprint. Cruise missiles are further constrained by platform integration which imposes strict size limitations. These factors all necessitate maximum use of internal space.

In order to meet design requirements, oftentimes one or multiple gas turbine engines are embedded within the fuselage of the aircraft. This allows for a concentrated centralized aircraft mass while also offsetting compressor and fan blades from incoming radar waves, reducing aircraft detectability. While this design choice will improve the desired performance parameters of this aircraft type, it will also lead to new aerodynamic considerations consistent

with an embedded and offset gas turbine engine. In order to understand fully the requirements of an inlet to bring external air to an internal engine, it is necessary to understand the intake requirements of a gas turbine engine first.

2.1.1 Gas Turbine Engines

Gas turbine engines are mostly used in aircraft for thrust production. These engines use the surrounding ambient air as a working fluid in order to propel an aircraft. Gas turbine engines function through four successive processes: intake, compression, combustion, and expansion. The first stage of this process, intake, is relevant to the work within this thesis and will be discussed thoroughly in the following sections of this literature review.

Compressor performance of a gas turbine engine is highly sensitive to the flow quality at the exit of the air-intake duct [15]. The primary purpose of the intake process is to provide a steady mass flow rate of external air at required speeds and quantity to the compressor face of the engine, referred to as the *aerodynamic interface plane* (AIP), with minimal distortion and loss of total pressure. Modern day gas turbine engines have relatively fewer compressor stages, and consequently high pressure ratios per stage. This makes their performance more sensitive to flow changes [16]. Pressure distortion at the compressor face is closely tied to compressor stalls [17] and also leads to uneven loading on fan blades leading to potential damage over time and a decreased lifetime of mechanical parts. It is imperative that an aircraft's intake system is designed to meet the engine performance requirements whilst also maximizing use of available internal space.

2.1.2 Inlets

The primary purpose of an engine inlet on a high speed aircraft is to deliver freestream flow to a gas turbine engine. During high speed flight the inlet works to raise the freestream enthalpy at the compressor face to conditions required by the engine [18]. Different engine and inlet combinations may be particularly susceptible to compatibility problems that can lead to problems such as engine surge or fan vibrations thus it is important for an aircraft inlet to be properly designed for its intended use. Two main categories of inlets exist depending on the intended flight speeds of the aircraft: supersonic or subsonic.

Subsonic inlets encompass a variety of designs depending on application and may even be implemented following a supersonic inlet depending on the requirements of the engine and airframe. This research is focused on subsonic

inlets suited for aircraft with embedded engines. Modern military aircraft designs feature radar and other equipment within the nose of an aircraft, making pitot inlets, such as that of the *North American F-86 Sabre* impractical from a modern design standpoint. Instead offset inlets are of particular interest. They make maximum use of space usually introducing offsets in one or more directions in order to bring oncoming airflow to an embedded engine. Of these offset inlets two are commonly used within modern aerospace applications: S-duct and Y-duct inlets.

S-Duct Inlets

S-ducts are a common offset inlet type comprising two reversing bends coupled with an offset in at least one direction. Their sigmoid like shape often resembles the letter 'S', hence the name. These ducts have the added benefit of diffusing air over a shorter distance due to the offset. S-ducts have a wide application in the aerospace industry; used in the *General Dynamics F-16*, *Dassault Falcon 900EX*, and the *General Dynamics Tomahawk* missile. Unlike straight diffuser inlets, S-ducts must simultaneously turn and diffuse the flow to the required engine conditions. The centreline curvature of an S-duct can oftentimes lead to significant secondary flows within the duct. This, combined with the decreasing flow velocity, increases the risk of flow separation [19]. Nevertheless, S-duct inlets remain a popular choice in aerospace applications due to their simplicity and relatively good performance.

Y-Duct Inlets

Y-duct inlets, sometimes referred to as bifurcated or *twin scoop* inlets, consist of two merging S-ducts symmetrical about a centreline, forming a singular duct in the shape of the letter 'Y'. The advantages of Y ducts were initially determined by Davis and Goldstein in 1948 [11]. Using an experimental setup at Mach numbers between 1.36 and 2.01, they found that the twin scoop Y-duct inlet displayed an approximately 10% higher pressure recovery at the AIP than what was achievable for an annular inlet of the same inlet area. Since then Y-duct inlets have been employed on many aircraft types such as the Canadair CT-114 Tutor, the Lockheed Martin F-35 Lightning II, the Saab JAS 39 Gripen, and more recently the Boeing T-7 Red Hawk.

Since Y-ducts are composed of two symmetrical S-ducts, their performance is closely linked to that of S-ducts. The major difference between the two comes with the flow mixing after their convergence to a single duct. In 1949 Martin and Holzhauser [12] experimental work compared twin and single scoop

inlet performance, as part of an integrated fuselage system for an aircraft in low subsonic Mach numbers. They concluded that each intake on the twin intake setup demonstrated similar pressure recovery performance before the merging plane. They also noted that unlike S-ducts, Y-ducts were susceptible to unstable flow regimes when experiencing asymmetric mass flow. This is discussed further in Section 2.4.2 of this chapter. In order to investigate Y-duct inlets properly, it is imperative to understand first how the duct performance is quantified.

2.2 Inlet Performance

Ideally an embedded engine would receive perfectly undisturbed, high pressure flow at the required inlet velocity and mass flow rate. Unfortunately, due to inlet geometry, flow turning, viscosity, and external conditions, performance will never be ideal. Given the purpose and applications of Y-duct and S-duct inlets, they must feature an offset and turning angle over which the flow is redirected from its initial free-stream direction to that of a near parallel but offset axis at the engine face. As flow navigates a bend, it must accelerate along the inner radii before again decelerating. This causes the formation of an adverse pressure gradient which can cause the flow near the wall to separate due to the decreased momentum associated with the developed boundary layer. The effect of area diffusion in a duct can amplify this adverse pressure gradient leading to larger regions of separated flow. This separation is detailed in Fig. 2.1.

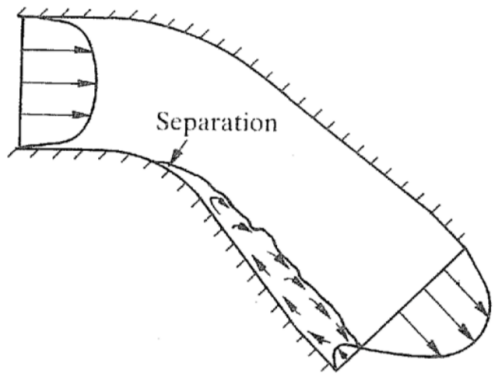

Figure 2.1: Flow Separation Following a Bend in a Duct With Area Diffusion [2].

The effect of flow turning also leads to a higher pressure on the outer radius and lower pressure on the inner due to the centrifugal acceleration of the flow. This causes flow re-circulation and secondary flows to form within the duct. This phenomenon is further discussed and explained in Section 2.2.3. The remainder of this section will discuss the parameters used to quantify inlet duct performance. The equations used to calculate these performance metrics are given in Chapter 3.

2.2.1 Pressure Recovery

Ideally 100% of the total pressure from the freestream would be present at the AIP. This would promote efficient compressor operation as well as optimum combustion within the engine. Due to viscous effects however, all inlet types will experience losses in total pressure. The ratio of the area-averaged total pressure to the free stream total pressure at the compressor face is called the *total pressure recovery* [20]. The coefficient of pressure loss refers to the loss of total pressure between the free stream conditions and the AIP, non-dimensionalized with the former. Variations in total pressure across the AIP are quantified in terms of *distortion* which will be discussed in a further section.

As flow is diffused, its static pressure will increase. This is quantified by the coefficient of static pressure recovery. Pressure recovery in an inlet depends on a range of factors, including the shape, aircraft speed, and the airflow demands of the engine which influence the flow speed through the intake.

The combination of bends and adverse axial pressure gradient caused by diffusion in S-ducts (and consequentially Y-ducts) can lead to adverse flow conditions such as separation and flow reversal. Early work conducted by Martin and Holzauser [21] generally found that for a given Y-duct setup, any flow instability and reversal experienced at low velocity ratios (*i.e.* the ratio of inlet velocity to freestream velocity) are functions of the static pressure recovery of the duct but have no relation to total pressure recovery.

2.2.2 Distortion

Flow distortion refers to the spatial non-uniformity of time-averaged total pressure values measured at the AIP [22]. For compression system such as one of a gas turbine engine, distorted inflow results in reduced aerodynamic performance, reduced stall margin, and increased blade mechanical stress levels [10]. It is impossible to completely eliminate distortion within a duct since as a minimum, a boundary layer will always be present reducing total pressure

recovery. Distortion is commonly quantified by different coefficients which denote the non-dimensional non-uniformity in a flow. These coefficients are presented in detail in Section. 3.3.

2.2.3 Swirl

Swirl is an undesirable condition relating to flow direction at the AIP. The Society of Automotive Engineers (SAE) defines swirl as the circumferential component of the flow angularity defined as the deviation of the local velocity vector from a vector normal to the AIP [23]. Swirl stems almost exclusively from aircraft configurations that require an offset engine and inlet [22]. Furthermore, it has been shown that an intake without the use of inlet guide vanes will have swirl at the engine face [9].

Two types of intake swirl are commonly found at the AIP: *bulk and twin swirl*. Bulk swirl is defined as a rotation of the entire inlet flow field in one direction about the rotational axis of the compressor. If bulk swirl is in the same direction as the compressor rotation it is referred to as co-rotating bulk swirl. That opposite to the compressor rotation is counter-rotating bulk swirl [23]. Twin swirl (sometimes referred to as *paired* swirl), is a condition defined by the presence of two vortices with equal magnitudes and opposite senses of rotation. However, offset swirl pairs can form from two vortices with opposite rotation senses but different magnitudes [23]. Twin swirl commonly develops in the first bend of an offset inlet, as the result of interaction between the centrifugal pressure gradient and a low energy region associated with flow separation at the inner radius [22]. This phenomenon is well understood with its historic roots in curved pipe work completed by Dean in 1927 [8].

When researching the intake ducts of the *Panavia Tornado* aircraft, Aulhela [9] found that both bulk and twin swirl are common in offset intakes. Bulk swirl can be mitigated simply with inlet guide vanes, however, twin swirl is a steady phenomenon and can only be moderately attenuated with such devices. Additionally, Aulhela concluded that engines without inlet guide vanes were particularly sensitive to bulk swirl when that swirl was contra rotational to the direction of compressor rotation. This combination can lead to problems such as engine surge and forced blade vibration [9]. The discussion in this section provide a foundation and baseline for the performance evaluations completed on the Y-ducts in this thesis. The performance metrics discussed in this section are further quantified in Section 3.3.

2.3 Y-duct Inlet Design Parameters

The performance of a Y-duct layout is highly dependent on its geometry. This geometry is defined by several parameters including, offset-to-length ratio, turning angle, area diffusion ratio and duct shaping. These geometric parameters can affect flow separation, swirl, pressure recovery, and distortion among other flow characteristics. The effect of inlet design parameters on flow performance is discussed in the following sections.

2.3.1 Offset and turning angle

In Y or S-ducts, offsets can lead to flow separation following the inner radius of a turn. There has been extensive published work on the topic of offset and turning angle, summarized in this section in order to appreciate better their influences on inlet performance.

In 2004 Bharani *et al.* [24] investigated the effect of varying turning angles in the horizontal plane for a Y-duct at an inlet entrance velocity of 130 ft/s corresponding to a Reynolds number of 1.25×10^5. They discovered that pressure recovery at the AIP was a function of the turning angle of the flow, with lower pressure recovery being observed for varying area diffusion ratios with increasing turning angle. Of all the angles tested, a turning angle of 22.5/22.5° was found to give the best performance at the AIP. Conversely 45/45° delivered the lowest performance at the AIP, also displaying drastically changed pattern of non-axial flow compared to ducts with lower turning angles, due to increased curvature and flow diffusion. At the AIP of ducts with lower turning angles, a number of vortices were observed that seemed to break into a large number of pairs.

In 2007, Gopaliya *et al.* [25] completed numerical work for an S-duct with a 90/90°turning angles, with varying offset at three Reynolds numbers between 1.37×10^5 and 5.48×10^5. Five different offsets were investigated between 0 and 1.25 outlet diameters. It was discovered that increasing the offset of the duct led to an approximate 12.1% decrease in pressure recovery for the most extreme offset case, compared to the no-offset case. A 32% increase in the non-uniformity index, which denotes the percentage of non axial flows at the AIP, was noted for the maximum offset compared to the no-offset case.

Further work in 2008 by Singh *et al.* [26] who numerically investigated the effect of offset in two perpendicular directions on the performance of a Y-duct at very low Reynolds numbers of 6.85×10^4. A Y-duct inlet with two semi-

elliptical entrances oriented with their major axis in the vertical direction was investigated with varying vertical turning angles of 15/15°, 22.5/22.5°, and 30/30° with a constant horizontal turning angle of 22.5/22.5°. The formation of two pairs of counter-rotating vortices was noted at the merging plane, with their intensity decreasing as the AIP was approached. The vortex intensity was greater than that noted in a single offset Y-duct. They concluded that Y-duct performance deteriorates significantly with vertical offsets, and recommended vertical offsets not exceeding 15/15° should be used wherever possible.

Continuing his research in 2010, Gopaliya *et al.* [27] investigated the effect of combined vertical and horizontal offset of an S-duct inlet with a 90/90° turning angle at a Reynolds number of 1.37×10^5. The vertical offset of their duct was held constant while horizontal offsets were varied from $0.25B$, $0.5B$, $0.75B$ to $1B$ where B was the diameter of the circular inlet entrance. It was found that increasing the vertical offset led to decreasing pressure recovery at the AIP, on the order of a 14% decrease for a rectangular inlet entrance (oriented with its major axis in the vertical direction), where offset was defined by the width of the entrance, and a 7.3% decrease for a semi-circular entrance transitioning to a rectangular exit where offset was defined by entrance diameter. Decreased flow uniformity was also seen in ducts with increases in vertical offsets.

In 2011 Anand and Sandeep [16] used the commercial CFD program *FLUENT* to predict the flow performance at the AIP for 3 different Y-ducts, all with an inlet Reynolds number of 1×10^5, the same curvilinear length and area ratio, and with different turning angles of 15/15, 22.5/22.5° and 30/30°. The results were similar to those found by Bharani *et al.* [24] in 2004 for an S-duct inlet: for smaller turning angles, the AIP flow was more uniform. As the turning angle of the flow increased, the coefficient of static pressure recovery was found to decrease, with coefficient of static pressure loss increasing.

In 2018, Asghar *et al.* [28] conducted transonic experimental work on the effect of offset-to-length ratio of a rectangular-to-circular S-duct inlet, for Mach numbers of 0.8 and 0.85. They found that pressure losses at the AIP increased for increasing offset-to-length ratio for both Mach numbers investigated, it was also noted that there was no link between radial distortion and offset-to-length ratio, however a clear link was observed for circumferential distortion.

2.3.2 Area Diffusion Ratio

For high speed flight in order to prepare incoming air to the conditions required by the engine, the flow must be diffused. The action of diffusing trades kinetic energy for enthalpy causing an increase in both static pressure and temperature. The adverse pressure gradient thereby formed in the duct can lead to flow separation and other undesirable phenomena such as swirl. Bharani *et al.* [24] investigated identical Y-duct designs, varying the area diffusion ratio between 2 and 3 and turning angles between 22.5/22.5° and 45/45°. It was found that for all turn angles, the larger area ratio led to higher static pressure recovery at the AIP, while maintaining similar pressure loss coefficients. For a duct with 22.5/22.5° turning angles, the two area diffusion ratios showed similar overall flow patterns at the AIP, with lower velocity magnitudes for the higher area ratio duct. Unfortunately, there are not many openly published studies on the effects of area diffusion ratio on Y-duct performance.

2.3.3 Inlet Entrance Shaping

Although all Y-ducts in aerospace propulsion applications will have a circular exits to match with the engine face, the intake entrance of both Y-duct limbs can vary greatly in shape. The effect of inlet shaping on duct performance have been well researched, and noticeable links have been found between the two.

In 2007 Saha *et al.* [29] investigated the effect of inlet entrance shape for S-duct inlets with turning angles of 22.5/22.5° at an inlet Mach of 0.173. Five different inlet shapes were investigated: elliptical, semi-circular, oval, rectangular, and square, all with an area diffusion ratio of two. It was found that inlet entrance shapes with round corners displayed the highest flow uniformity at the AIP, while entrances with sharp corners displayed the lowest. Secondary flows also followed the same trend, with the square shapes producing the strongest secondary flows. It was found that elliptical inlet entrance shapes gave the best flow uniformity in terms of total pressure distortion: $DC(60)$ was 0.032, with the square shape giving the worst $DC(60)$ of 0.149. Total pressure losses of 4.13% were the greatest for the square entrance shape with semi-circular having the lowest, at 3.79%. The semi-circular inlet provided the highest static pressure recovery and lowest coefficient of static pressure loss.

In 2008, Signh *et al.* [18] found similar result to those of Saha *et al.* [29]: the rounding of inlet entrance corners significantly improved the AIP flow characteristics of a double offset Y-duct. Singh investigated a Y-duct with

horizontal turning angles of 22.5/22.5° and vertical turning angles of 15/15°. Beginning with a traditional semi-circular inlet entrance shape, the corners were gradually rounded to asses the effects. As corner radius increased, flow reversal decreased, eventually disappearing completely. Static pressure recovery was noted to increase almost 20% between the baseline and most rounded entrance while total pressure decreased by approximately 6%. Flow uniformity also increased with rounding, with a decrease in $DC(60)$.

These results were corroborated by Gopaliya *et al.* [27] in 2010 who found that semi-circular duct entrances displayed reduced pressure recovery loss at the AIP compared to those of a rectangular entrance. They also found that non-uniformity increased from approximately 12% for a duct with no vertical offset, to 32% for a duct with a vertical offset equivalent to the outlet width of the rectangular cross section. The non-uniformity index of the duct with the circular cross section was found to increase from just 6.4% with no vertical offset, to 21% for a vertical offset equivalent to the diameter at the duct exit.

Asghar *et al.* [30] experimentally investigated the effect of inlet entrance aspect ratio on duct performance for Y-duct inlets at high subsonic Mach numbers. A relation between aspect ratio and pressure recovery was observed with increasing aspect ratio, leading to increased pressure recovery. This was likely due to the greater flow diffusion in the vertical plane. No clear trends were noted with aspect ratio and total pressure recovery. The radial distortion increased with aspect ratio. However, despite marginal changes to circumferential distortion, no clear trend could be established.

In 2023 Gilbart *et al.* [4] tested S-ducts at high subsonic Mach numbers to compare the effect of entrance cross-sectional area on performance. It was noted that $DC(60)$ at 0.35 was greater for the S-duct with a circular entrance compared to the 0.29 calculated for the S-duct with a rectangular entrance signifying less distortion with the latter entrance shaping. The rectangular entrance duct displayed higher bulk swirl, at 10°, than did the circular entrance duct at 5°. The circular entrance was found to exhibit higher total pressure losses at 5.5%, compared to the 3.7% observed for the S-duct with the rectangular entrance. The circular entrance duct was noted to have larger regions of separated flow compared to the rectangular entrance duct.

Merging ducts

Unlike an S-duct, Y-ducts feature a converging section where the two limbs meet. The merging of flow from each branch of a Y-duct leads to a unique flow

pattern at the AIP, so it is important to investigate it further. Very complex flows can form when a yaw angle is introduced, mass flow rates from each limb are not equal, or both conditions are present. Research in this topic is summarized in later portions of this literature review.

Bharani *et al.* [24] investigated the flow distribution at the AIP for Y-ducts. It was found that the relatively undisturbed core flow commonly noted at the AIP of S-ducts, remained distinct at the AIP of the Y-duct. Instead of merging into a single flow at the joining of the two Y-duct limbs, the two zones of undisturbed flow persisted on their respective sides of the AIP. Numerical work done by Patel *et al.* [31] on Y-ducts noted these same flow patterns for their work on Y-ducts over a range of inlet velocities.

These results were further validated by Singh *et al.* [15] in 2013. Using an experimental Y-duct setup with an average inlet Reynolds number of 6.85×10^4, separation bubbles were observed at the inflection plane of the bends in both limbs of the Y-ducts. Despite the separated flow, two distinct flow regimes were apparent at the AIP: A central core flow with high velocity featuring a nearly uniform pair of vortices surrounded by reasonably uniform flow with velocity decreasing towards the outer walls. The separation bubbles observed at the inflection planes of the limbs upstream had disappeared.

The design geometry of Y-duct intakes is seen to have a profound influence on their performance. The Y-duct design used in this thesis was a carefully modified design based on a duct tested by Sidhu *et al.* [32]. The baseline design was modified in order to improve pressure recovery and increase its entrance speed based on the findings in the literature. The design is detailed in Section 3.2.1.

2.4 External effects

While Y-ducts are designed for certain design point conditions, these conditions will not always be present in operation. In real operations, external factors such as intake Mach number, angle-of-attack, yaw, and the presence of forebodes will influence Y-duct inlet performance. This section discusses the effects of these external factors.

2.4.1 Free stream Mach number

Y-ducts installed in aircraft will be subject to a wide range of freestream velocities which influence, in part, the speed of airflow through the inlet. It is

important to understand the effects of varying inlet speeds, and consequently mass flow rates, may have on the performance of a duct. In his work, Raymer [33] states as a baseline, that an inlet exposed to a Ma=0.8 flow may only encounter Ma=0.6 at the entrance. This highlights the effect of area blockage and loss in a freestream and is pertinent for results obtained in this work.

In 2004 Patel *et al.* [31] investigated the effect of multiple free stream velocities of 30 m/s, 60 m/s, and 90 m/s on the performance of a Y-duct with a single axis offset with a rectangular entrance as well as with a circular exit. They concluded from their work that there was no link between increasing Reynolds number (from increasing velocity) and the coefficient of static pressure recovery or total pressure loss for the range tested.

In 2008, further numerical work was completed at low Mach numbers corresponding to incompressible conditions by Singh *et al.* [26]. A Y-duct with both 22.5/22.5° horizontal and vertical turning angles was evaluated at Reynolds numbers ranging from 4.45×10^4 to 4.05×10^5. It was concluded that Reynolds number had no noteworthy effect on duct performance. The results for the highest Reynolds number had a 5% lower static pressure recovery, a 3% increase in total pressure loss, and no notable change in $DC(60)$.

In their incompressible numerical work on low subsonic Y-ducts in 2008, Singh *et al.* [26] supported these findings, discovering very little change in pressure distortion at the AIP for Reynolds numbers between 4.5×10^4 and 1×10^5. They were able to conclude that the Reynolds number has no significant effect on flow uniformity at the AIP. Asghar *et al* [28] compared different S-duct offset ratios at inlet Mach numbers of 0.8 and 0.85. Notwithstanding, this narrow Mach range, the variation in performance (static pressure recovery, total pressure loss, and radial and circumferential distortion descriptors) was imperceptible.

There is a gap in published research that exists for Y-duct performance at high subsonic Mach numbers. The majority of work has been completed for very low subsonic Mach numbers or for Mach numbers greater than 1.2. Very little work is openly available for Mach numbers in between, other than work done at the Royal Military College of Canada on S-ducts by Rider *et al.* [1] and Asghar *et al.* [28, 30, 34].

2.4.2 Angle-of-attack and sideslip

During aircraft manœuvres, a Y-duct may be subject to angles of incidence which cause non-uniform flow within the duct. This section will focus solely on the effects of angle-of-attack and sideslip, which were defined by their deviation from the normal vector originating from the AIP surface with the duct oriented horizontally. A subsequent section will discuss the forebody effects. Triantafyllou *et al.* [10] completed numerical work on the effects of angles-of-attack and sideslip on the pressure recovery and distortion at the AIP of an S-duct for varying Mach numbers. They found that, in general, maximum radial intensity decreased with both increasing angles-of-attack and sideslip. They also noted that increasing the angle of sideslip (while keeping angle-of-attack constant) increased the maximum circumferential distortion intensity, regardless of inlet Mach number.

In 2009 Ibrahim *et al.* [35] used numerical methods to compare the effects of Mach number, angle-of-attack, and sideslip angle on flow quality at the AIP of an S-duct inlet with no forebody. They found that varying the angle-of-attack had the greatest influences on flow distortion. Saha *et al.* [14] computationally investigated the effects of angle-of-attack between 0° and 30° on a Y-duct inlet that featured offset in the horizontal direction and semi-elliptical inlet entrances. Strong secondary flows were noted at the AIP as angle-of-attack was increased. These flows formed from both the upstream curvature of the duct as well as the transverse pressure gradient caused by the angle-of-attack. Angle-of-attack was also found to decrease coefficient of static pressure recovery at the AIP. Total pressure losses were found to increase modestly with increasing angles-of-attack between 0° and 20° with larger increases measured between 20° and 30°. $DC(60)$ increased over 400% between 0° and 30° angle-of-attack.

2.4.3 Effects of a Forebody

The presence of a forebody and its interaction with a Y-duct inlet is of particular interest to the work completed here. In real Y-duct applications, the duct itself is usually part way along an aircraft's fuselage, suggesting that its performance will be heavily influenced by the presence of the forebody. Depending on its installation, the boundary layer build-up on a forebody can greatly influence Y-duct performance. A forebody can also affect the mass flow into either or both limbs of a Y-duct, generating non-uniform asymmetrical flow regimes leading to performance degradations. So with asymmetric operation, it is expected that the flow at the AIP will experience high distortion and low pressure recovery [20].

Stroud [13] completed in an early attempt in 1952 to determine the feasibility of the implementation of twin scoop (Y-duct) inlets on high speed aircraft. They focused on the installation of a Y-duct on a forebody, as well as the influence of the forebody bluntness on Y-duct performance. They determined that a very blunt forebody with a relatively low finesse ratio led to great reductions in maximum pressure recovery and mass flow ratio of the duct, while contributing to large increases in drag, when compared to a less blunt configuration with a higher finesse ratio.

In 1956 Lazzeroni and Pfyl [36] investigated the effects of using boundary layer diverters and varying inlet lip geometry in order to improve the performance of a Y-duct fuselage combination. They found that, in general, a boundary layer diverter removed all boundary layer before it entered the inlet and led to higher propulsive thrust and larger ranges in steady inlet operations. This is compared to drawing the boundary layer off through a permeable surface. The diverter also had less radial and circumferential total pressure distortion at the AIP. They also found that a blunt entrance lip design on the Y-duct had considerably higher-pressure recovery compared to thin and sharp lip inlets at low subsonic speeds, but these had marginal gains at high subsonic and supersonic speeds.

In numerical work done by Patel *et al.* [31], the effect of a forebody was simulated by skewing the axial velocity between the two limbs. This work used the CFD code *FLUENT* to simulate a single offset Y-duct inlet with turning angles of 22.5/22.5°. It was found that the performance of the Y-duct decreased with increases in skewness of the inlet velocity profile. The duct receiving less mass flow rate had significantly lower pressure recovery and much higher total pressure losses. Its performance was also more closely linked to Reynolds number than the un-skewed duct. At the AIP, non-symmetric secondary flows are formed with strength proportional to increasing skewness.

Building on this work, in 2017 Saha *et al.* [37] completed a computational study into the effects of yaw angle on the performance of a Y-duct system featuring a single direction offset in the presence of a forebody. They investigated the effects of yaw angles between 0° and 30° assuming incompressible flow with an inlet Reynolds number of 2.67×10^5. Their results follow trends noted previously. For 0° yaw the AIP of the Y-duct was found to have a $DC(60)$ of 0.4224. $DC(60)$ was observed to increase with yaw with a maximum $DC(60)$ of 0.9128 being observed at 30° yaw. Their results also showed that non-uniformity of the flow at the AIP increased steeply with yaw angle,

with a consequent reduction in static pressure recovery and an increase in total pressure loss. The pressure recovery in the blanked leeward branch of the duct was noted as being lower than that of the windward side due to the blockage from the forebody. Understanding duct performance as influenced by external factors is a key topic pertaining to the work conducted in this thesis. Work such as by Patel *et al.* [31] and Saha *et al.* [37] are particularly useful in understanding the yawed performance of a Y-duct much like what is undertaken in this thesis.

This literature review summarized and synthesized important topics and ideas related to Y-duct inlets and their performance. The literature examined has provided a foundation on the understanding of Y-ducts and their implementation in aircraft, performance quantification, and the influence of a yaw angle and forebodies on duct performance, all of which are essential topics for the work completed in this thesis. Although there is a great deal of published literature on Y-ducts, a noticeable gap exists in experimental research on forebody effects, as well as on high subsonic inlet Mach numbers. The present work aims to push the knowledge of forebody effects further while also helping to fill in the gap in research for high subsonic Mach numbers through experimental Y-duct testing. The Y-duct used in this research was designed based on guidance from the literature reviewed here and on experimental work completed at RMC by Sidhu *et al.* [32].

3 Experimental Method

This chapter details the configuration of the laboratory, test articles, and associated subsystems used for the testing and evaluation of Y-ducts to determine the performance influence of yaw, angle-of-attack, and fuselage forebody.

3.1 Wind Tunnel

The RMC polysonic wind tunnel is a vacuum indraft tunnel, a configuration that uses a sealed low pressure vacuum tank downstream of the test section. When the seal holding the pressure differential between the tanks and the test section is rapidly opened, an airflow is induced through the test section, drawing in atmospheric air from the laboratory. The setup at RMC used three large external vacuum tanks with an approximate volume of 6000 US gallon (22,712.5 L). A top-view sketch of the wind tunnel setup is shown in Figure 3.1.

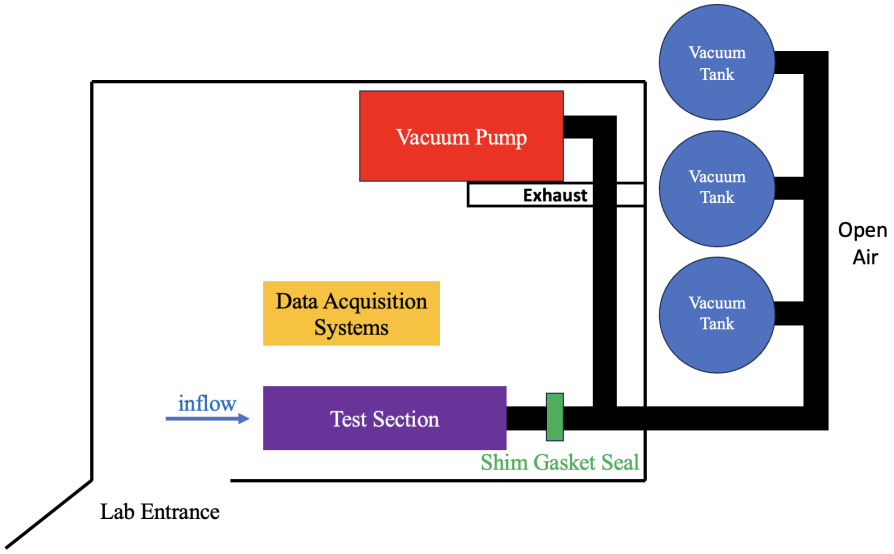

Figure 3.1: Top View of the Wind Tunnel Equipment.

The vacuum tanks were evacuated to -25 inHg (-84.66 kPa) gauge pressure for the isolated Y-duct testing and to -23 inHg (-77.88 kPa) for the internal aerodynamic testing. These pressures allowed for about 3 seconds of continuous steady state run time for the isolated Y-duct and 1 second of continuous run for the internal aerodynamics model. Air was evacuated from the tanks using a 30 Hp *Gardner Denver* electric vacuum pump capable of moving 840 m^3 of air per hour. The tanks were sealed from the test section using a round shim made from heavy gasket paper. This shim held the pressure differential between the vacuum tanks and atmospheric laboratory air. Both test articles were installed upstream of the shim, but configurations differed for the isolated Y-duct and internal aerodynamics model, as detailed later in this section. The airflow was initiated manually using a long metal rod to puncture the shim, allowing atmospheric air to flow through the test section into the vacuum tanks. All tunnel components were thoroughly secured to mitigate vibrations associated with the violence of the test initiation.

3.2 Test Sections

Specifically two major test articles were needed in this work: the isolated Y-duct model, used to find baseline data, and the internal aerodynamics model, used to investigate the effects of forebody interference on Y-duct performance.

Both were tested using the same wind tunnel, set at the required Mach numbers although with different experimental setups.

3.2.1 Isolated Y-duct

The isolated Y-duct was tested by drawing air directly through the Y-duct at an inlet entrance speed of Ma=0.8 and Ma=0.63. It consisted of several components in sequence including the Y-duct model, a straight duct section which held the 5-hole pressure probe data acquisition device on a linear traverse, and an adjustable iris valve, all attached directly to the exhaust duct of the indraft wind tunnel, as shown in Figure 3.2. Here the isolated Y-duct itself is the test section. Note that this figure is oriented so that flow is moving from right to left.

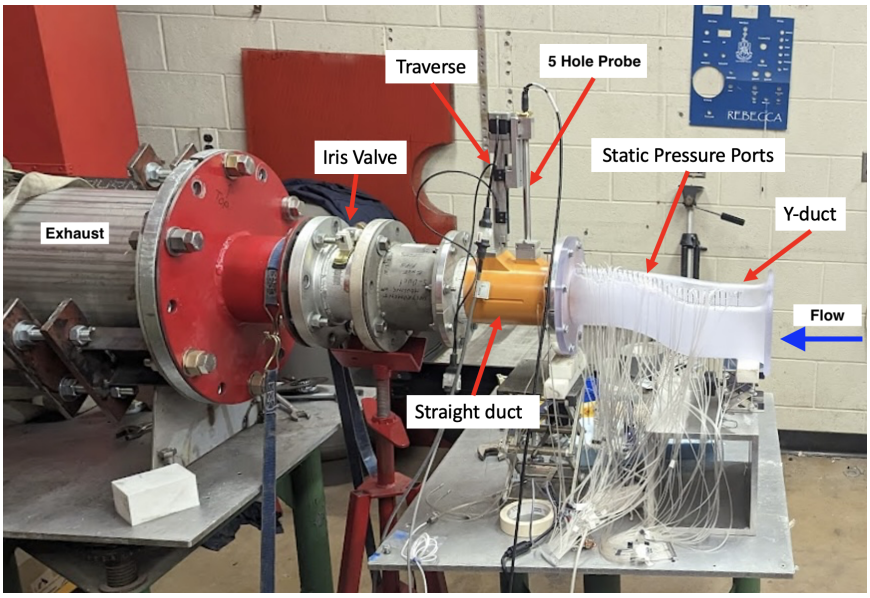

Figure 3.2: Isolated Y-Duct Installed [3].

The flow rate through the test section was controlled using the adjustable iris valve, designed and manufactured at RMC. This device allowed for fine adjustments of the choked throat area, limiting mass flow in the test section and consequently the speed of the airflow at the inlet entrance. A straight section of ducting with the same diameter as the Y-duct exit was situated downstream of the test section and just upstream of the iris valve housing the 5-hole *Aeroprobe* data acquisition system and linear traverse.

The linear traverse mechanism allowed the *Aeroprobe* to move from the wall of the straight duct to the centre. The traverse moved at approximately 0.67 in/s (0.017 m/s) during a run which resulted in negligible change in local flow angle. The *Aeroprobe* measured total pressure and all three components of velocity and featured transducers mounted on the probe itself. The entire section could be manually rotated in 30° increments, allowing the *Aeroprobe* to collect data discretely across the entire AIP.

Isolated Y-Duct Test Section

The isolated Y-duct model was manufactured using stereolithography (SLA) 3-D printing. Shown schematically in Fig. 3.3, it measured 15.3 in (0.38 m) long, and had an exit diameter of 4 in (0.101 m). The isolated Y-duct model featured a bellmouth entrance to compensate for the lack of ram pressure during testing and to allow air to enter smoothly into the inlet the design of which was based on ASME guidelines [38].

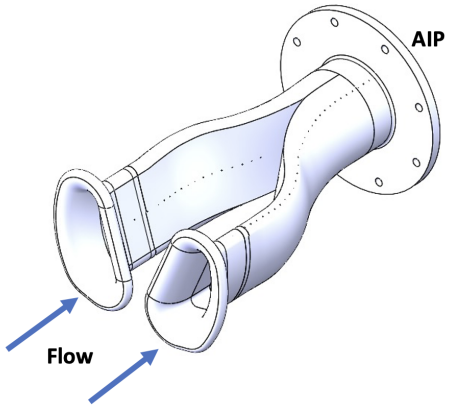

Figure 3.3: The Isolated Y-Duct Model.

The duct was designed as a representative twin-scoop Y-duct applicable for example, to a narrow fuselage air vehicles such as a cruise missile. The design was based on on previous Y-duct wind tunnel testing completed at RMC by Sidhu *et al.* [32] modified to improve performance. Design modifications to this baseline duct were aimed at increasing pressure recovery, decreasing distortion and increasing the inlet entrance operating speeds. A schematic of the duct is shown in Fig. 3.4 with key geometric parameters of this duct summarized in Table 3.1.

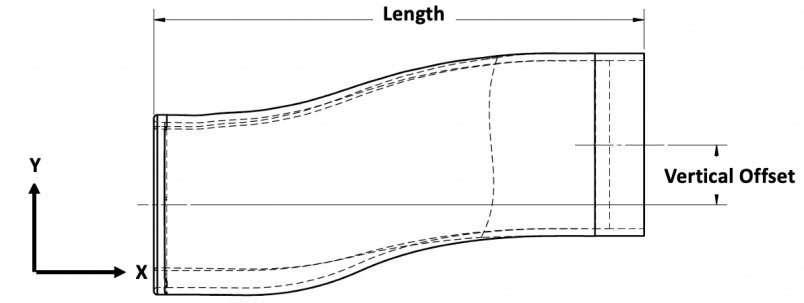

(a) Side View.

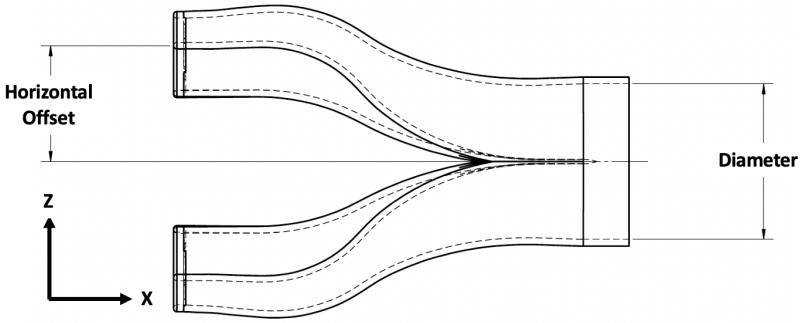

(b) Top View.

Figure 3.4: Isolated Y-Duct.

Table 3.1: Y-Duct Geometric Parameters.

Parameter	Symbol	Value
Exit Diameter	D	4 in
Area Diffusion Ratio	$\not{R}$	1.53
Length-to-Diameter Ratio	R_{LD}	2.93
Vertical Offset-to-Diameter Ratio	R_{OD_V}	0.358
Horizontal Offset-to-Diameter Ratio	R_{OD_h}	0.7455
Vertical Offset-to-Length Ratio	R_{OL_V}	0.122
Horizontal Offset-to-Length Ratio	R_{OL_h}	0.254

Static Pressure Measurements: Isolated Y-duct

The Y-duct model had a line of static pressure taps along each major offset meridian used to observe flow behaviour streamwise along the limbs of the duct. Looking downstream in Fig 3.3, the left limb featured 31 static pressure ports on the upper and lower surfaces while the right limb contained 31 ports on the outer and 17 on the inner surface which ended at the convergence of the two limbs. These ports were drilled through the wall material, then metal tube liners were inserted and fixed in place using epoxy. The tube ends were flush with the inside surface of the duct.

Flexible plastic tubing was attached to the metal tubes, connected to a 64-port *Scanivalve* MPS4264 15 psi differential (psid) pressure scanner. Prior to each test, the scanner was zeroed to ensure accurate static pressure data. Just before a run began, data acquisition at 200 Hz was triggered for a set number of data points, corresponding to a recording duration longer than the length of the run. This sample rate was chosen as it allowed for a proper statistical average to be made. The sample rate of data corresponded to approximately 300 - 400 steady state data points recorded over run duration. Data were obtained in a CSV file using *Scanivalve's* web-based data acquisition software and then averaged for the steady state run time. Static pressure data from the first pressure tap at the bellmouth of the inlet were used to calculate the entrance Mach number. Adjustments to the iris valve were sometimes required, using data from the *Scanivalve* to achieve the desired inlet Mach number of 0.8 $\pm$0.005. Due to the number of static pressure ports along the isolated Y-duct, a minimum of two runs were required to obtain static pressure data along all four meridians.

5-Hole Probe Pressure Measurements

The total pressure and velocity at the AIP were measured using a custom made 5-hole *Aeroprobe* ER-FRP. The tip of the 5-hole *Aeroprobe* was situated at the AIP of the 4-in diameter duct. The probe measured static and total pressure as well as the vector components of velocity. Data from this probe were used to evaluate the total pressure recovery, pressure distortion, and swirl performance of the duct. The probe was fixed to a linear traverse that moved from approximately 2 mm inboard from the outer wall to the centre of the AIP, triggered when a drop in pressure was detected coincident with -7 psi (-48.26 kPa) gauge pressure. The total transit was approximately 2 in (0.0508 m), a path traversed at 0.67 in/s (0.017 m/s). This speed resulted in a negligible

change in local flow angle for the probe corresponding to ± 0.05% of the local angle-of-attack. The *Aeroprobe* began recording data as it traversed from the wall of the straight duct to the centre. The azimuth angle of the *Aeroprobe* was manually adjusted in 30° increments between runs to survey the entire AIP discretely. Twelve runs were required to obtain data for the entire AIP. The probe featured a nose tip offset 90° from the main shaft, allowing it to face into the airflow with the probe inserted radially in the duct. The probe details and a schematic are given in Appendix B.

The tip of the probe featured five offset holes which, in combination, measured both the static and total pressure of the airflow. The probe measurements taken at 10 kHz were transferred to the *AeroFlow2* software that converted it into pressure and the x, y, and z components of the local velocity vector.

Y-Duct Data Processing

Data obtained from the *Scanivalve* device were processed directly from the output of the CSV file. They were averaged and used to plot variations in static pressure coefficient, C_p, along each limb of the duct. Data collected from the *Aeroprobe* system were noisy and required smoothing using a Savitzky-Golay filter before further processing. The smoothed data were imported into a program written in *MATLAB* from Rider [1] available in Appendix C. Data collected during the radial traverse were averaged into 20 radial data points, with each point being an average of 1500 discrete data points. The program first averaged the data points from each of the 12 azimuth angles with respect to area. The data from each azimuth angle were then compiled and contour plots for both velocity and total pressure distortion were created for the entire AIP. Flow performance metrics were also calculated using a *MATLAB* program from Rider [1], further explained in Section 3.3.

3.2.2 Internal Aerodynamics Model

In order to determine the influence of a forebody on a Y-duct performance, a separate test apparatus was constructed. This included three main components: the model, the model stand, and a new wind tunnel test section. The model was created as a representative gas turbine powered air vehicle incorporating the same Y-duct as the isolated Y-duct described in Section 3.2.1. The model was attached to a steel stand and housed within a rectangular wind tunnel test section. Unlike the isolated Y-duct where airflow was only through

the duct itself, in this configuration the entire model was immersed in the uniform airflow. An option existed to throttle the flow through the Y-duct by advancing a conical plug from the aft end. This was not used in this work.

Total pressure and limited static pressure instrumentation were incorporated in the internal aerodynamics model as discussed in Section 3.2.2. The model was cantilevered from its base with adjustable angle-of-attack and yaw. The support was attached to both the bottom plate of the test section and also to the table below, transferring aerodynamic loads to these structures as shown in Figure 3.5. Note the flow in this figure goes from right to left.

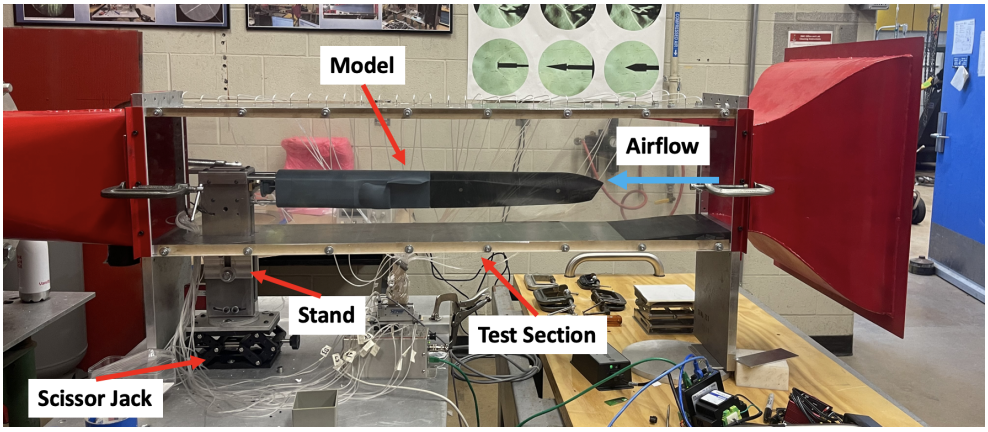

Figure 3.5: Internal Aerodynamics Test Section.

The test section for the internal aerodynamics model was rectangular in shape, measured 48 inches long, 8 inches wide, and 10.5 inches high and was adapted from another supersonic test section used at RMC. The structure was fabricated from aluminum except the sides which were clear acrylic panels. The top plate was 3/4 in thick with static pressure taps every 1.5 inches along the centreline of the model itself. These were used to measure the average freestream Mach number over the model.

The bottom plate had a 6.5 in diameter circular cutout at the downstream end that featured two rectangular slots to accommodate the support structure of the model stand and a 1.5 in rectangular cutout for plastic tubing. The round plate was designed to rotate $\pm 4^\circ$ to vary the yaw angle of the model. The slots for the vertical supports of the model stand were longer than required and the pivot was below the bottom plate of the test section so that angle-of-attack could be varied. During runs, voids in these slots was sealed using

duct tape. A collar on the underside of the round plate could be tightened to the model stand, securing it and transferring some of the aerodynamic load during a test run. Due to the baseline area blockage in the test section, no iris plate was required to achieve an average freestream of Ma=0.8 over the model.

Model Stand

The model stand, shown in Fig. 3.6, was machined from steel with the model itself attached in a cantilevered fashion. The stand consisted of two vertical rectangular support beams fixed to curved pivot hinges at the base and to the collar of the test section. The upstream side of these support beams were faired to limit the effects of flow separation on area blockage in the test section. The stand was fixed at its base to a *Thorlabs* scissor jack bolted to a steel table. The scissor jack height was adjusted to keep the model approximately 3 in above the test section floor to minimize the stands effect on area blockage while keeping the model clear of any wall effects. The model's angle-of-attack could be varied between -4° and 8° using the curved pivot hinges. Both angle-of-attack and yaw were adjusted manually and verified using a digital inclinometer. Each pivot could be bolted securely in place.

The top of the stand contained a brass support bearing that aligned a centre rod attached to the total pressure rake located at the AIP of the internal aerodynamics model as shown in Fig. 3.6. The index angle on the pressure rake was manually adjusted between runs on 15° increments. The index angle was set using an angle indicator located on the downstream side of an alignment cone. A set screw through the top of the brass bearing plate was used to lock the rod in place during runs.

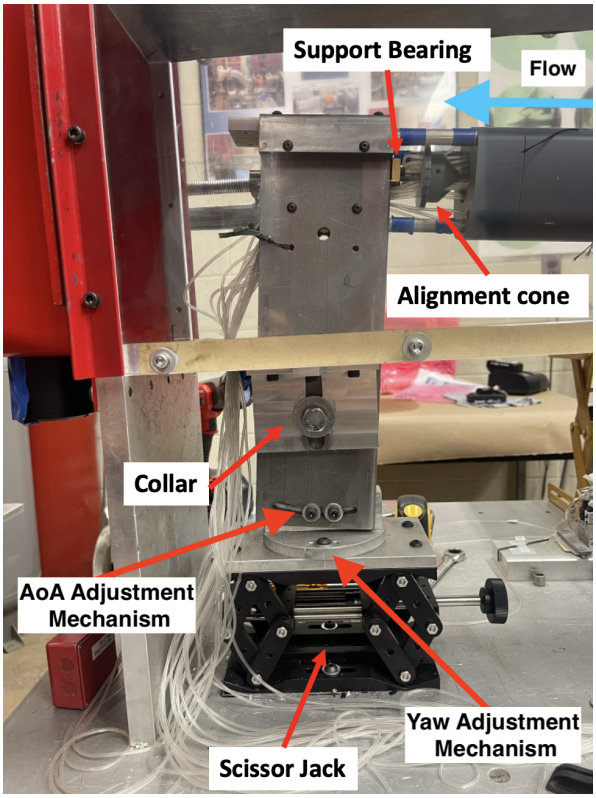

Figure 3.6: Internal Aerodynamics Model Stand.

Test Article

The internal aerodynamics model was conceived as a modern cruise missile powered by a gas turbine engine. The model had a high wing with a cambered airfoil. The aft end of the model featured four tail fins in a cruciform pattern each aligned 45° from the horizontal. The fuselage of the model was trapezoidal in shape and was designed to act as a lifting body. The nose was characterized by a twin faceted downward looking dome with a faired upper portion. The twin-scoop Y-duct inlets were situated just downstream and below the main wing. A CAD image of the model design is shown in Figure 3.7.

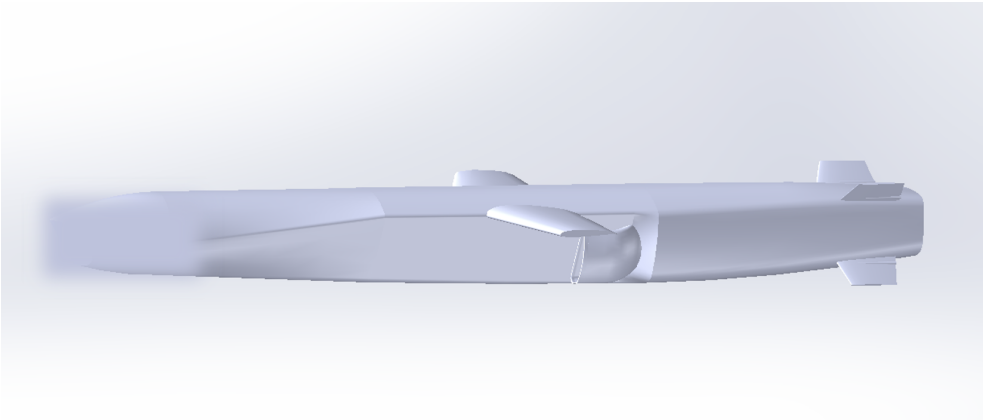

Figure 3.7: The Air Vehicle Design.

The design of the cruise missile was adapted to allow for aerodynamic performance measurements of the embedded Y-duct inlet. The test article kept the forebody upstream of the inlet entrance unmodified. The wings of the model were slightly clipped in order to fit within the test section and to allow yaw without wall interference. This was acceptable since the model was not being used for external aerodynamic testing. At the exit of the internal Y-duct, the missile body was truncated. At this point a 3-in section was added which extended the internal duct to standardize the flow quality measuring point between the *Aeroprobe* in the isolated Y-duct and the total pressure rake of the internal aerodynamics model. This section contained two opposing static pressure ports. The sections of the model downstream of the leading edge of the wing were printed using SLA of *Acura Bluestone* material, due to its high strength and surface finish. The nose section upstream of the wing was printed using fused deposition modeling (FDM) with ASA plastic due to its lower weight. The surfaces were sanded to an excellent surface finish using 600-grit sandpaper. The model was printed in five separate parts which were later fastened together. The test model measured 28.47 in long, 5.5 in wide, and 3.33 in tall at the thickest point. A schematic is shown in Fig. 3.8.

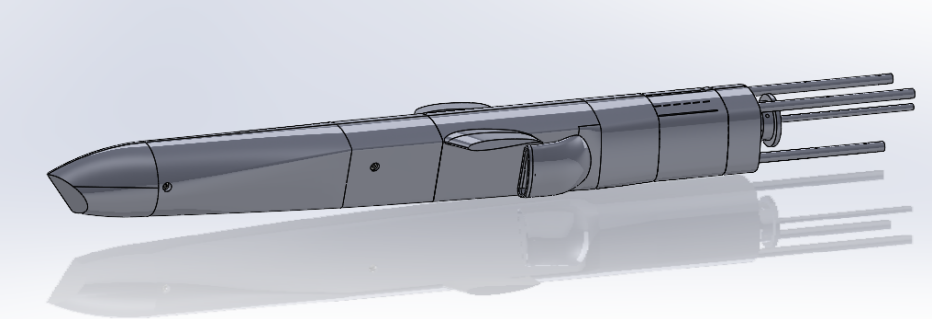

Figure 3.8: Isolated Internal Aerodynamics Model.

In the upper section of the support, three steel structural rods extended forward into the models core. The model itself contained a structural skeleton consisting of steel and aluminum rods attached to the 3-D printed ASA plastic core. The structural steel rods fixed the model to the support, transferring aerodynamic loads to the support and the steel table below. The internal structure is shown in Fig. 3.9 with steel components in blue, aluminum in green and the 3-D printed core in red. Note this figure is oriented so that flow goes from right to left.

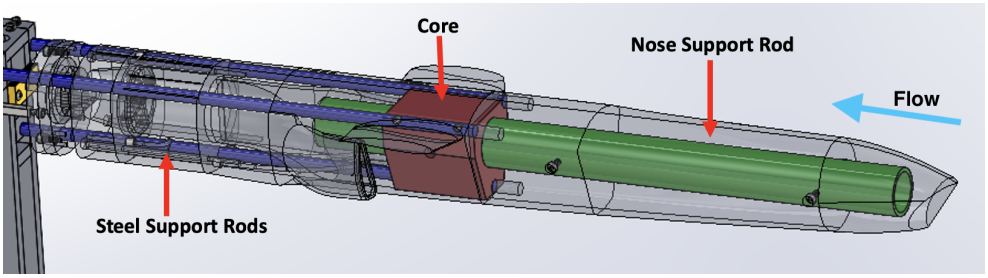

Figure 3.9: The Internal Structure of the Model.

Just downstream of the AIP of the embedded Y-duct, a cruciform shaped pressure rake was installed with four aluminum Pitot tubes with an inner diameter of 0.8 mm on each arm. A front-on view of the installed internal pressure rake is shown in Fig. 3.10b. These probes extended one inch upstream to be aligned with the AIP. Two static pressure ports were placed just upstream of this pressure rake to measure the airspeed at the AIP. The pressure rake itself was attached to a steel rod and locked in place using a set screw in a support bearing on the model's support. The index of the pressure rake was manually adjusted on 15° increments to create a discrete total pressure map at the AIP over the course of six runs.

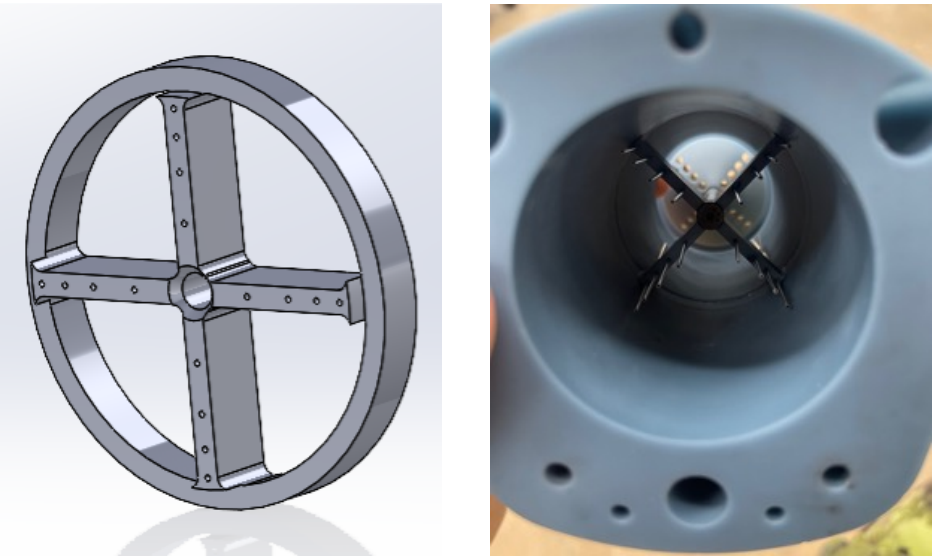

(a) Isolated Pressure Frame. (b) Installed Pressure Rake at the AIP.

Figure 3.10: The Internal Aerodynamics Model Total Pressure Rake.

Total pressure measurement from the 16 ports in this rake were recorded using an attached *Scanivalve* DSA3217 10 pisd pressure scanner. Flexible Tygon pressure lines of equal length were passed through the model stand and out through the bottom of the test section to the pressure scanner. The steady state run time of the tunnel was longer than the settling time of the system allowing for adequate steady state pressure data to be recorded.

Total Pressure Measurements: Internal Aerodynamics Model

Each total pressure tap was positioned in the centre of one of four equal-area concentric rings comprising the AIP for subsequent performance calculations detailed presently in Section 3.3. Before testing began, the software *DSALINK2* was opened and the scanner was zeroed. Data were recorded at 500 Hz for each run and exported as a CSV file. Between runs the model orientation was adjusted for the same index angle to be recorded for all combinations of angle-of-attack and yaw. Once complete, the pressure rake was manually indexed by 15°. Due to its shape, only six index angles were required in order to obtain a discrete scan of the entire AIP.

Static Pressure Measurements: Internal Aerodynamics Model

Static pressure taps were drilled at four locations on the internal aerodynamics model and along the top surface of the test section. Here 31 pressure taps spaced at 1.5 in intervals recorded axial velocity streamwise along the test section. The total pressure for these velocity calculations was assumed to be the atmospheric pressure in the lab. On the model, two static pressure ports were placed just downstream of the entrance on the inner surface of the inlet, one of which is annotated in Fig. 3.11a. These ports allowed airspeed calculation at the inlet entrance. Finally, two static pressure ports were located within the internal duct in line with the total pressure probes, one of which is shown in Fig. 3.11b.

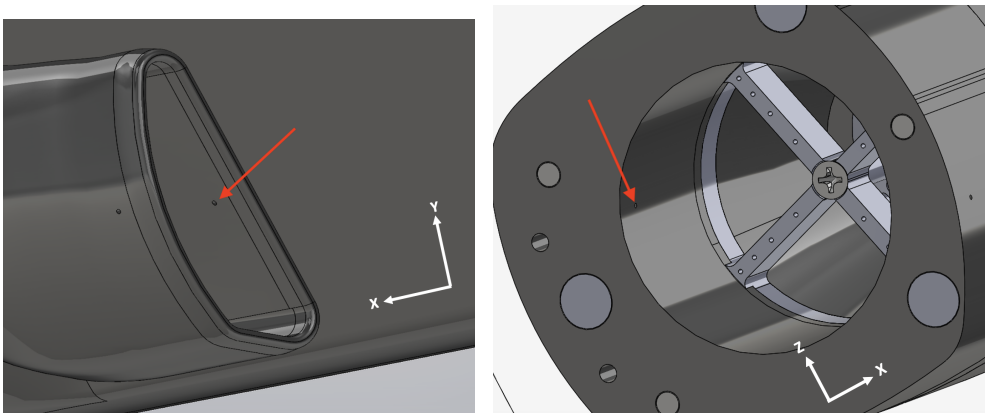

(a) At Inlet. (b) At AIP.

Figure 3.11: Static Pressure Ports in the Model.

All static pressure measurements for the model were recorded using a 64-port *Scanivalve* MPS4264 15 psid pressure scanner. Typically, an average of 200 steady state data points were recorded during a run. Static pressure data were exported directly as a CSV file, with the *Scanivalve* software converting voltage to pressure units using predefined calibrations.

Internal Aerodynamics Data Processing

Static pressure data from the *Scanivalve* MPS4264 did not require any post-processing. Steady state data points from the exported CSV file were averaged in time before calculating local airspeeds. Total pressure data recorded by the *Scanivalve* DSA3217 scanner were processed using a *Python* program that took the six individual data files from each of the pressure rakes indices between 0°

and 90° (allowing for the entire AIP to be mapped discretely). Total pressure contour plots were created that were compared against those of the isolated Y-duct. Finally, a *Python* program was used to calculate pressure distortion coefficients at the AIP as described in Section 3.3. Both of these codes are available in Appendix C.

3.3 Flow Quality Metrics

Flow quality metrics provide a quantitative representation of pressure recovery and loss, pressure distortion, and swirl at the AIP of a duct. The following subsections describe the metrics used to quantify Y-duct performance.

3.3.1 Static Pressure Coefficient

The coefficient of static pressure, $C_{p,x}$, represents the non-dimensionalized local static pressure of the flow. This coefficient is used in identifying a region of flow separation along any major meridian of the isolated Y-duct and calculated using Equation 3.1.

$$C_{p,x} = \frac{p_{s,x} - p_{s,1}}{p_{0,1} - p_{s,1}} \tag{3.1}$$

where $p_{s,x}$ is the static pressure at a given point in the duct, $p_{s,1}$ is the static pressure at the duct entrance, and $p_{0,1}$ is the laboratory atmospheric pressure.

3.3.2 Total Pressure Loss and Recovery

The area-averaged total pressure recovery, $\overline{\pi}$, denotes the degree of area-averaged total pressure recovery at the AIP compared to the total pressure available at the inlet entrance. Ideally this value would be unity, meaning all available total pressure was recovered and the duct exhibits no loss. Equation 3.2 is used for the calculation of $\overline{\pi}$ effected at the AIP of both the isolated and internal aerodynamics Y-duct.

$$\overline{\pi} = \frac{\overline{p_{0,2}}}{p_{0,1}} \tag{3.2}$$

where $p_{0,1}$ is the total pressure at the duct entrance (atmospheric pressure) and $\overline{p_{0,2}}$ is the area-averaged total pressure at the AIP. Area-averaged total pressure loss, $\overline{\gamma}$, is defined in Equation 3.3.

$$\overline{\gamma} = 1 - \frac{\overline{p_{0,2}}}{p_{0,1}} = 1 - \overline{\pi} \tag{3.3}$$

3.3.3 Total Pressure Distortion

Total pressure distortion is an important parameter in quantifying inlet duct performance. High pressure distortion at the AIP of a duct can lead to un-even loading on compressor blades and even unsteady combustion of a gas turbine engine, both leading to degraded performance of an air vehicle. The pressure distortion in the worst j degree sector at the AIP, $DC(j)$, was calculated for both the isolated and embedded Y-ducts using Equation 3.4.

$$DC(j) = \left(\frac{\overline{p_{0,2}} - \overline{p_{0,j}}}{\overline{p_{0,2}} - \overline{p_{s,2}}} \right)_{\max} \tag{3.4}$$

where $\overline{p_{0,j}}$ denotes the total pressure in the worst j sector at the AIP. Traditionally the sector, j, is taken as 60° so the coefficient becomes $DC(60)$.

The maximum radial distortion descriptor, $DPRP_{\max}$, denotes the worst area-averaged circumferential distortion in one of the circumferential rings (the *ith*) at the AIP. For calculations, the AIP is divided into five equal area concentric rings for the isolated Y-duct, and four for the internal aerodynamics model. Both AIPs are also divided into sectors with the isolated duct featuring twelve 30° sectors and the embedded Y-duct having twenty four 15° sectors, identified by k. This indexing is shown in Fig. 3.12 for the isolated Y-duct. The $DPRP_{\max}$ was calculated using Equation 3.5.

$$DPRP_{\max} = \left(\frac{\overline{p}_{0,2} - \overline{p}_{0,2,i}}{\overline{p}_{0,2}} \right)_{\max} \tag{3.5}$$

where $\overline{p}_{0,2,i}$ is the area-averaged total pressure in the worst circumferential ring, i.

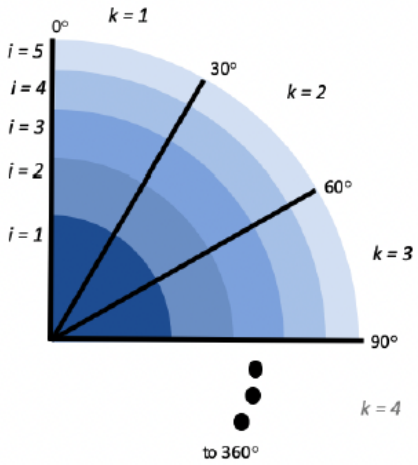

Figure 3.12: Radial and Circumferential Indices at the Isolated Y-Duct AIP [4].

Similarly, the average circumferential distortion descriptor, $DPCP_{\text{avg}}$, quantifies circumferential total pressure distortion in each sector, k, where the local area-averaged pressure recovery is below that of the ring average. The circumferential distortion descriptor for the isolated Y-duct was calculated using Equation 3.6:

$$DPCP_{\text{avg}} = \frac{1}{5}\sum_{i=1}^{5}\left(1 - \frac{\sum_{k=1}^{12}\begin{cases}\frac{\overline{p}_{0,2,i,k}}{\overline{p}_{0,2,i,}} & \overline{p}_{0,2,i,k} < \overline{p}_{0,2,i,} \\ 0 & \overline{p}_{0,2,i,k} \geq \overline{p}_{0,2,i,}\end{cases}}{\sum_{k=1}^{12}\begin{cases}1 & \overline{p}_{0,2,i,k} < \overline{p}_{0,2,i,} \\ 0 & \overline{p}_{0,2,i,k} \geq \overline{p}_{0,2,i,}\end{cases}}\right) \tag{3.6}$$

3.3.4 Swirl

Due to the limited instrumentation in the restrictive internal volume of the internal aerodynamics model, swirl metrics could only be calculated for the isolated Y-duct with data from the 5-hole *Aeroprobe*. The angle of local swirl, α was calculated using Equation 3.7.

$$\alpha = \arctan\left(\frac{v_\theta}{u}\right) \tag{3.7}$$

where u is the local axial velocity and v_θ, as sketched in Fig. 3.13, is the local circumferential velocity.

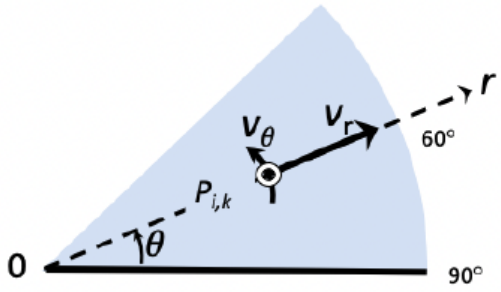

Figure 3.13: Velocity Vectors at the AIP Looking Downstream Parallel with u [4].

Swirl intensity is the average of the absolute, circumferential swirl angle in degrees for each ring at the AIP. This parameter was first developed by Bouldin and Sheoran [39] before later becoming SAE standard [23]. This descriptor can be considered as the extent-weighted absolute swirl at the AIP and is calculated using Equation 3.8.

$$SI(i) = \frac{\sum_{k=1}^{m} SS_{i,k}^{+}\theta_{i,k}^{+} + \sum_{k=1}^{m} |SS_{i,k}^{-}\theta_{i,k}^{-}|}{360} \tag{3.8}$$

where SS^{+} and SS^{-} correspond to the average positive (counter-clockwise facing upstream) and negative (clockwise facing upstream) swirl angles respectively, for a given sector region *i,k*. The angular extent of swirl for the same region is θ, indexed for i and k. velocities calculated from the *Aeroprobe* were averaged across all rings, so Equation 3.8 could be simplified as Equation 3.9.

$$SI = \overline{|\alpha|} \tag{3.9}$$

Swirl directivity, *SD* was calculated using Equation 3.10.

$$SD(i) = \frac{\sum_{k=1}^{m} SS_{i,k}^{+}\theta_{i,k}^{+} + \sum_{k=1}^{m} SS_{i,k}^{-}\theta_{i,k}^{-}}{\sum_{k=1}^{m} SS_{i,k}^{+}\theta_{i,k}^{+} + \sum_{k=1}^{m} |SS_{i,k}^{-}|\theta_{i,k}^{-}} \tag{3.10}$$

This parameter represents the overall sense of swirl rotational direction at the AIP. Values of *SD* can range from -1 to +1. A *SD* of 0 at the AIP denotes a pure twin swirl or no swirl while a value of -1 or +1 denotes the presence a pure bulk swirl. Since data from the *Aeroprobe* were averaged across each of the rings, Equation 3.10 could also be simplified, resulting in Equation 3.11.

$$SD = \frac{\overline{\alpha}}{|\overline{\alpha}|} \tag{3.11}$$

The swirl pair parameter, *SP*, indicates the number of CRV present at the AIP and can be calculated using Equation 3.12.

$$SP(i) = \frac{\sum_{k=1}^{m} SS_{i,k}^{+}\theta_{i,k}^{+} + \sum_{k=1}^{m} |SS_{i,k}^{-}|\theta_{i,k}^{-}}{2 \times max\left[\sum_{k=1}^{m} SS_{i,k}^{+}\theta_{i,k}^{+}, \sum_{k=1}^{m} |SS_{i,k}^{-}|\theta_{i,k}^{-}\right]_{k=1\ldots m}} \tag{3.12}$$

An *SP* value of 1 represents a single pair of CRV while a value of 0.5 denotes that a purely bulk swirl is present (half a vortex pair). As before, since data from the *Aeroprobe* were averaged, Equation 3.12 could be simplified to Equation 3.13.

$$SP = \frac{|\overline{\alpha}|}{2 \times max\left[\overline{\alpha}^{-}, \overline{\alpha}^{+}\right]} \tag{3.13}$$

4 Results and Discussion

This chapter presents and discusses the results for both the isolated Y-duct and the embedded Y-duct in the internal aerodynamics model. Results for static and total pressure recovery, total pressure distortion, and swirl are presented for the isolated Y-duct. Total pressure recoveries and distortion are presented for the internal aerodynamics model Y-duct and compared with the isolated duct for the zero angle-of-attack, zero yaw case. The influences of yaw angle and angle-of-attack on the performance of the embedded Y-duct are also discussed here.

4.1 Isolated Y-duct

The following sections detail the observed performance of the isolated Y-duct for two intake entrance Mach numbers.

4.1.1 Static Pressure Recovery

Static pressure distribution helps to observe flow behaviour in the duct, aiding to identify zones of separated flow. The results from the static pressure recovery of the isolated Y-duct also aid in the understanding of flow features within the duct and of the more complex flow behaviour present within the embedded Y-duct of the internal aerodynamics model. Any zones of separated flow are resultants of adverse pressure gradients caused by area diffusion as well as flow turning as discussed in Chapter 2. Static pressure measurements were made along each major axis of the Y-duct, the orientations of which are labelled in Fig. 4.1.

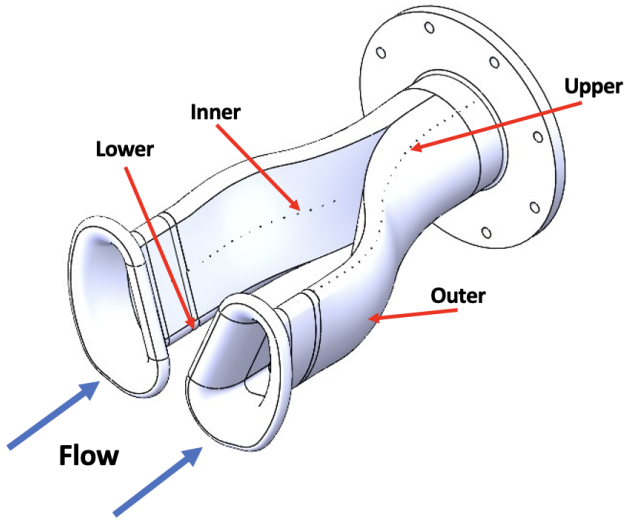

Figure 4.1: Static Pressure Measurement Orientations for the Isolated Y-duct.

The upper, lower, inner, and outer meridians provide good insight regarding flow behaviour along each of the main surfaces encompassing both the vertical and horizontal offset of the duct. The flow in the two limbs was not averaged, rather opportunities were taken when space was available for the four meridians tested. The coefficient of static pressure results for the isolated Y-duct at an entrance speed of Ma=0.80 is presented in Fig. 4.2. The uncertainty for an average C_p was 3×10^{-5}. Uncertainty calculations are detailed in Appendix A.

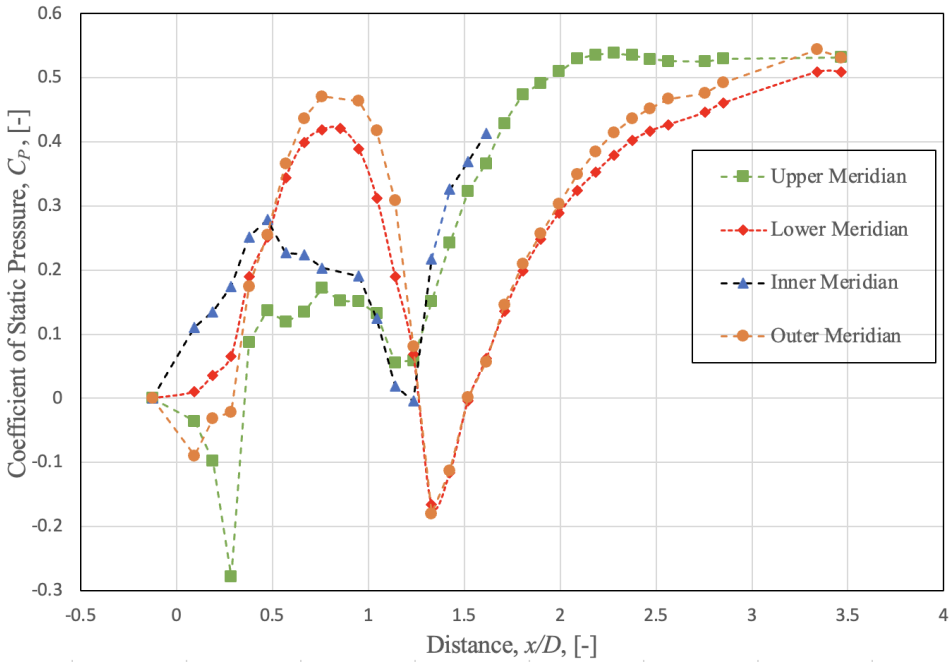

Figure 4.2: Static Pressure Coefficient for the Isolated Y-duct at Ma=0.80.

Considering the upper meridian, a suction peak is noted at $\frac{x}{D} \approx 0.35$ caused by the acceleration of the flow along the inner radius of the first vertical offset. This suction peak is followed by a period of flow separation spanning from $\frac{x}{D} \approx 0.4$ until $\frac{x}{D} \approx 1.4$ characterized by the region of relatively stagnant C_p followed by a brief zone of static pressure reduction and then a recovery from the deceleration of re-attached flow in the Y-duct. The lower meridian follows an initial trend of static pressure recovery as the flow decelerated along the outer radius of the first vertical offset before accelerating again along the inner radius of the second vertical offset reaching a suction peak at $\frac{x}{D} = 1.3$. The static pressure of the flow begins to recover past this point and continues to as the two ducts merge. No flow separation is noted along this meridian.

Initially, the inner meridian experiences a small pressure recovery due to the area diffusion of the duct before reaching a suction peak at $\frac{x}{D}$=1.25 corresponding to the flow accelerating along the inner radius of the first horizontal bend. Due to the merging of the two Y-duct limbs, the inner meridian includes fewer data points than the others. The static pressure along the outer meridian initially drops before separating briefly from $\frac{x}{D} \approx 0.2$ until $\frac{x}{D} \approx 0.25$, a result of the adverse pressure gradient along the outer radius of the first horizontal

offset of the duct. Following this period of deceleration along the outer radius, the flow accelerates along the inner radius of the second horizontal bend before reaching a suction peak at $\frac{x}{D} \approx 1.3$. At this point, the merging of the two duct limbs causes the flow to decelerate further and recover static pressure.

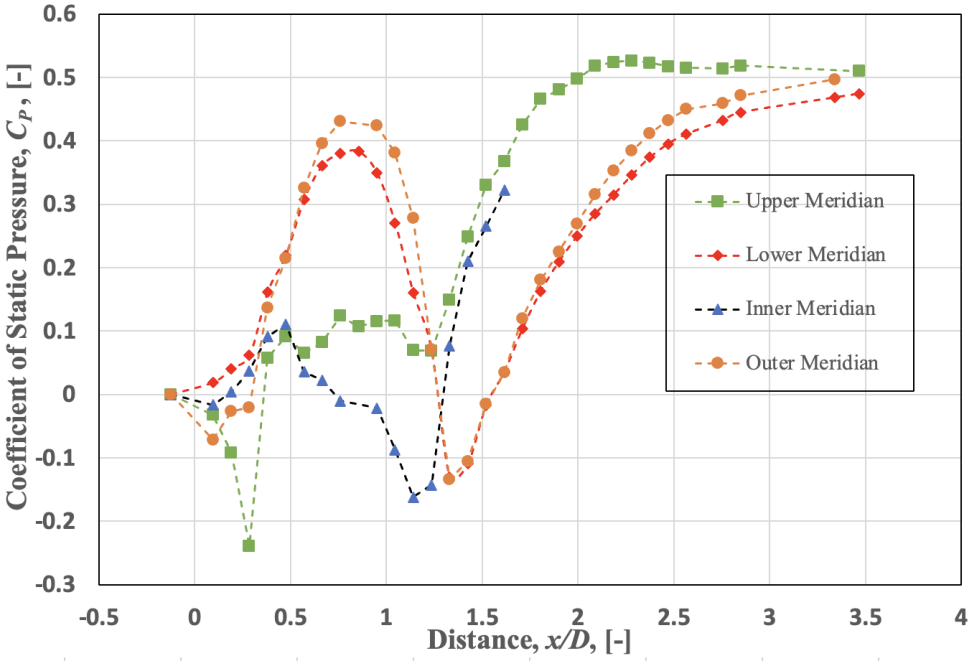

Figure 4.3: Static Pressure Coefficient for the Isolated Y-duct at Ma=0.63.

Static pressure results for Ma=0.63 are given in Fig. 4.3. Here the static pressure trends are quite similar to those of Ma=0.80. All major flow features discussed for Ma=0.80 were present at 0.63. Minor differences were observed at Ma=0.63 such as a slightly earlier suction peak on the inner meridian at $\frac{x}{D} \approx 1.15$ and a longer separated zone after the inner radius on the first vertical offset on the upper meridian at $0.5 \leq \frac{x}{D} \leq 1.2$. The static pressure along the inner surface displayed consistently lower values of C_p at Ma=0.63 compared to Ma=0.80 caused by the increase magnitudes of adverse pressure gradients within the duct. The overall static pressure recovery for Ma=0.80 was higher than that of Ma=0.63.

4.1.2 Total Pressure Recovery

Total pressure recovery at the AIP was mapped for the isolated Y-duct using the 5-hole *Aeroprobe* data acquisition system. These plots provide a visual representation of the total pressure distortion and recovery. Circumferential positions around the AIP are marked using degrees between 0 and 360 ascending clockwise while looking upstream as shown in Fig. 4.4.

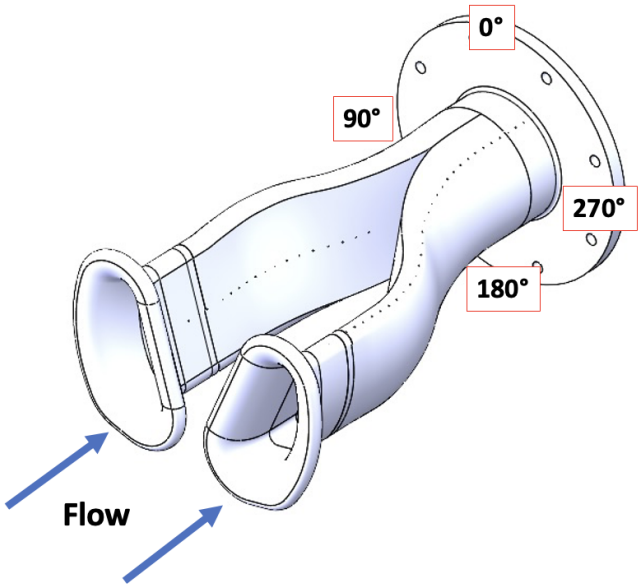

Figure 4.4: Y-Duct Total Pressure Plot Orientation.

Figure 4.5 shows the total pressure recovery at the AIP looking upstream for the isolated Y-duct at an inlet entrance speed of Ma=0.80.

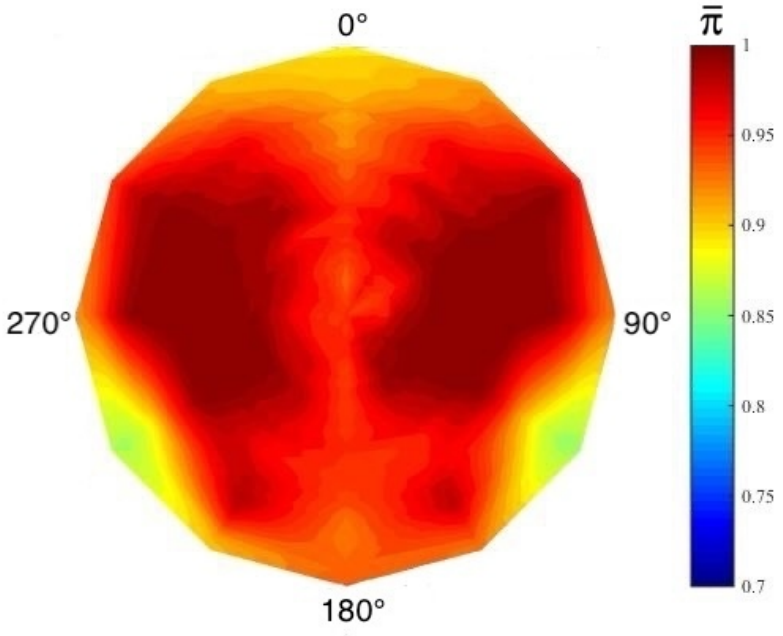

Figure 4.5: Total Pressure Recovery at the Isolated Y-Duct AIP at Ma=0.80

The total pressure recovery at the AIP for the isolated Y-duct featured two regions of high total pressure recovery located in the centre region concentrated around the 90° and 270° meridians. These zones of high pressure recovery correlate to the most undisturbed regions of incoming flow from the centre of each Y-duct limb. The lowest regions of total pressure recovery are concentrated at the outer circumferential positions at the 120° and 240° angles. These zones of low recovery were caused by the the separated flow in the Y-duct along the outer meridian just upstream of the AIP. This region was not noted in Fig. 4.2 as the separation occurred locally between measurement meridians.

A second region of low total pressure recovery is visible concentrated in the upper portion of the AIP around the 0° meridian. This was caused by the separation along the upper meridian. The merging plane of the two entrance limbs is also clear as a vertical line of decreased total pressure recovery stretching diametrically between 0° and 180°. This reduced total pressure recovery may have been caused by frictional losses on the splitter plate before merging of the two limbs. The total pressure recovery at Ma=0.63 is presented in Fig. 4.9 for comparison with the embedded Y-duct.

4.1.3 Swirl Performance

Although swirl data and plots could not be created for the internal aerodynamics embedded Y-duct model, the swirl performance for the isolated duct was measured and is reported in this section for understanding the development of secondary flows within Y-ducts. The same meridian labelling and orientation as that presented in Fig. 4.4 was used for the swirl plots. The swirl distribution across the AIP for the isolated Y-duct at Ma=0.80 is shown in Fig. 4.6.

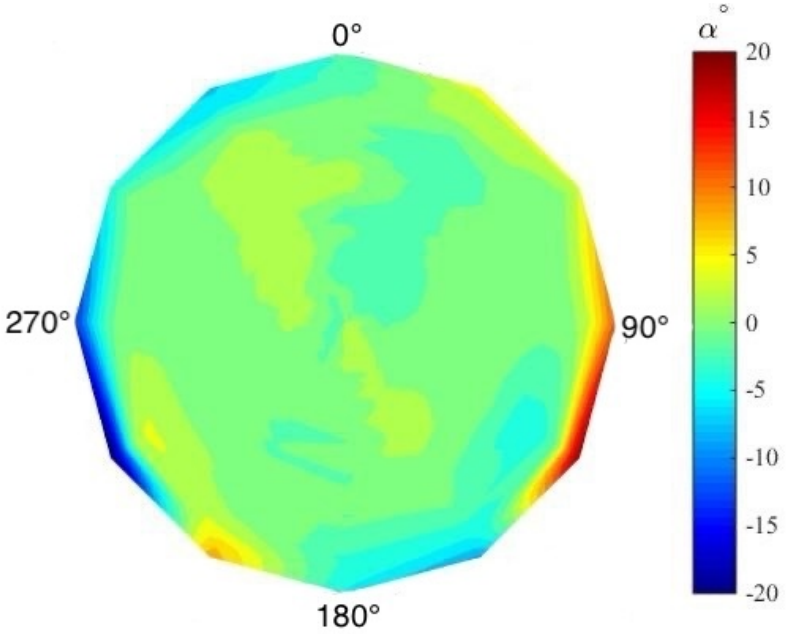

Figure 4.6: Swirl Angle Distribution at the Isolated Y-Duct AIP at Ma=0.80.

Here, small areas of high magnitude local swirl exist at the outer radii approximately between the 90° to 120° and 240° to 270° meridians. These roughly correspond to areas of lower total pressure recovery identified in Fig. 4.5. Two pairs of counter-rotating vortices (CRV) are present with one towards the centre upper portion of the duct and the other located closer to the 180° meridian. The swirl results also support the total pressure recovery results in Fig. 4.5. Regions of zero local swirl in the central regions of the AIP correspond to the areas of high total pressure recovery due to the reduced losses in these areas. Swirl performance at Ma=0.63 is shown in Fig. 4.7.

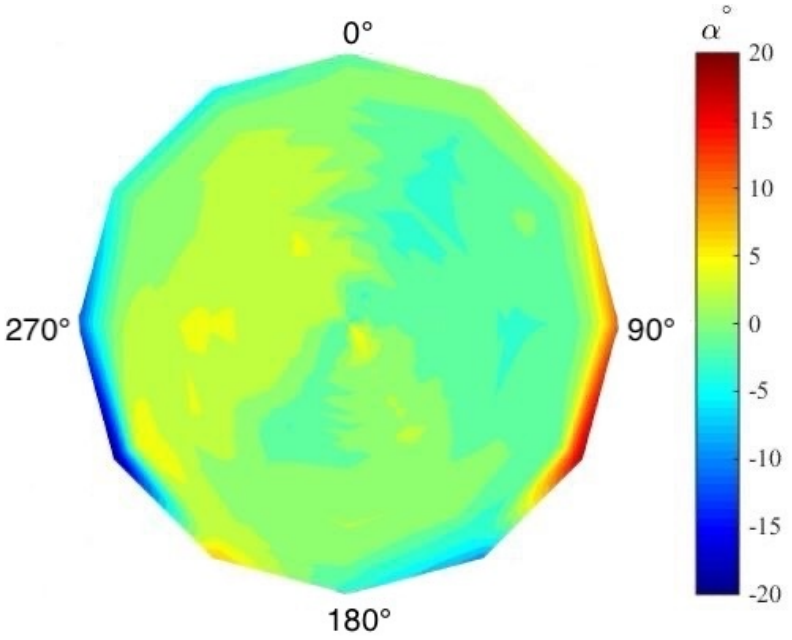

Figure 4.7: Swirl Angle Distribution at the Isolated Y-Duct AIP at Ma=0.63

Figure. 4.7 shows that the swirl performance at Ma=0.63 was very similar to Ma=0.80. All major features observed in Fig. 4.6 are present at the lower entrance Mach number. It should be noted that the size of regions with high local swirl decreased for Ma=0.63, corresponding to the reduced size of low total pressure recovery regions at 120° and 240° angles as shown in Fig. 4.9a. Conversely, the regions of zero swirl angle have increased corresponding to the increased areas of high total pressure recovery in Fig. 4.9a compared to Ma=0.80 results shown in Fig. 4.5. Swirl coefficients for the isolated Y-duct are given in Tab. 4.1.

Table 4.1: Isolated Y-duct Swirl Coefficients at the AIP.

Coefficient	Ma=0.80	Ma=0.63
SI [°]	2.401 ± 0.012	2.389 ± 0.012
SD [-]	0.204 ± 0.007	0.324 ± 0.007
SP [-]	1.833 ± 0.003	2.052 ± 0.003

The swirl coefficients for the two entrance Mach numbers remained relatively close. The lower entrance Mach number had a slightly higher magnitude

of swirl directivity, denoting a greater magnitude of bulk swirl present at this entrance speed. The number of swirl pairs increased at Ma=0.63. Gilbart *et al.* [4] highlighted both of these trends when decreasing the entrance Mach number for an S-duct intake.

4.2 Embedded Y-duct

This section discusses and compares results obtained from the internal aerodynamics model with embedded Y-duct for a range of model angles-of-attack and yaw. Total pressure recovery, distortion parameters, and inlet Mach numbers are investigated. A comparison between the baseline Y-duct and embedded Y-duct at zero flight angles is also presented. For the purposes of comparison between different model orientations, a numerical abbreviation will be used for brevity and clarity: A(AoA)Y(β) where AoA and β identify angle-of-attack and yaw angles in degrees. For example, for the case where the model is oriented at an 8° angle-of-attack with 4° yaw, the abbreviation used would be $A8Y4$. For the case with -4° angle-of-attack and 0° yaw, the shorthand would be A-4Y0.

4.2.1 Comparison with Isolated Y-duct

The first orientation of the internal aerodynamics model is the A0Y0 case where the model is aligned with oncoming flow. This directly compares with the isolated Y-duct to evaluate the effects of the model forebody on Y-duct performance. The orientation of the model with respect to the freestream from both a lateral, and streamwise (head-on) perspective, are given in Fig. 4.8.

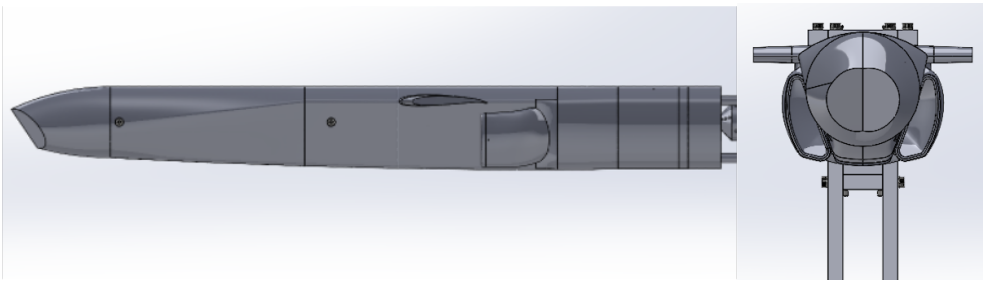

(a) Lateral View. (b) Streamwise View.

Figure 4.8: Model Orientation of A0Y0 Test.

As shown in Fig. 4.8a, about two thirds of the model's fuselage lies directly upstream of the Y-duct intake. Figure 4.8b shows the model looking downstream. The transition from a circular nose to trapezoidal lifting body fuselage can also be noted in this view with the transition partially blocking a direct path for the freestream into the intake.

The internal aerodynamics model was tested with an average freestream Mach number over the model of Ma=0.80. At this freestream test Mach number, it was found that the Y-duct inlet entrance reached just Ma=0.52. This lower Mach number was a result of both the model's forebody as well as the blockages and losses caused by the Y-duct in the freestream flow. The observed decrease in Mach number at the intake entrance aligns with work presented in Raymer [33]. In this work, Raymer details that the intake of an aircraft travelling in a freestream of Ma=0.8 might only experience Ma=0.6 at the intake entrance. The intake Mach could be increased if a suction was present in the inlet such as that provided by a gas turbine engine.

For the internal aerodynamics model, the flow is further slowed prior to the inlet entrance due to the effect of boundary layer development on the forebody, exacerbated by the aforementioned nose blockage from the round-to-trapezoidal transition of the forebody. The influence of the higher pressure under the wings directly upstream of the inlet entrance also acts to create a small adverse pressure gradient, further slowing the flow. The effects of the forebody could be isolated from the Y-duct itself by testing the duct in a freestream without an induced suction. Though the model was tested at a freestream speed of Ma=0.8, it was decided isolated Y-duct results for an intake entrance speed of Ma=0.63 would provide a more direct comparison due to the decreased intake entrance Mach number of the model compared with the freestream. Key Mach number data for the embedded and isolated ducts are compared in Table 4.2.

Table 4.2: Isolated and embedded Y-duct Mach number at A0Y0.

Location	Embedded Y-duct	Isolated Duct
Model Body	0.803	0
Inlet Entrance	0.525	0.63
AIP	0.418	0.45

Due to the limitations in data for comparison, the inlet entrance speeds between the isolated and embedded Y-duct will not match exactly. The lower isolated Y-duct intake speed of Ma=0.63 will provide a relatively close comparison of results and allow for the effects of the forebody to be highlighted.

Total Pressure recovery

Plots of total pressure recovery at the AIP for both isolated and embedded Y-ducts were created. Because of the differences in the intake entrance Mach numbers between the two Y-ducts as well as the influence of the forebody, close matching in results is not necessarily expected. The total pressure recovery at the AIP of the isolated and embedded Y-ducts is shown in Fig. 4.9, where plots are oriented looking upstream.

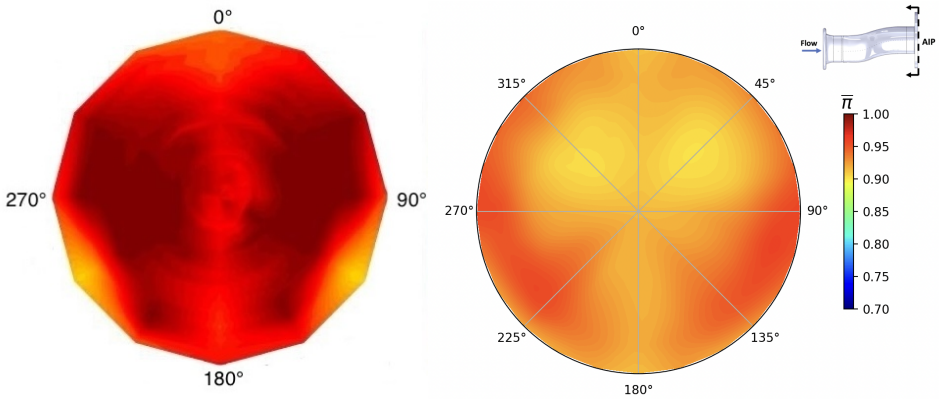

(a) Isolated Entrance Ma=0.63 (b) Embedded Entrance Ma=0.52

Figure 4.9: Total Pressure Recovery at the AIP for the Isolated and Embedded Y-Duct

The isolated Y-duct at Ma=0.63 in Fig. 4.9a had areas of high total pressure recovery centrally around the 90° and 270° angles. Areas of high pressure recovery can also be noted on the embedded Y-duct although their locations have shifted downward concentrated around the 120° and 240 ° angles. These regions have moved radially towards the outside of the AIP with a decreased magnitude of local pressure recovery compared with the isolated duct. This migration was likely caused by the high pressure on the underside of the wing deflecting freestream flow towards the lower part of the intake entrance.

The downward shift of these high pressure recovery regions also eliminated the regions of lower pressure recovery for the isolated duct around the 120° and 240° angles. The decrease in magnitude of total pressure recovery for the embedded Y-duct was caused primarily by the influence of boundary layer developed along the fuselage upstream of the inlet entrance.

The shift in location of high pressure recovery was also likely driven by the combination of boundary layer and wing effects. The relatively small adverse pressure gradient created by the underside of the main wing may cause the low energy boundary layer to separate upstream of the inlet entrance. The disturbed flow creates the regions of low pressure recovery observable in the central area of the AIP towards the 0° meridian along the 45° and 315° angles. This explains why the same low pressure recovery area is absent in the isolated duct. Flow visualization over the model would help to confirm this hypothesis.

Both ducts also clearly show a centralized region of low pressure recovery running from the 0° to 180° meridian due to the merging of the limbs into a single duct ahead of the AIP. At this flight orientation, any vortices created by the faceted nose would be directed underneath the fuselage and have no effect on the performance of the Y-duct. The results of the isolated Y-duct at Ma=0.63 show that all the major features observed in the total pressure recovery for Ma=0.80 were also present for the lower entrance Mach number. The lower entrance Mach number clearly showed an improvement in total pressure recovery across the entire AIP, a trend not noted for the embedded Y-duct due to the presence of the forebody. Areas of high pressure recovery in the centre regions of the AIP of the isolated duct at Ma=0.63 increased in size and areas of lower total pressure recovery, such as those around the 0°, 120°, and 240° angles, have increased in magnitude of recovery compared to Ma=0.80. The isolated and embedded duct performance can be further analyzed with their pressure recovery and loss coefficients: Table. 4.3 compares pressure distortion and recovery parameters.

Table 4.3: Total Pressure Recovery and Distortion Coefficient Comparison.

Parameter	Embedded Duct	Isolated Duct Ma=0.80	Isolated Duct Ma=0.63
$\overline{\pi}$	0.927 ± 0.0023	0.96245 ± 0.00003	0.97495 0.00003
$\overline{\gamma}$	0.073 ± 0.0023	0.03575 ± 0.00003	0.02505 ± 0.00003
$DPRP_{\max}$	0.012 ± 0.0013	0.0447 ± 0.00028	0.0319 ± 0.00028
$DPCP_{\text{avg}}$	0.0115 ± 0.0005	0.0249 ± 0.0001	0.0187 ± 0.0001
$DC(60)$	0.31 ± 0.059	0.2195 ± 0.00019	0.1851 ± 0.00019

Easily inferred from the total pressure recovery plots in Fig. 4.9, the total pressure losses are greater for the embedded duct: 7.33 % compared to 2.5 % for the isolated duct at Ma=0.63. The increase in loss coefficient was mainly due to the strong influence of boundary layer along the forebody of the internal aerodynamics model. Radial and circumferential distortion descriptors for the isolated duct were higher than the embedded, again unsurprising when reviewing the contour plots presented in Fig. 4.9. The embedded Y-duct had much smaller differences in magnitudes of pressure recovery across the entire AIP compared with those of the isolated duct. The influence of forebody boundary layer on the embedded Y-duct attenuated the overall pressure recovery, avoiding great differences in local pressure recovery across the AIP. Interestingly, the $DC(60)$ for the embedded Y-duct was slightly greater than that of the Ma=0.80 isolated duct: 0.31 compared to 0.2195. This signifies the AIP of the embedded Y-duct sees greater differences between local total pressure and the AIP average compared with the isolated. The locations of the two also varied with the $DC(60)$ being centred around the 0° meridian for the isolated duct and between 0° and 60° for the embedded Y-duct. The increase in $DC(60)$ for the embedded Y-duct, despite the decrease in radial and circumferential distortion descriptors, was potentially caused by the low pressure recovery evident in the upper regions towards the 0° meridian. The pressure recovery in these regions was lower than the average for the AIP. A lower local total pressure recovery combined with higher static pressure (see Equation 3.4) at the AIP due to the lower Mach number would cause a higher overall $DC(60)$ compared with the isolated duct at Ma=0.80.

4.2.2 Effect of angle-of-attack

The internal aerodynamics model was designed for investigating the effects of angle-of-attack on the forebody flow and interaction with the embedded Y-duct. The model pivoted between -4° angle-of-attack (nose down) and 8°

angle-of-attack (nose up) about its cantilevered support. The inlet performance was evaluated with no yaw at model angles-of-attack of -4° (A-4Y0), 0° (A0Y0), 4° (A4Y0), and 8° (A8Y0).

Best efforts were made to maintain the vehicle freestream Mach number consistent at Ma=0.8 at all flight orientations. Unfortunately due to the complex external shape of the model and the small fixed size of the wind tunnel, exact Mach number matching was not possible. Average Mach numbers for the vehicle freestream, intake, and AIP are summarized in Tab. 4.4. Each Mach number is an average over six test runs.

Table 4.4: Average Model Mach Numbers at Zero Yaw Angle.

Orientation	Freestream	Intake Entrance	AIP
A-4Y0	0.811 ± 0.0044	0.532 ± 0.006	0.421 ± 0.0075
A0Y0	0.804 ± 0.0044	0.526 ± 0.006	0.418 ± 0.0074
A4Y0	0.807 ± 0.0044	0.503 ± 0.0062	0.373 ± 0.0084
A8Y0	0.819 ± 0.0044	0.480 ± 0.0064	0.346 ± 0.0091

As mentioned above, all vehicle freestream Mach numbers varied by less than 0.02 from Ma=0.8 with A8Y0 having the greatest average vehicle Mach number at Ma=0.819. There is not necessarily a direct link between the average vehicle freestream Mach number and inlet entrance Mach number. Due to the complex shaping of the model, horizontal asymmetry and the vehicle Mach numbers measured above the vehicle, different angles of attack position the inlet entrance in such ways where there is no discernible trend between the two. However, a trend did emerge between the inlet entrance and AIP Mach numbers, as shown in Fig. 4.10. In this figure, and all successive scatter plots, the marker sizes correspond to their uncertainty.

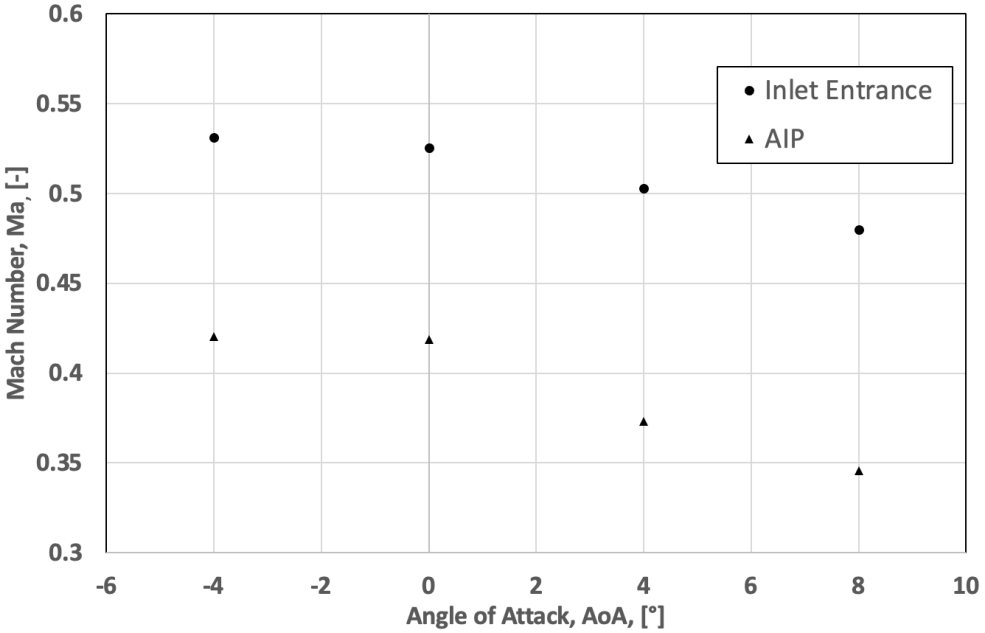

Figure 4.10: Effect of Angle-of-Attack on Inlet Entrance and AIP Mach Numbers.

Here a clear trend of decreasing Mach number with increasing angle-of-attack was apparent for both the inlet entrance and AIP. This trend for the AIP is expected in particular since this Mach number is directly dictated by the intake entrance Mach number. The Y-duct intake is designed to slow down the oncoming flow to conditions acceptable for engine consumption using flow diffusion within the duct. The decrease in inlet entrance Mach number with increasing angle-of-attack is hypothesized to be caused due to increased blockage both from the orientation of the intake and the forebody as well as the required flow turning angle. The effect of angle-of-attack can be further examined using the freestream view of the model across varying angles-of-attack as shown in Fig. 4.11.

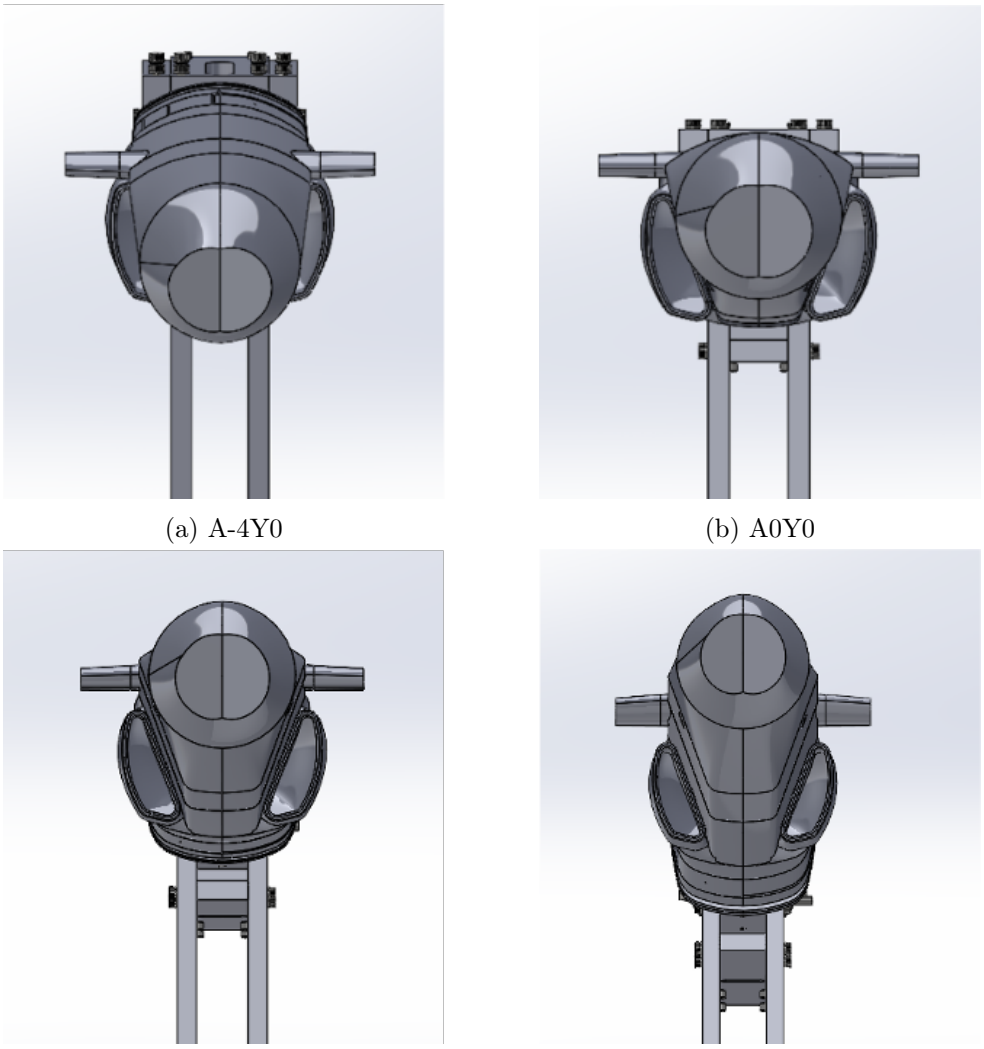

(a) A-4Y0 (b) A0Y0

(c) A4Y0 (d) A8Y0

Figure 4.11: Freestream Perspectives of the Internal Aerodynamics Model at Varying Angle-of-Attack with Zero Yaw Angle.

Here, the increased angle-of-attack visible in Fig. 4.11c and Fig. 4.11d highlight the wing position at these angles. The increased angle-of-attack of these orientations increased the blockage for oncoming flow entering the intake, increasing the pre-compression of the flow through ram effect. Similarly the larger surface area of the underside of the wing in the path of the free stream flow works to create an area of high static pressure just upstream of the intake

entrance. This adverse pressure gradient slows the flow approaching the inlet entrance. As angle-of-attack is increased, the axial velocity through the duct must decrease. These phenomena are sketched in Fig. 4.12.

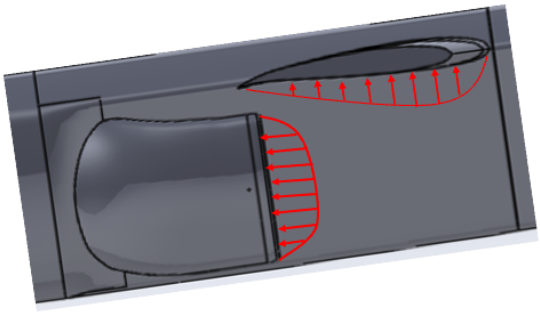

(a) Pre-Compression.

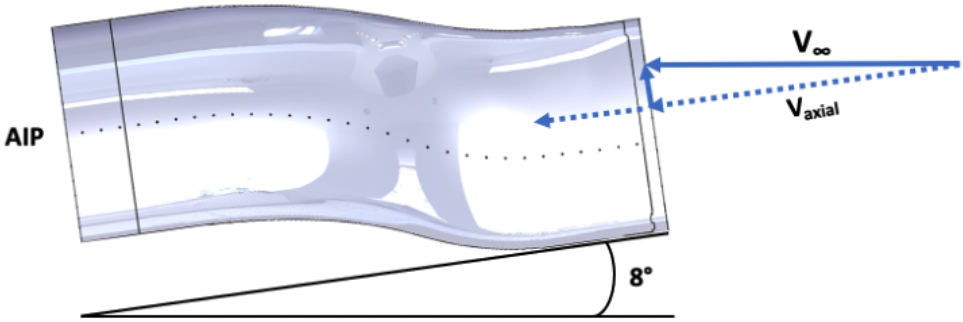

(b) Flow Turning.

Figure 4.12: External Effects on Embedded Y-Duct.

For negative angle-of-attack, the inlet Mach number increased less than could be hypothesized from the trend for positive angles-of-attack. The change in trend was driven primarily from the horizontal asymmetry of the model. The trapezoidal shaping of the fuselage cross section is clear in Fig. 4.11b effectively blocking some of the freestream from entering directly into the intake. This will be further discussed in this section. The Mach number at A-4Y0 is very close to that observed for A0Y0. This is hypothesized to be caused primarily by the lack of external compression occurring upstream of the intake in this flight configuration. This could be verified through testing an isolated Y-duct in the free stream velocity at varying angle-of-attack. Although the entrance Mach number was similar at this angle-of-attack, the pressure recovery and distortion varied quite significantly, which will be discussed in later sections

of this chapter. Total pressure recovery at the AIP is presented in Fig. 4.13 providing more insight on intake performance with varying angle-of-attack.

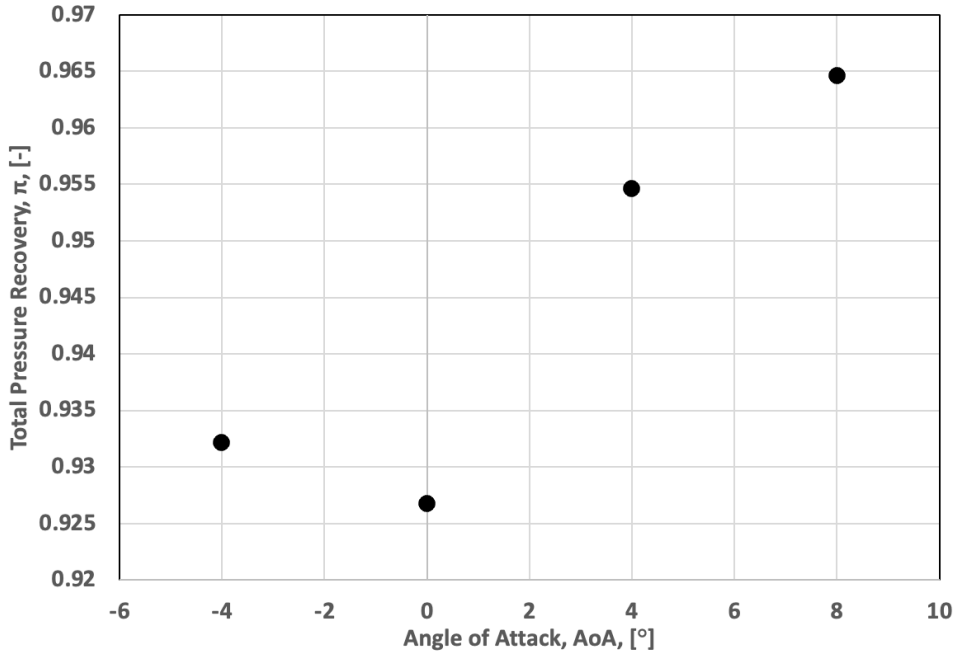

Figure 4.13: Angle-of-Attack Influence on Total Pressure Recovery at The AIP at 0° Yaw.

For increasing positive angles-of-attack, the results follow the expected trend of increasing total pressure recovery. This trend is opposite to that of inlet entrance Mach number and matches the results presented in Section 4.1.2, that is, the lower intake Mach number delivering higher pressure recovery in the isolated Y-duct.

Unlike the case of the isolated Y-duct, this increase in total pressure recovery with angle-of-attack for the embedded duct was primarily caused by two factors: first, the decrease in flow diffusion. The decreased flow diffusion allows the flow to stay attached to the inner radii of the vertical and horizontal duct bends, effectively eliminating some flow separation and total pressure loss. The second is from the external compression work done to the flow outside the intake through ram effect and influence of the main wing.

At A-4Y0, the total pressure recovery at the AIP increased compared to that observed for A0Y0, despite the higher intake Mach number at this flight condition. It is hypothesized the increase was caused by the reduction in boundary layer thickness being ingested by the intake at A-4Y0 compared to A0Y0. Due to the model's downward angle-of-attack at A-4Y0, the flow did not travel axially along the forebody of the model as it does for A0Y0, effectively decreasing the upstream wetted surface area and the size of boundary layer developed. Instead, the shorter travel reduces losses in the flow energy at the AIP. The negative angle also slowed the flow at the intake entrance due to the flow turning required, negating some of the effect of the horizontal offsets in the duct. This effect can be noted clearly in the total pressure recovery plot at the AIP in Fig. 4.14a and is discussed later in this work. Next, this section will detail and discuss the AIP total pressure recovery contour plots for each investigated angle-of-attack. Distortion coefficients for the internal aerodynamics model will be discussed at the end.

Total Pressure Recovery With Angle-of-Attack

This section details the effect of angle-of-attack on the total pressure recovery of the embedded Y-duct. Total pressure recovery contour plots are presented in Fig. 4.14. It should be noted that Fig. 4.14b is the same as the previously presented in Fig. 4.9b and is presented here again for ease of comparison. For comparison purposes the A0Y0 case will act as a baseline.

-4° Angle-of-Attack, 0° Yaw

The results for the A-4Y0 orientation shown in Fig. 4.14a differ quite significantly from the A0Y0 case previously discussed. In the bottom portion of the AIP between the 90° and 270° meridians, the A-4Y0 case displays a very concentrated region of high pressure recovery with greater magnitude than that of the A0Y0 case. Due to the negative angle of the model, the flow did not travel axially along the model as it did for the A0Y0 case but instead, cross flow components existed. The decrease in wetted area upstream of the intake entrance decreased the size of the boundary layer being ingested, increasing total pressure recovery. Due to the negative angle of the Y-duct with respect to the freestream in this orientation, oncoming air was able to travel more directly towards the bottom of the duct as shown in Fig. 4.14a with the required turning of the flow resulting increased pressure recovery towards the bottom of the entrance.

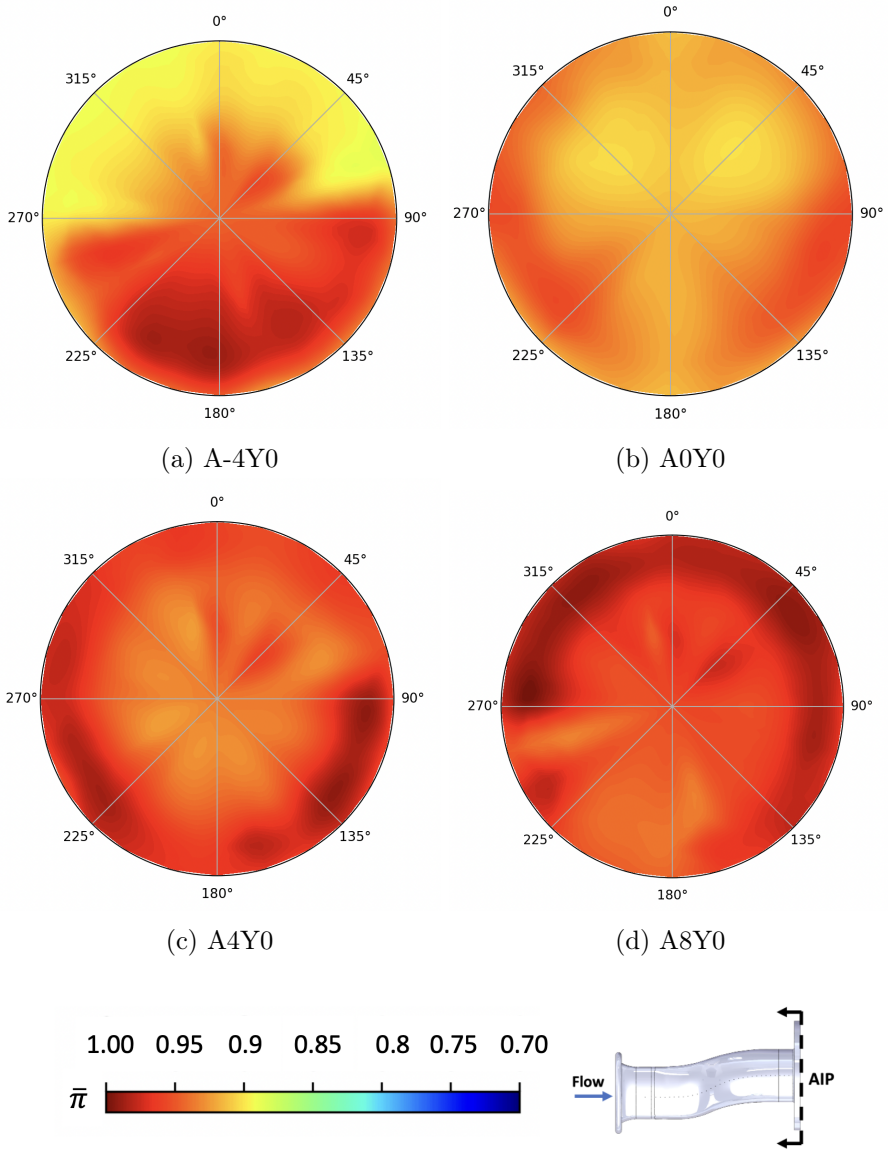

(a) A-4Y0 (b) A0Y0

(c) A4Y0 (d) A8Y0

Figure 4.14: Variation in Total Pressure Recovery with Angle-of-Attack.

At A-4Y0, the upper portion of the AIP towards the outer radii experienced lower total pressure recovery between approximately 90° and 270° meridians. Due to the negative angle-of-attack on the model's wing, what is usually the pressure surface of the wing instead became a suction surface, accelerating flow before it entered the upper portion of the intake, causing a loss in total pressure. A centralized region of higher pressure recovery is also apparent in the upper portion of the duct. This is caused by some of the more direct flow being shifted upwards due to the effect of the outer radius of the first vertical bend and the diffusion occurring at the inner radius of the second bend. At this negative angle-of-attack, any vortices generated from the nose are hypothesized to be directed under the fuselage and not affect the inlet performance.

4° Angle-of-Attack, 0° Yaw

The downstream orientation of the model at A4Y0 is shown in Fig. 4.11c. The increased angle-of-attack decreases the forebody wetted area upstream of the intake entrance relative to A0Y0. In Fig. 4.14c it can be noted that pressure recovery across the whole Y-duct AIP for A4Y0 was higher than that of A0Y0. The areas of higher total pressure recovery were apparent around the outer regions of the lower part of the AIP towards the 180° meridian. The regions of higher pressure recovery were concentrated around the outer radial locations between the 70° and 150° and 210° and 315° angles. The minor asymmetry of these regions is attributed to experimental artifacts during data acquisition. This concentration of high recovery fell approximately in the same circumferential locations as the areas of higher pressure recovery observed for the A0Y0 case however shifted radially outwards. The outer regions recovered the most direct flow and the angle-of-attack negated some of the flow separation caused by the first vertical bend in the duct through increased ram effect and required flow turning. The external compression of the freestream from the underside of the wing also contributed to the higher pressure recovery across the AIP compared to the A0Y0 case. The lowest regions of pressure recovery occurred towards the centre of the AIP. The reduction of pressure recovery in the central regions was caused by the effect of boundary layer from the upstream fuselage.

The combined effect of angle-of-attack and the second vertical bend on the upper surface of the Y-duct caused greater flow diffusion in this area contributing to the relatively lower pressure recovery evident around the 0° meridian. It is also hypothesized that at this angle-of-attack any vortices generated from the faceted nose of the model were directed towards the upper portions of the

intake entrance. The visible line of lower pressure recovery for the A0Y0 case, from the 0° meridian to the 180° meridian, was not noticeable in the A4Y0 case.

8° Angle-of-Attack, 0° Yaw

The A8Y0 orientation was the highest angle-of-attack investigated within the scope of this work. Evidently in Fig. 4.11d, the inlet is completely exposed to the oncoming flow with the pressure surface of the wing more exposed to the free stream than it was for A4Y0. The high angle-of-attack at this orientation also reduces the upstream wetted area ahead of the intake. Figure 4.14d shows the A8Y0 case with the highest total pressure recovery evaluated thus far continuing the trend of increasing total pressure recovery with positive angle-of-attack. The same flow mechanisms responsible for increased total pressure recovery with angle-of-attack are responsible again here. Areas of high pressure recovery have migrated upward towards the 0° meridian compared to the A4Y0 case, concentrated between the 135° and 225° angles. The lower pressure recovery noted at 240° angle was assumed to be a data acquisition error since it was expected that the recovery would be vertically symmetric at this orientation. The centre regions of A8Y0 experienced higher pressure recovery but were still relatively lower than that of the outer regions for the same orientation. Compared to A4Y0, the increased pressure recovery in these areas was caused by the reduction in the effect of boundary layer on pressure recovery. The low pressure region from 150° to 225° could be due to separated flow inside the lower lip of the inlet. Any Vortices developed on the nose of the model were assumed to be deflected over the top of the model not influencing the performance of the intake.

4.2.3 Distortion Descriptors

The distortion descriptors for all angle-of-attack cases with zero yaw are presented in Table 4.5.

Table 4.5: Embedded Y-duct Distortion Coefficients for Tests with no Yaw.

Orientation	$DPRP_{max}$	$DPCP_{avg}$	$DC(60)$
A-4Y0	0.02 ± 0.0024	0.0288 ± 0.0005	0.65 ± 0.061
A0Y0	0.012 ± 0.0014	0.0115 ± 0.0005	0.31 ± 0.059
A4Y0	0.019 ± 0.0011	0.0077 ± 0.00038	0.13 ± 0.053
A8Y0	0.009 ± 0.001	0.015 ± 0.00038	0.46 ± 0.053

Looking first at the $DPRP_{\max}$, no trend was apparent between the magnitude and angle-of-attack. For all of these cases the $DPRP_{\max}$ was located at the first radial measurement point from the centre of the AIP, except for A-4Y0 where it was located at the outermost. The identification of these locations are supported by polar plots presented previously and noting the regions of relatively high or low pressure recovery compared to the AIP average. $DPCP_{\text{avg}}$ also has no discernible trend with angle-of-attack: A4Y0 had the lowest value for $DPCP_{avg}$ while A-4Y0 had the highest. This could also be visually inferred where A-4Y0 exhibited great differences in circumferential pressure between the top (0° meridian) and bottom (180° meridian) regions of the AIP. By contrast, A4Y0 displayed much smoother circumferential pressure changes. $DC(60)$ values, as with the last two distortion coefficients, did not trend with angle-of-attack. The highest $DC(60)$ occurred at A-4Y0 between the 300° and 360° meridians. The lowest was found for A4Y0 occurring between the 330° and 30° angles.

4.2.4 Effect of Yaw

The effects of yaw on the performance of the internal aerodynamics model were also investigated. The model was able to pivot its support ±4° as described in Chapter 3. Due to the vertical symmetry of the model, only yaw in one direction was investigated. For all model orientations involving yaw, the nose of the missile yawed to the left when facing upstream. The combined effects of angle-of-attack and yaw were investigated with all the previously evaluated angles-of-attack repeated this time with 4° of yaw. Much like for zero yaw cases, the changes in model orientations with yaw resulted in slight Mach number variations across the internal aerodynamics model caused by changes to the effective cross sectional area of the test section. The variation

of freestream Mach numbers across yaw test orientations are listed in Table 4.6. Note that due to the lack of vertical symmetry when yawed, the entrance Mach numbers are reported separately for the left and right inlet. These Mach numbers are summarized in Table 4.7.

Table 4.6: Average Freestream Mach Numbers at 4° Yaw.

Orientation	Freestream
A-4Y4	0.797 ± 0.0044
A0Y4	0.808 ± 0.0044
A4Y4	0.808 ± 0.0044
A8Y4	0.819 ± 0.0044

Table 4.7: Average Vehicle Mach Numbers at 4° Yaw.

Orientation	Left Intake Entrance	Right Intake Entrance	AIP
A-4Y4	0.499 ± 0.0072	0.507 ± 0.0048	0.383 ± 0.0075
A0Y4	0.532 ± 0.0072	0.601 ± 0.0044	0.455 ± 0.0071
A4Y4	0.493 ± 0.0073	0.496 ± 0.0051	0.369 ± 0.0081
A8Y4	0.471 ± 0.0076	0.490 ± 0.0053	0.347 ± 0.0093

Table. 4.7 shows that the AIP Mach numbers were relatively consistent with those listed in Table 4.4 for the zero yaw cases, however, they do not match exactly. A comparison between the two is shown in Fig. 4.15.

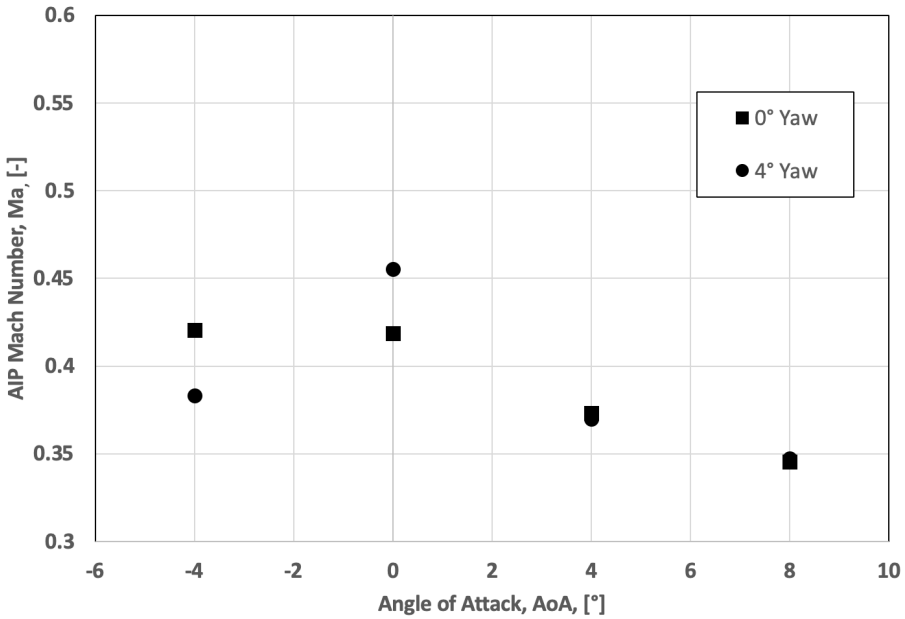

Figure 4.15: AIP Mach Number Variation with Angle-of-Attack and Yaw.

The AIP Mach numbers for A4Y4 and A8Y4 match fairly closely with their counterparts observed for A4Y0 and A8Y0. This matching begins to break down at lower angles-of-attack where the AIP Mach number for the A0Y4 case is higher than that of A0Y0 and at A-4Y4 where a lower AIP Mach number was observed compared to that for A-4Y0. These discrepancies stemmed directly from the influence of inlet entrance Mach number. Table. 4.7 shows that for A-4Y4 and A0Y4, greater differences were visible between the intake Mach numbers compared to the A-4Y0 and A0Y0 cases reported previously. The variation of intake Mach number with yaw and angle-of-attack is presented in Fig. 4.16.

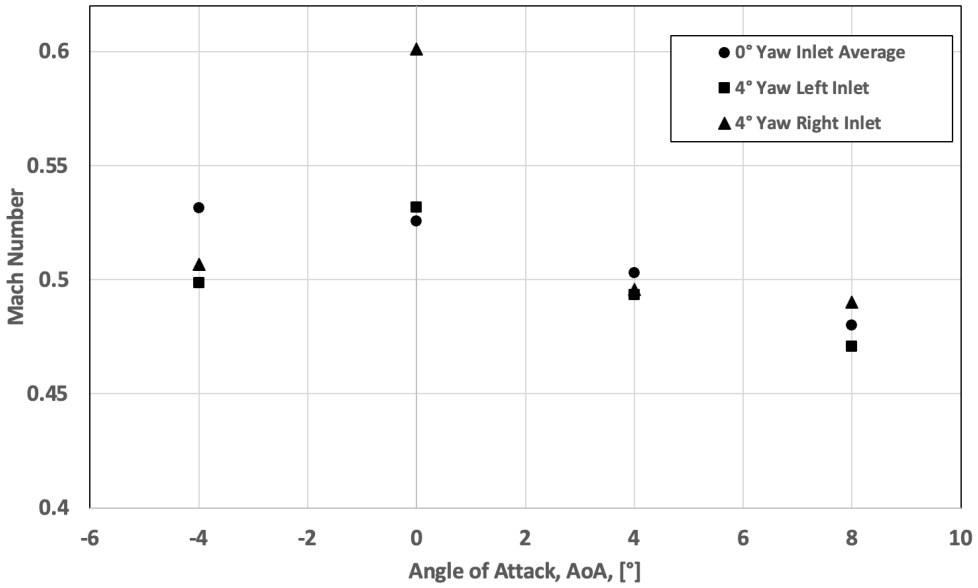

Figure 4.16: Variation of Intake Entrance Mach Numbers With Angle-of-Attack and Yaw.

The intake Mach number provides an interesting insight into the effect of yaw on the performance of the embedded Y-duct inlet. For the 0° yaw cases, the intake Mach number for both entrance limbs was consistent between left and right sides. The effect of yaw led to differences in Mach numbers between left and right inlets with some angles-of-attack influenced more than the others. As shown in Fig. 4.16 for the zero yaw cases, the variation of intake Mach number followed a linear pattern of decreasing Mach number with increasing angle-of-attack. This trend was not observed for the combined angle-of-attack and yaw orientations. The right inlet entrance (exposed by yaw) consistently experienced higher Mach numbers than the left side (off yaw axis) with the largest discrepancy between inlets noted for the A0Y4 case. At A0Y4, the right inlet faces the oncoming flow. Unlike for increased angles-of-attack, there was minimal adverse pressure gradient created from the underside of wing at this orientation resulting in a higher momentum flow. This was combined with the lack of boundary layer interference due to the fuselage being yawed away from the oncoming flow, leading to higher right hand inlet entrance Mach numbers for the A0Y4 orientation. The ram effect from the freestream on the fuselage acts to slow the oncoming flow somewhat, however, its effects are not as great as that of the underside of the wing. In the A0Y4 orientation, a wake is created

from the leeward side of the fuselage which travels towards the left intake. The exposure to this wake leads to lower pressure at the left intake, resulting in a higher inlet entrance Mach number than was noted for the A0Y0 case. It should also be considered that the non-parallel orientation of the model with respect to the freestream will influence the exit conditions of the duct which may affect the inlet entrance conditions. The forebodies influence on the intake Mach numbers can be explained when examining the downstream view of the internal aerodynamics model, seen in Fig. 4.17.

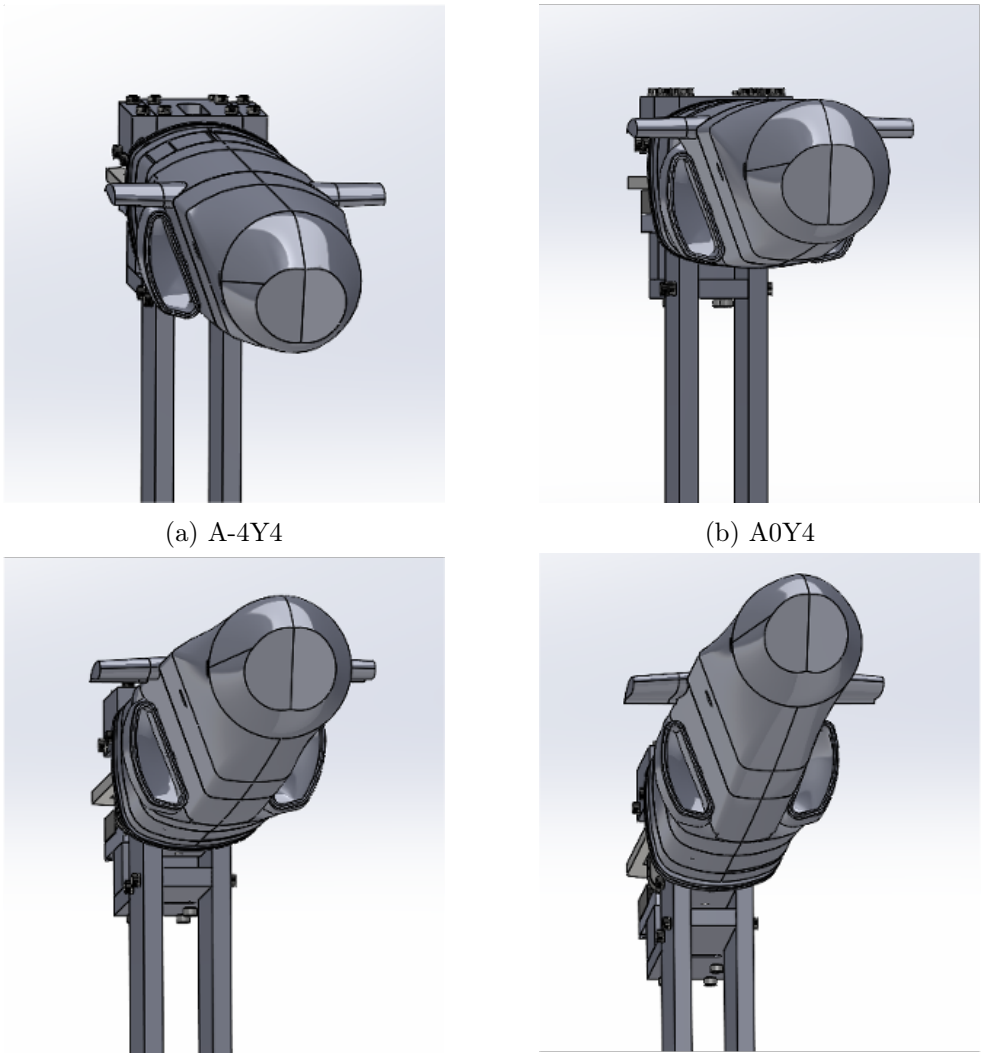

(a) A-4Y4 (b) A0Y4

(c) A4Y4 (d) A8Y4

Figure 4.17: Freestream Orientations of the Internal Aerodynamics Model at 4° Yaw Angle at Varying Angle-of-Attack.

Considering first the positive angles-of-attack, A4Y4 and A8Y4, it can be seen in Fig. 4.17 that the left side inlet, despite being on the leeward side of the yawed model, receives direct oncoming flow due to the positive angle-of-attack. For the A4Y4 orientation, both the left and right inlets matched Mach number very closely, with both being less than that of the A4Y0 case. The lower magnitude likely was caused by the combined effects of wing and

fuselage ram effect for the right intake and the increased ram effect present at the left intake compared to A4Y0.

For the A8Y4 orientation the left intake and wing surface were exposed to much of the flow. The pressure surface of the wing provided some external compression to the oncoming flow to further reduce the inlet entrance speed. The right intake shows a very small decrease in Mach number between A4Y4 and A8Y4 as a result of the increase in underside surface of the wing combined with a decrease in total blockage area around the intake, seen in Fig. 4.17d. This resulted in approximately the same amount of flow deceleration upstream of the inlet entrance.

The A-4Y4 orientation exhibits lower inlet entrance Mach numbers than were found for the A4Y0 case, with the right intake having a slightly higher entrance Mach number than the left. Similar to A0Y4, the left intake was obstructed by the fuselage to any direct flow in this orientation. It is hypothesized that the increased cross flow across the top of the model would be drawn downward towards the low pressure wake shed from the underside of the fuselage. The resulting increase in non-axial flow results in the lower entrance Mach compared to what was experienced for the A-4Y0 test. The described mechanism is sketched in Fig. 4.20. This hypothesis could be further investigated through flow visualization.

At A-4Y4 for the right intake, the yawed and negatively deflected wing possibly contributed to the generation of vortices from the leading edge. These secondary flows mix with the free stream to slow the oncoming flow, effectively leading to the reduced entrance Mach numbers. Total pressure recovery for 4° yaw and varying angles-of-attack are compared with the zero yaw orientations in Fig. 4.18.

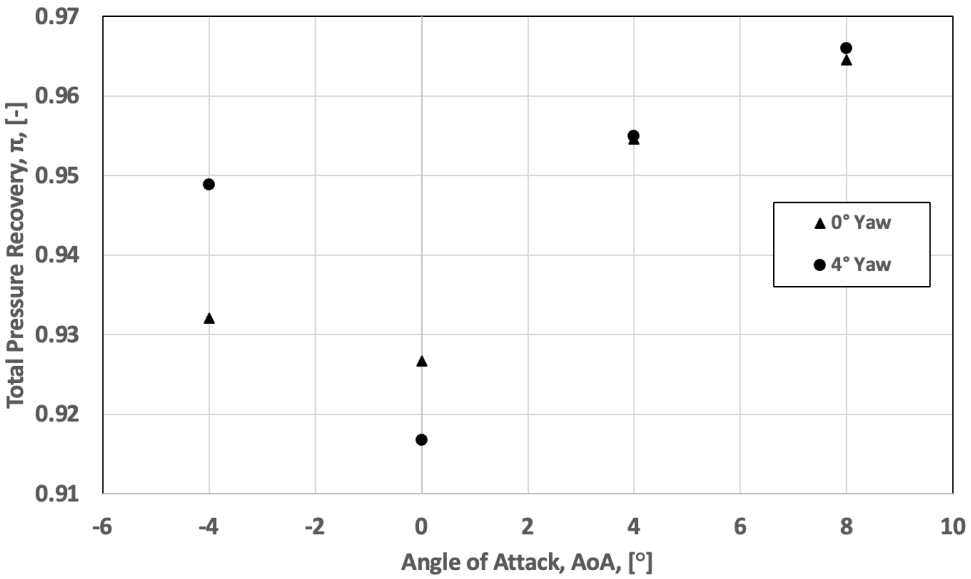

Figure 4.18: Effects of Angle-of-Attack and Yaw on Total Pressure Recovery at the Embedded Y-Duct AIP.

As expected based on the results for 0° yaw, the total pressure recovery at the AIP follows a similar trend when compared with the inlet entrance Mach number. Similar to A8Y0, A8Y4 exhibits the highest total pressure recovery of any yawed case investigated. This was a consequence of the lower intake Mach number and increased external compression caused by the aforementioned effects and flow turning. All other total pressure recoveries were relatively similar when reviewing the intake Mach numbers in Fig. 4.16 with the previous trends.

Total Pressure Recovery With Yaw and Angle-of-Attack

This section will detail and discuss the effects of yaw on the total pressure recovery of the embedded Y-duct. Total pressure recoveries are presented for 4° yaw with varying angle-of-attack in Fig. 4.19.

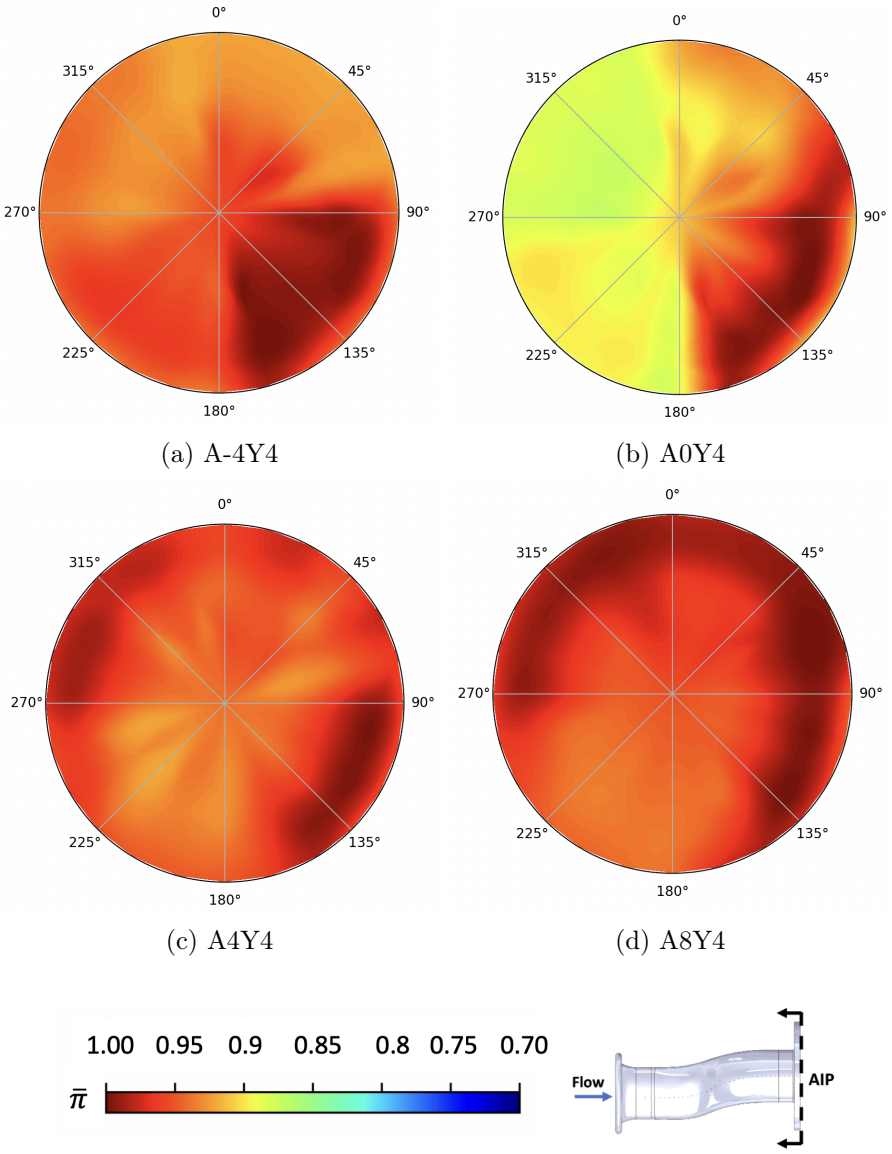

(a) A-4Y4 (b) A0Y4

(c) A4Y4 (d) A8Y4

Figure 4.19: Variation in Total Pressure Recovery with Angle-of-Attack.

0° Angle-of-Attack, 4° Yaw

The differences in total pressure recovery between the A0Y0 and A0Y4 orientations are evident when comparing Figures 4.14b and 4.19b. The region between 0° and 180°, centred around the 270° meridian for A0Y4 shows the effects of the blanked left intake. The left inlet in this case is situated along the leeward surface of the fuselage causing a zone of reduced pressure and consequently a lower total pressure recovery at the AIP. There was possibly also an influence of the vortices from the nose affecting the flow quality in the inlet at this orientation. The opposite side of the AIP corresponding to the windward intake, showed a similar pressure distribution as that shown in Fig. 4.14b but with much higher magnitudes of total pressure recovery despite the intake Mach number (see Fig. 4.16) being the highest of any orientation investigated. This Increased total pressure recovery, despite the high Mach number was aided by the right inlet's fully exposed position due to the side-slipped orientation. This increased the previously discussed ram effect on the intake as well as decreased the axial velocity through the duct from the required flow turning. The yawed orientation also reduced the flow travelling axially along the model which in turn reduced the influence of external boundary layer on the performance of the embedded Y-duct. This led to the slight increase in pressure recovery on the right hand side of the intake at this orientation, compared with A0Y0. However, the overall total pressure recovery at the AIP was low due to the poor recovery on the leeward side.

-4° Angle-of-Attack, 4° Yaw

In the A-4Y4 orientation, the right intake can be seen exposed to the oncoming flow while the left side intake is blocked. As expected, the total pressure recovery results in Fig. 4.19a exhibits an asymmetry due to the effect of yaw. The region between the 90° and 180° meridians show a local area of higher pressure recovery. This was similar to the lower regions of A-4Y0 where the ram effect decreased the inlet entrance speed which helped negate some influence of the vertical offsets, increasing total pressure recovery in this sector of the AIP. The magnitude of pressure recovery was greater at this orientation again due to the yaw angles influence on increased ram effect as well as flow turning angle at the right intake. The upper regions of the AIP between 90° and 270° centred around the 0° meridian, had higher pressure recovery than that for the A-4Y0 case. This increase in pressure recovery was due to the decrease in wing effect immediately upstream of the intake. Due to the non-chordwise flow over the wing at this orientation, the lower pressure region created on the lower

surface of the wing was less than that of the A-4Y0 case leading to slightly higher total pressure recoveries in this region. The side of the AIP centred around the 270° meridian for the A-4Y4 case had higher pressure recovery than that for the A0Y4 case. The change in model orientation could have caused increased cross flow over the top of the fuselage towards the leeward side of the model which was pulled downward by the seperated wake shed from the bottom of the model. This reduced axial velocity in the intake resulting in higher total pressure recovery on the associated side of the AIP. This behaviour is sketched in Fig. 4.20.

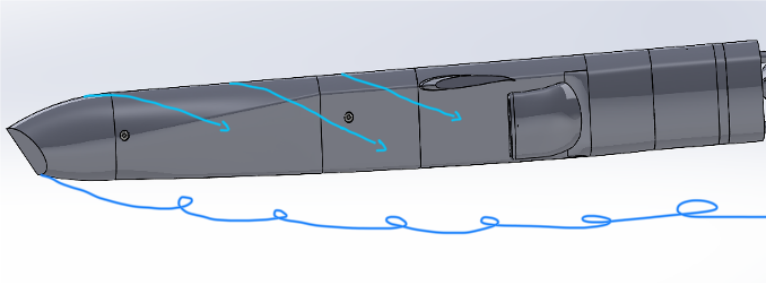

Figure 4.20: The Hypothesized Effect of Forebody Wake at A-4Y4.

4° Angle-of-Attack, 4° Yaw

In Fig. 4.17c, both inlets are seen to receive some direct freestream, despite the yaw angle. The pressure surface of the right main wing is also facing the oncoming flow. Between the 80° to 150° angles in Fig 4.19c, a similar area of high pressure recovery to that observed in the A4Y0 orientation is present. In the case of A4Y4 this area has increased slightly in size, likely related to the increased ram effect and flow turning at the entrance of the right intake of the duct with 4° of yaw. The half of the AIP centred about the 270° meridian exhibited some notable differences from that of A4Y0 orientation. The most prominent of these differences was the shift in location of high pressure recovery from around the 225° to the 315° angles on the A4Y0 AIP. This upwards shift is caused by the separated flow on the upper leeward side of the fuselage. Due to the orientation of the fuselage, a wake is generated downstream which influences air coming from under the model to flow upwards along the fuselage towards the downstream side of the model. This influences the direction of the air entering the intake, effectively increasing its angle-of-attack, causing a similar pressure distribution to what was seen for A8Y0. This is sketched in Fig. 4.21.

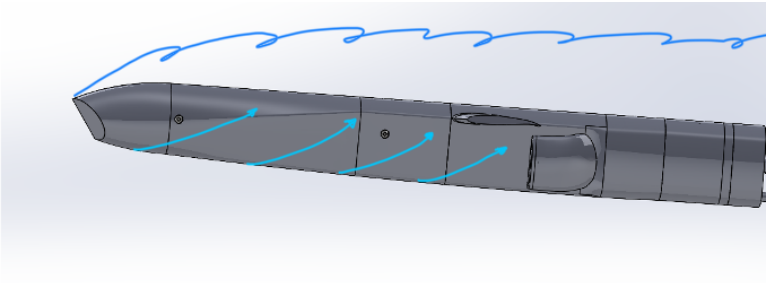

Figure 4.21: The Hypothesized Effect of Forebody Wake at A4Y4.

8° Angle-of-Attack, 4° Yaw

Figure. 4.17d shows that at A8Y4, both inlet entrances are exposed to the oncoming flow. Due to the combination of yaw angle and angle-of-attack at this orientation, the pressure surface of the wing had slightly lower blockage area directly above the intake. When comparing the total pressure recovery for A8Y4 in Fig. 4.19d with that of A8Y0 in Fig. 4.14d, the two orientations display relatively similar trends in total pressure recovery, with both model orientations featuring regions of higher total pressure recovery around the outer radii of the upper half of the AIP, situated around the 0° meridian. As discussed for the A8Y0 case, this upper concentration of high pressure recovery was a consequence of the positive angle-of-attack which increased ram effect and flow turning at the top of the inlet entrance eliminating some effect of the vertical bend within the embedded Y-duct. Consistent with A4Y4 results (see Fig. 4.19c), the A8Y4 orientation exhibited an area of pressure recovery greater both in size and magnitude in the lower region of the AIP from 90° to 150° angles than was noted for the A8Y0 case. The effect of the body wake again influenced the performance of the Y-duct at this orientation. The 270° meridian side (corresponding to the leeward intake) shows that regions of higher pressure recovery were swept upwards as compared to the A8Y0 case, and now concentrated mainly above the 270° angle. This is due to the increased static pressure of the flow as it impacts the windward side of the fuselage transiting under the model to the leeward side. The low pressure regions at the AIP from 170° to 270° angles could be caused by separated flow inside the lower lip of the left intake. Similar to the A8Y0 case, the high angle-of-attack at A8Y4 is hypothesized to have caused any vortices generated from the nose of the model to be directed over the fuselage leaving no impact on inlet performance.

4.2.5 Distortion Descriptors

The distortion descriptor results provide a quantitative comparison between total pressure distortion at different model orientations. Distortion descriptors for the 4° yaw tests are listed in Table 4.8.

Table 4.8: Distortion Coefficients for Tests at 4° Yaw.

Orientation	$DPRP_{max}$	$DPCP_{avg}$	$DC(60)$
A-4Y4	0.013 ± 0.0023	0.0179 ± 0.00046	0.43 ± 0.057
A0Y4	0.008 ± 0.0023	0.0285 ± 0.00059	0.78 ± 0.082
A4Y4	0.017 ± 0.0011	0.0109 ± 0.00036	0.4 ± 0.049
A8Y4	0.014 ± 0.0011	0.0193 ± 0.00033	0.57 ± 0.049

Table 4.8 compares the three pressure distortion coefficients examined in the scope of this work between the various yawed orientations. Considering $DPRP_{\max}$ first, no trend was present for increasing angle-of-attack with yaw. The highest magnitude of $DPRP_{\max}$ was calculated for the A4Y4 orientation (see Fig. 4.19c), occurring in the innermost ring. This corresponded to the area of lowest pressure recovery for A4Y4 compared with the average at its AIP. The lowest $DPRP_{\max}$ also was at the innermost ring for A0Y4 (see Fig. 4.19b). This makes sense due to the relative horizontal symmetry noted in the total pressure results. This meant that each of the 4 rings contained an almost equal amount of high and low pressure recovery, comparable with the AIP average.

The $DPCP_{\text{avg}}$ did not display any observable trend with angle-of-attack. The opposite results to $DPRP_{\max}$ were noted for this parameter for the A0Y4 case exhibiting the highest $DPCP_{\text{avg}}$ and A4Y4 displaying the lowest. This also can be visually inferred when inspecting the contour plots presented in Fig. 4.19c and 4.19b. Due to the abrupt circumferential total pressure changes in A0Y4, the $DPCP_{\text{avg}}$ for this orientation was the highest. The A4Y4 orientation had some near symmetry along the 45° - 225° axis. This led to the lowest circumferential distortion, and hence the lowest $DPCP_{\text{avg}}$. This matched the angle-of-attack of the lowest circumferential distortion noted for the unyawed orientations, occurring at 4°.

Similar to the previous two coefficients, $DC(60)$ showed no discernible trend with angle-of-attack at 4° yaw. As expected, the highest value of $DC(60)$

was found for the A0Y4 case between the 270° and 330° angles, corresponding to the lowest total pressure recovery measured at the AIP. The lowest $DC(60)$ was again expirenced by A4Y4 between 180° and 240° angles. This area again relates to the lowest total pressure recovery for this orientation. Qualitatively from Fig. 4.19c, the pressure distortion at this orientation was low due to the near symmetry observed in the results.

5 Conclusion

Experimental work was conducted at RMC to investigate the effects of a forebody on the performance of a twin-scoop Y-duct inlet in high subsonic flow. This was accomplished through the design, manufacture, and testing of two test articles based on the same design: an isolated Y-duct and a high subsonic air vehicle with the Y-duct embedded within it. The vehicle was designed with features representative of a modern air-launched cruise missile. The Y-duct was designed at RMC based on previous Y-duct work by Sidhu *et al.* [32]. Both test articles were tested in RMC's polysonic indraft windtunnel at Ma=0.8 with the isolated Y-duct also compared at Ma=0.63. The experimental campaign yielded some key findings in terms of the baseline effects of a forebody on Y-duct performance, the effect of yaw on performance, and wing installation location.

Compared to the isolated Y-duct, the performance of the embedded Y-duct with no model incidence or yaw angles was found to be quite different. Specifically, despite the internal aerodynamics model being exposed to a Ma=0.8 freestream flow, the entrance of the embedded Y-duct only encountered Ma=0.525. This highlighted both the impact of the forebody and the effect of blockage and losses through the duct exposed to a freestream. The decrease in entrance Mach was consistent with design predictions of Raymer [33]. Total pressure recovery was decreased at the aerodynamic interface plane (AIP) compared to that of the isolated Y-duct. Despite the lower entrance Mach number, the effects of freestream led to an additional 4.79% total pressure loss at the AIP compared with the isolated duct at Ma=0.63. These losses could be reduced depending on the amount of forebody surface area upstream of the inlet with total pressure losses decreasing when angle-of-attack was varied. A crucial next step in this research is to install the isolated Y-duct in the test section with no model in order to isolate its losses and influence on Mach number from that of the forebody. Conventional total pressure distortion parameters $DPRP_{\max}$ and $DPCP_{\text{avg}}$ were lower in the embedded duct; however,

$DC(60)$ increased, due to the reduced total pressure recovery at the AIP compared with that of the isolated duct. These results highlight the importance of optimizing the location of the intake along the forebody in order to reduce these upstream effects and improve performance. The design of a more effective boundary layer diverter might also attenuate some boundary layer related total pressure losses. This is not possible for boundary layer ingesting aircraft configurations, so the effect of upstream fuselage has much more significance to the designer. An investigation into different forebody configurations could help to further correlate design features and their influence on duct performance.

The effect of yaw on the internal aerodynamics model introduced asymmetric flow conditions between the duct entrances. At 4° yaw across all angles-of-attack, the leeward intake experienced lower intake Mach numbers than the exposed inlet did. This was due to the effect of fuselage blocking the freestream. It was however, impractical to confirm these hypotheses with the data presented in this thesis and instead future work should incorporate flow visualization to accomplish this task. At these same conditions, the Mach number of the leeward inlet was found to be lower than the windward inlet Mach number for all angles-of-attack except for 0°. This was likely due to the leeward inlet's exposure to the body wake of the model, resulting in lower local static pressure and decreased ram effect resulting in higher entrance Mach number on the leeward side. Despite the asymmetry in intake conditions with yaw, total pressure recovery at the AIP matched fairly closely with the 0° yaw results for all angles-of-attack, with the largest difference noted at -4° angle-of-attack. Though total pressure recoveries were similar, the total pressure distribution at the AIP and hence the total pressure distortion coefficients for 4° tests yaw varied compared to 0°. $DC(60)$ and $DPCP_{\text{avg}}$ were found to be lower for all conditions except -4° angle-of-attack, while 4° yaw results compared with those of the 0° yaw orientation. By contrast, $DPRP_{\text{max}}$ was found to be greater for all angles-of-attack at 0° yaw except for the 8° test which fell below that of the 4° yaw case. High pressure distortion and non-uniformity can be dangerous for a gas turbine engine, possibly leading to undesirable and potentially dangerous engine operations; it should be avoided as much as possible. It should be noted however, that an aircraft such as the one represented by the internal aerodynamics model would not likely be in phases of flight where such yaw angles were maintained for even the briefest periods of time. These findings are nevertheless important for aircraft such as fighter aircraft with similar intake configurations, where high manœuvrability may expose the aircraft to these asymmetric flying conditions for extended periods of time.

The angle-of-attack influence on the internal aerodynamics model further highlighted the effects of forebody and aircraft configuration on the performance of a Y-duct. The configuration of the internal aerodynamics model featured the main wing installed just above and upstream of the Y-duct inlet entrance. At 0° angle-of-attack, this situated the pressure surface of the wing just upstream of the inlet entrance, slightly slowing freestream in this region. At both 0° and 4° yaw, total pressure recovery of the Y-duct intake increased with angle-of-attack. It was hypothesized that positive angles-of-attack increased ram effect and required flow turning at the inlet entrance, decreased the upstream boundary layer on the fuselage, and further exposed the pressure surface of the wing to the freestream causing external compression. These mechanisms attenuated some flow losses caused by the vertical offset of the duct by decreasing the axial flow velocity through the duct. This trend that was evidenced by increasing total pressure recovery with increasing angle-of-attack and the highest total pressure recovery for both yaw angles was observed at 8° angle-of-attack. At -4° angle-of-attack, both yaw cases also recorded higher total pressure recovery than that observed at 0°. This was hypothesized to be caused by a decrease in boundary layer effects due to the decrease in wetted area, as well as an increased total pressure recovery from the reduced axial duct velocity at the negative angle-of-attack. Despite higher total pressure recovery compared to 0° angle-of-attack, -4° angle-of-attack conditions revealed increased pressure distortion coefficients and non-uniformity at the AIP compared to those at positive angles-of-attack. This was likely caused by the negative wing incidence angle upstream of the Y-duct entrance. The results suggest that the positioning of the wing and Y-duct used in the aircraft model configuration was generally effective. Usually aircraft, especially those with a lifting body such as the internal aerodynamics model, fly at a positive angle-of-attack during cruise with minimal time spent at negative angles. Having an aircraft with the wing positioned above the inlet could provide better intake performance, and subsequently better engine performance during cruise flight compared to other configurations. Further work on different forebody configurations could confirm these findings and further the understanding of the forebodies influence on duct performance.

6 Recommendations

Recommendations for both future work and the current experimental setup are presented here. In order to better understand the source of total pressure losses on the internal aerodynamics Y-duct, an isolated Y-duct should be tested in the internal aerodynamics model test section. This would isolate the losses in total pressure caused by the forebody from those of the Y-duct itself as well as provide further insight into the ducts losses and blockage and how they effect entrance Mach number. These results would help optimize a design in order to improve the performance at the AIP.

The current internal aerodynamics model would benefit from flow visualization over the model. This would improve the overall understanding and verify the current hypotheses of complex flow behaviours over the forebody near the inlets. This could lead to simple modifications to the shape of the forebody to evaluate their impact on the performance of the duct.

Perhaps the most logical next step into the research of forebody effects on Y-duct performance would be the testing of different forebody configurations. The model used in this work provided good insight into the effects of a representative high subsonic air vehicle forebody, however, the model itself is rather uniquely configured. The design of a modular test article would allow for the effects of different fuselage cross sections, wing placement, nose shaping, and other common features to be investigated. This would further the understanding of a forebody's influence on duct performance while also providing correlations between certain features and their effect on duct performance. Investigating the effects of different features would further the understanding of aircraft configurations and their effect on intake, and subsequently engine performance. Both were beyond the scope of this work. Furthermore, the flow downstream of the model could be adjusted in order to achieve different free stream Mach numbers in order to evaluate their effect on the performance of the Y-duct.

The current work required a manual adjustment of index angles for the total pressure rake at the AIP and this required partial disassembly of the test section. Originally, the design of the internal aerodynamics model included a small motor attached to the indexing rod in order to adjust the index angle remotely. With the setup used here, the motor was found to be lacking torque and unable to turn the index rod reliably. Future work using this rig would benefit from the introduction of a more powerful motor able to overcome the friction in the rotational system. This would save enormous amounts of time between test runs as well as allowing for increased accuracy and repeatability in terms of achieved index angles.

Further improvements to the current test set up should include the automation of the flow activation. The current RMC polysonic indraft wind tunnel relies on thick gasket paper to hold the pressure differential before a run is initiated manually. The cutting and installation of these paper shims is time-consuming and laborious. Improvements could be made to the tunnel activation procedure with the incorporation of an automated system such as a piston driven plug. This type of system would seal the pressure differential using a piston to hold a plug in place between the high pressure of the test section and low pressure of the vacuum tanks. This system would use compressed air to rapidly retract, allowing flow through the test section into the vacuum tanks. There currenlty exists a partially completed design of such a device at RMC which requires significant work required to achieve full operational capability. The completion and implementation of such a device would be a project at the level of a masters student in engineering at RMC. The future commissioning of this device would allow for more efficient testing using RMC's polysonic wind tunnel including time savings and consistent flow activation.

References

[1] C. Rider, "Passive Flow Control in an S-duct Intake," *Royal Military College of Canada*, 2021.

[2] D. Miller, *Internal Flow Systems*. BHRA (Information Services), 2 ed., 1990.

[3] B. Gilbart, C. Rider, A. Asghar, W. D. Allan, R. Stowe, and R. Pimentel, "Effect of Geometry Modification of a Double Entrance Y-duct Inlet on Aerodynamic performance With High Speed Flow." To be published, 2024.

[4] B. Gilbart, A. Asghar, T. Pistun, W. D. Allan, R. Stowe, and R. Pimentel, "Effect of Entrance Cross-Section on Bulk Swirl and Performance of an S-duct Inlet in High Subsonic Flow," in *Proceedings of ASME Turbo Expo 2023*, no. GT2023-104188, 2023.

[5] C. Aeroprobe, *Fast Response Probes– User Manual.*, 2016.

[6] Canadian Warplane Heritage Museum, "Canadair CT-114 Tutor." Available online, 2024. Accessed on: 2024-03-19.

[7] Tech. Sgt. Nicolas Myers, "U.S. Air Force Maj. Kristin Wolfe performs a demonstration in the F-35A Lightning II at the Reno Air Races in Reno, Nevada, Sept. 19, 2021." Available online, 2021. Accessed on: 2024-03-19.

[8] W. Dean, "Note on the Motion of Fluid in a Curved Pipe," *London, Edinburgh and Dublin Phil. Magazine and J. of Sci*, vol. 4(20), pp. 208–223, 1927.

[9] F. Aulehla, "Intake Swirl - A Major Distrubance Parameter in Engine/Intake Compatibility," *Messerschmitt-Boelkow-Blohm G.m.b.H.*, no. ICAS-82-4.8.1, 1982.

[10] T. Triantafyllou, T. Nikolaidis, M. Diakostefanis, and P. Pilidis, "Total Pressure Distortion Levels at the Aerodynamic Interface Plane of a Military Aircraft," *The Aeronautical Journal*, vol. 119, no. 1210, 2015.

[11] W. Davis and D. Goldstein, "Experimental Investigation at Supersonic Speeds of Twin-Scoop Duct Inlets of Equal Area: An Inlet Enclosing 61.5 Percent of the Maximum Circumference of the Forebody," *National Advisory Comittee for Aeronautics*, no. NACA-RM-A7J27, 1948.

[12] N. Martin and C. Holzhauser, "An Experimental Investigation at Large Scale of Single and Twin NACA Submerged Side Intakes at Several Angles of Sideslip," *Ames Aeronautical Laboratory, National Advisory Comitee For Aeronautics, Washingston, USA*, no. NACA-RM-A9F20, 1949.

[13] J. Stroud, "Experimental Investigation of the Effect of Forebody Bluntness on the Pressure Recovery and Drag of a Twin-Scoop Inlet-Body Combination at Mach Numbers of 1.4 and 1.7.," *National Advisory Comittee for Aeronautics*, no. NACA RM A51K14, 1952.

[14] K. Saha, S. Singh, and V. Seshardi, "Effect of Angle of Attack on the Performance of Twin Intake Duct," in *Proceedings of AIAA Fluid Dynamics Conference and Exhibit 2007*, no. AIAA 2007-4357, 2007.

[15] N. Singh, A. Rahim, and M. Islam, "Flow Characteristics of a Symmetric Y-shaped Diffusing Duct with Zero Yaw Angle," *Indian Journal of Engineering and Materials Sciences*, vol. 20, pp. 125–131, 2013.

[16] R. Anand and R. Sandeep, "Effect of Angle of Turn on Flow Characteristics of Y- Shaped Diffusing Duct Using CFD," *Institute of Electronics and Electrical Engineers*, 2011.

[17] D. Bowditch and R. Coltrin, "A Survey of lnlet/Engine Distortion Compatibility (invited-paper)," in *Proceedings of AIAA/SAE/ASME 19th Joint Propulsion Conference*, 1983.

[18] R. Singh, S. Singh, and V. Seshadri, "Effect of Corner Rounding on the Performance of The Double Offset Y-Shaped Aircraft Intake Duct," *Proceedings of the Institution of Mechanical Engineers, Part G: Journal of Aerospace Engineering*, vol. 222, pp. 969–983, 2008.

[19] S. Wellborn, B. Reichert, and T. Okiishi, "An Experimental Investigation of the Flow in a Diffusing S-Duct," *NASA*, 1992.

[20] A. El-Sayed and M. Emeara, "Aero-Engines Intake: A Review and Case Study," *Journal of Robotics and Mechanical Engineering Research*, vol. 1, no. 3, 2016.

[21] N. Martin and C. Holzhauser, "Analysis of Factors Influencing the Stability Characteristics of Symmetrical Twin-Intake Air-Induction Systems,"

[22] J. Seddon and J. Goldsmith, *Intake Aerodynamics*. AIAA Education Series, 1999.

[23] S. International, *A Methodology for Assessing Inlet Swirl Distortion*. Society of Automotive Engineers, 2022.

[24] S. Bharani, S. Singh, V. Sehsardi, and R. Chandramouli, "Effect of Angle-of-Turn on the Performance of Divided Intake Ducts," *Proceedings of the Institution of Mechanical Engineers, Part G: Journal of Aerospace Engineering*, 2004.

[25] M. Gopaliya, M. Kumar, S. Kumar, and S. Gopaliya, "Analysis of Performance Characteristics of S-shaped Diffuser with Offset," vol. 11, pp. 130–135, 2007.

[26] R. Singh, S. Singh, and V. Seshardi, "Performance and Flow Characteristics of Double-Offset Y-Shaped Aircraft Intake Ducts," *Journal of Aircraft*, vol. 45, no. 4, 2008.

[27] M. Gopaliya, P. Goel, S. Prashar, and A. Dutt, "CFD Analysis of Performance Characteristics of S-shaped Diffusers with Combined Horizontal and Vertical Offsets," *Computers and Fluids*, vol. 40, 2010.

[28] A. Asghar, W. Allan, M. LaViolette, D. Alexander, R. Stowe, and G. Ingram, "S-Duct Diffuser Offset-to-Length Ratio Effect on Aerodynamic Performance of Propulsion System Inlet of High Speed Aircraft," in *Proceedings of ASME Turbo Expo 2018 Turbomachinery Technical Conference and Exposition*, no. GT2018-76661, 2018.

[29] K. Saha, S. Singh, and V. Seshardi, "Computational Analysis on Flow Through Transition S-Diffusers: Effect of Inlet Shape," *Journal of Aircraft*, vol. 44, no. 1, 2007.

[30] A. Asghar, R. Stowe, W. Allan, and D. Alexander, "Entrance Aspect Ratio Effect on S-duct Inlet Performance at High-Subsonic Flow," in *Proceedings of ASME Turbo Expo 2016: Turbomachinery Technical Conference and Exposition*, no. GT2016-57875, 2016.

[31] T. Patel, S. Singh, and V. Seshadri, "Characteristics of Y-Shaped Rectangular Diffusing Duct at Different Inflow Conditions," *Journal of aircraft*, vol. 42, no. 1, 2004.

[32] S. Sidhu, A. Asghar, W. D. Allan, R. Stowe, and R. Pimentel, "Internal Aerodynamic Performance Evaluation of Double Entrance S-Duct Intake at Moderately High Subsonic Mach Number.," in *Proceedings of ASME Turbo Expo 2021*, no. GT2021-58849, 2021.

[33] D. P. Raymer, *Aircraft Design: A Conceptual Approach*. 4 ed., 2006.

[34] A. Asghar, S. Pym, W. Allan, M. LaViolette, and R. Stowe, "Pressure Equilization Method For Passive Flow Control of an S-Duct Intake for High Subsonic Speeds.," in *Proceedings of ASME Turbo Expo 2018 Turbomachinery Technical Conference and Exposition*, 2018.

[35] I. Ibrahim, E. Ng, and K. Wong, "Applying Taguchi's Off-Line Quality Control Method and ANOVA on the Maneuverability of the F-5E Intake," *Mathematical and Computer Modelling*, 2009.

[36] F. Lazeroni and F. Pfyl, "Effect of Boundary-Layer Control and Inlet Lip Shape on the Performance of a Twin-Scoop Air-Induction System at Mach Numbers from 0 to 1.9.," *National Advisory Comittee for Aeronautics*, no. NACA RM A55L02, 1956.

[37] K. Saha, S. Singh, and V. Seshadri, "Effect of Yaw Angle on the Performance Characteristics of Twin Intake Duct," *Journal of aircraft*, vol. 53, no. 3, 2017.

[38] H. Bean, *Fluid Meters, Their Theory and Application.* American Society of Mechincal Engineers, 6th ed., 1971.

[39] B. Bouldin and Y. Sheoran, "Inlet Flow Angularity Descriptors Proposed for Use with Gas Turbine Engines," *World Aviation Congress and Display*, no. SAE 2002-01-2919, 2002.

[40] NASA Glenn Research Center, "Inlets." Available online, 2021. https://www.grc.nasa.gov/www/k-12/airplane/inlet.html.

[41] M. Gopaliya, P. Jain, S. Kumar, V. Yadav, and S. Singh, "Performance Improvement of S-shaped Diffuser Using Momentum Imparting Technique," *Journal of Mechanical and Civil Engineering*, vol. 11, pp. 23–31, 2015.

[42] A. Paul, P. Ranjan, R. Upadhyay, and A. Jain, "Passive Flow Control through a Y-shaped Air Intake," in *Proceedings of ICTACEM 2010 International Conference on Theoretical, Applied, Computational and Experimental Mechanics*, 2010.

Appendices

A Uncertainty Analysis

Uncertainty evaluations were carried out on the calculated performance metrics. The uncertainty of a parameter was found using the partial derivative and root sum squared (RSS) methods. Uncertainties for values which were averaged were found as the root sum of the squared standard deviation and instrument uncertainties. This remainder of this section details the equations used to find uncertainty for each performance metric evaluated.

A.1 Coefficient of Static Pressure, $C_{p,x}$

The coefficient of static pressure, $C_{p,x}$ was first given in Equation 3.1. It is given again here in Equation A.1 with the uncertainty for coefficient of static pressure shown in Equation A.2.

$$C_{p,x} = \frac{p_{s,x} - p_{s,1}}{p_{0,1} - p_{s,1}} \tag{A.1}$$

$$\delta_{C_{p,x}} = \sqrt{\left(\frac{1}{p_{0,1} - p_{s,1}}\delta_{p_{s,x}}\right)^2 + \left(\frac{p_{s,x} - p_{0,1}}{{p_{0,1} - p_{s,1}}^2}\delta_{p_{s,1}}\right)^2 + \left(\frac{-(p_{s,x} - p_{s,1})}{(p_{0,1} - p_{s,1})^2}\delta_{p_{0,1}}\right)^2} \tag{A.2}$$

A.2 Total Pressure Recovery, $\overline{\pi}$

The coefficient of total pressure recovery, $\overline{\pi}$ was first given in Equation 3.2. It is given again here in Equation A.3 with the uncertainty for coefficient of total pressure recovery shown in Equation A.4.

$$\overline{\pi} = \frac{\overline{p_{0,2}}}{p_{0,1}} \tag{A.3}$$

$$\delta_{\overline{\pi}} = \sqrt{\left(\frac{\overline{p_{0,2}}}{p_{0,1}}\delta_{p_{0,1}}\right)^2 + \left(\frac{1}{p_{0,1}}\delta_{\overline{p_{0,2}}}\right)^2} \tag{A.4}$$

A.3 Pressure Distortion, $DC(j)$

The pressure distortion in the worst j degree sector at the AIP, $DC(j)$ was first given in Equation 3.4. It is given again here in Equation A.5 with the uncertainty for the pressure distortion shown in Equation A.6.

$$DC(j) = \left(\frac{\overline{p_{0,2}} - \overline{p_{0,j}}}{\overline{p_{0,2}} - \overline{p_{s,2}}}\right)_{\max} \tag{A.5}$$

$$\delta_{DC(j)} = \sqrt{\left(\frac{\overline{p_{0,j}} - \overline{p_{s,2}}}{(\overline{p_{0,2}} - \overline{p_{s,2}})^2}\delta_{\overline{p_{0,2}}}\right)^2 + \left(\frac{-1}{(\overline{p_{0,2}} - \overline{p_{s,2}})}\delta_{\overline{p_{0,j}}}\right)^2 + \left(\frac{\overline{p_{0,2}} - \overline{p_{0,j}}}{(\overline{p_{0,2}} - \overline{p_{s,2}})^2}\delta_{\overline{p_{s,2}}}\right)^2} \tag{A.6}$$

A.4 Radial Distortion Descriptor, $DPRP_{\max}$

The radial distortion descriptor, $DPRP_{\max}$ was first given in Equation 3.5. It is given again here in Equation A.7 with the uncertainty for the radial distortion descriptor shown in Equation A.8.

$$DPRP_{\max} = \left(\frac{\overline{p}_{0,2} - \overline{p}_{0,2,i}}{\overline{p}_{0,2}}\right)_{\max} \tag{A.7}$$

$$\delta_{DPRP_{\max}} = \sqrt{\left(\frac{\overline{p}_{0,2,i}}{\overline{p_{0,2}}^2}\delta_{\overline{p_{0,2}}}\right)^2 + \left(\frac{-1}{\overline{p_{0,2}}}\delta_{\overline{p}_{0,2,i}}\right)^2} \tag{A.8}$$

A.5 Circumferential Distortion Descriptor, $DPCP_{\text{avg}}$

The radial circumferential descriptor, $DPCP_{\text{avg}}$ was first given in Equation 3.6. It is given again here in Equation A.9. Due to its more complex piecewise form the uncertainty for the circumferential distortion descriptor shown in Equations A.10, A.11, and A.12. Note the form given here is for the isolated Y-duct.

$$DPCP_{\text{avg}} = \frac{1}{5}\sum_{i=1}^{5}\left(1 - \frac{\sum_{k=1}^{12}\begin{cases}\frac{\overline{p}_{0,2,i,k}}{\overline{p}_{0,2,i,}} & \overline{p}_{0,2,i,k} < \overline{p}_{0,2,i,} \\ 0 & \overline{p}_{0,2,i,k} \geq \overline{p}_{0,2,i,}\end{cases}}{\sum_{k=1}^{12}\begin{cases}1 & \overline{p}_{0,2,i,k} < \overline{p}_{0,2,i,} \\ 0 & \overline{p}_{0,2,i,k} \geq \overline{p}_{0,2,i,}\end{cases}}\right) \tag{A.9}$$

$$\frac{\delta DPCP_{\text{avg}}}{\delta\overline{p}_{0,2,i,k}} = \frac{1}{5}\sum_{i=1}^{5}\left(1 - \frac{\sum_{k=1}^{12}\begin{cases}\frac{1}{\overline{p}_{0,2,i,}} & \overline{p}_{0,2,i,k} < \overline{p}_{0,2,i,} \\ 0 & \overline{p}_{0,2,i,k} \geq \overline{p}_{0,2,i,}\end{cases}}{\sum_{k=1}^{12}\begin{cases}1 & \overline{p}_{0,2,i,k} < \overline{p}_{0,2,i,} \\ 0 & \overline{p}_{0,2,i,k} \geq \overline{p}_{0,2,i,}\end{cases}}\right) \tag{A.10}$$

$$\frac{\delta DPCP_{\text{avg}}}{\delta\overline{p}_{0,2,i}} = \frac{1}{5}\sum_{i=1}^{5}\left(1 - \frac{\sum_{k=1}^{12}\begin{cases}\frac{-\overline{p}_{0,2,i,k}}{(\overline{p}_{0,2,i,})^2} & \overline{p}_{0,2,i,k} < \overline{p}_{0,2,i,} \\ 0 & \overline{p}_{0,2,i,k} \geq \overline{p}_{0,2,i,}\end{cases}}{\sum_{k=1}^{12}\begin{cases}1 & \overline{p}_{0,2,i,k} < \overline{p}_{0,2,i,} \\ 0 & \overline{p}_{0,2,i,k} \geq \overline{p}_{0,2,i,}\end{cases}}\right) \tag{A.11}$$

$$\delta_{DPCP_{\text{avg}}} = \sqrt{\left(\frac{\delta DPCP_{\text{avg}}}{\delta\overline{p}_{0,2,i,k}}\delta_{\overline{p}_{0,2,i,k}}\right)^2 + \left(\frac{\delta DPCP_{\text{avg}}}{\delta\overline{p}_{0,2,i}}\delta_{\overline{p}_{0,2,i}}\right)^2} \tag{A.12}$$

A.6 Swirl Intensity, SI

The simplified swirl intensity, SI, was first given in Equation 3.8. It is given again here in Equation 3.8 with the uncertainty for the simplified swirl intensity shown in Equation A.14.

$$SI = \overline{|\alpha|} \tag{A.13}$$

$$\delta_{SI} = \sqrt{\left(\frac{u^2}{{u_\theta}^2 + u^2}\delta_{u_\theta}\right)^2 + \left(\frac{-{u_\theta}^2}{{u_\theta}^2 + u^2}\delta_u\right)^2} \tag{A.14}$$

A.7 Swirl Directivity, SD

The simplified swirl directivity, SD, was first given in Equation 3.11. It is given again here in Equation A.15 with the uncertainty for the simplified swirl directivity shown in Equation A.16.

$$SD = \frac{\overline{\alpha}}{|\overline{\alpha}|} \tag{A.15}$$

$$\delta_{SD} = \sqrt{\left(\frac{1}{|\overline{\alpha}|}\delta_{\overline{\alpha}}\right)^2 + \left(\frac{-\overline{\alpha}}{|\overline{\alpha}|^2}\delta_{|\overline{\alpha}|}\right)^2} \tag{A.16}$$

A.8 Swirl Pairs, SP

The simplified swirl pairs, SP, was first given in Equation 3.13. It is given again here in Equation A.17 with the uncertainty for the simplified swirl pairs shown in Equation A.18 and A.19 for maximum values of α^+ and α^- respectively.

$$SP = \frac{|\overline{\alpha}|}{2 \times max\left[\overline{\alpha}^-, \overline{\alpha}^+\right]} \tag{A.17}$$

$$\delta_{SP^+} = \sqrt{\left(\frac{1}{\overline{\alpha}^+}\delta_{|\overline{\alpha}|}\right)^2 + \left(\frac{-|\overline{\alpha}|}{2\overline{\alpha}^+}\delta_{\overline{\alpha}^+}\right)} \tag{A.18}$$

$$\delta_{SP^-} = \sqrt{\left(\frac{1}{\overline{\alpha}^-}\delta_{|\overline{\alpha}|}\right)^2 + \left(\frac{-|\overline{\alpha}|}{2\overline{\alpha}^-}\delta_{\overline{\alpha}^-}\right)} \tag{A.19}$$

B Aeroprobe

The 5-hole *Aeroprobe* ER-FRP was calibrated to $\pm$ 50° for subsonic flows. It had a resolution of $\pm$ 1°.

The velocity vector was defined with respect to the probe using the flow angles $(\alpha, \beta, \theta, \phi)$ and the velocity magnitude (V). Figure B.1 below shows the two coordinate systems that were used to describe the angle of the fluid flow relative to the probe. The first is a standard spherical coordinate system where the azimuthal angle (roll) is denoted by $\phi(0 \leq \phi \leq 2\pi)$ and the polar angle (cone)is denoted by $\theta(0 \leq \theta \leq \pi)$. The second coordinate system is a wind-axis system, in which, the angle of attack (α) is measured from the probe longitudinal axis to the projection of the wind direction onto the Xp - Zp plane. The angle of sideslip (β) is measured from the projection of the wind direction onto the Xp - Zp plane to the wind vector. The $\alpha - \beta$ coordinates are derived from the velocity components in post processing. The relationship between the velocity components and the $\theta - \phi$ angles and $\alpha - \beta$ angles are given as follows where u, v, and w are the velocity components in the x, y, and z directions respectively [5].

$$u = V \cos\theta \tag{B.1}$$

$$v = V \sin\theta \cos\phi \tag{B.2}$$

$$w = V \sin\theta \sin\phi \tag{B.3}$$

Where:

$$\alpha = \arctan\frac{w}{u} = \arctan[\tan\theta \sin\phi] \tag{B.4}$$

and

$$\beta = \arctan\frac{v}{V} = \arcsin[\sin\theta \cos\phi] \tag{B.5}$$

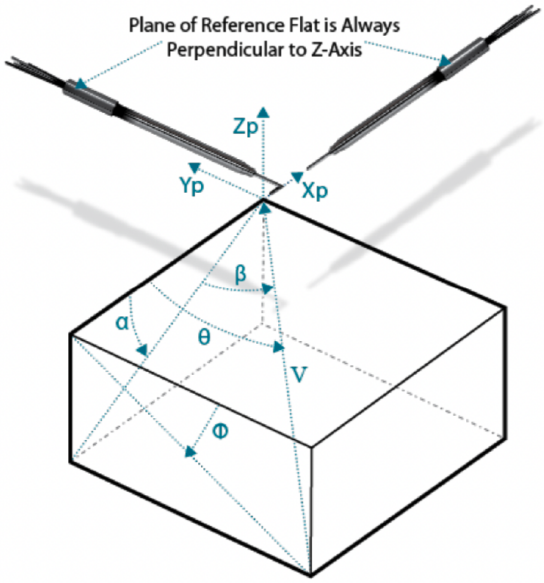

Figure B.1: *Aeroprobe* Configuration Options [5].

C Sample Code

C.1 Isolated Y-duct Contour Plot from [1]

```
%% Coefficient Calculations
% Courtney Rider
% March 11 2021
clear all
close all
% clc

%% Import Data
Duc = 4; % not 0 = baseline, 3 = FC3, 4 = FC4

if Duc ==0
    StitchedLocation = '01_Sept_2020_Baseline\AeroprobeData_Smooth'; %File location to stitched files
    Duc = '16149-1_AeroPressure_Baseline_TP_'; %S-duct geometry in file name
elseif Duc ==3
    StitchedLocation = '05_August_2020_FC3\AeroprobeData_Smooth'; %File location to stitched files
    Duc = '16149-1_AeroPressure_FC3_TP_'; %S-duct geometry in file name
elseif Duc ==4
    StitchedLocation = 'AeroprobeData_Smooth'; %File location to stitched files
    Duc = '16149-1_AeroPressure_Round-InletM0.80_TP_'; %S-duct geometry in file name
end

Angle = 30; %Angle inbetween traverse in degrees (000,030,060,090,120,150,180)
StartAngle = 000; %Begining angle in degrees
EndAngle = 330; %Final swept angle in degrees
P_inf = 14.7556; % Atmospheric pressure in PSI average of 101.2 and 101.4

n = 30000; %Steps to center of duct

%%
% 1 - time
% 5 - u(ft/s)
% 6 - v(ft/s)
% 7 - w(ft/s)
% 8 - Velocity(ft/s)
% 9 - Mach
% 10 - Density(lb/ft^3)
% 11 - Po(psi)
% 12 - Ps(psi)
% 13 - To(C)
% 14 - Ts(C)
% 15 - Cone(deg)
% 16 - Roll(deg)
% 17 - Pitch(deg)
% 18 - Yaw(deg)
% 19 - Error

%% Coefficients
P02 = zeros(n,length(StartAngle:Angle:EndAngle));
alpha = zeros(n,length(StartAngle:Angle:EndAngle));

for j = 1:EndAngle/Angle+1
    % Get angle and run number in the format needed for file name
    p = (j-1) * Angle;
    if p==0
        Agl = '000';
    elseif p<100&&p>10
        Agl = ['0',num2str(p)];
    else
        Agl = num2str(p);
    end

    % Import data
    nameStitched = [num2str(StitchedLocation),'\',num2str(Duc),'_A',num2str(Agl),'_T_','.txt']; % Post processed file name
    StitchedData = importdata(nameStitched);

    % Average Data
```

```
    P02(:,j) = StitchedData(:,11);
    alpha(:,j) = atan(StitchedData(:,7)./StitchedData(:,5));
end

%% AVERAGE TO 1000 Points radially
n1 = 40;
Stitched = zeros(n,size(StitchedData,2));

%% AREA AVERAGE
R = 2; % inches, outer radius of duct at AIP
ro = linspace(R, R/n, n);
ri = linspace(R-R/n, 0, n);
A_Sec_Ave = pi*(ro.^2 - ri.^2)*Angle/(EndAngle+Angle);
A_Total = sum(A_Sec_Ave)*(EndAngle+Angle)/Angle;

P02_Ave = zeros(n1,size(P02,2)+1);
alpha_Ave = zeros(n1,size(P02,2)+1);

for i = 1:n1
    a = (i-1)*n/n1 +1;
    b = i*n/n1;
    for j = 1:size(P02,2)
        P02_Ave(i,j) = sum(A_Sec_Ave(a:b) * P02(a:b,j))/sum(A_Sec_Ave(a:b));
        alpha_Ave(i,j) = sum(A_Sec_Ave(a:b) * alpha(a:b,j))/sum(A_Sec_Ave(a:b))*180/pi;
    end
end
P02_Ave(:,end) = P02_Ave(:,1);
alpha_Ave(:,end) = alpha_Ave(:,1);

Pi = P02_Ave/P_inf;

%% PLOT
rho = linspace(1,0,size(Pi,1));
theta = StartAngle/180*pi:Angle/180*pi:(EndAngle+Angle)/180*pi;
[thg,rg] = meshgrid(theta,rho);
[Xi,Yi] = pol2cart(thg,rg);

% clockwise plot -y
% looking downstream
figure(1)
hold on
contourf(Xi,-Yi,Pi,20,'LineStyle','none');
colorbar;
colormap(jet)
caxis([0.7 1]);
xlabel('\ity','Fontsize',12,'Fontname','Times New Roman','Fontweight','n','LineStyle',
'none');
ylabel('\itx','Fontsize',12,'Fontname','Times New Roman','Fontweight','n','LineStyle',
'none');
%title('Total Pressure','Fontsize',15,'Fontname','Times New
Roman','Fontweight','n','LineStyle','none');
c = colorbar;
c.Title.String = '\pi';
c.Title.FontSize = 15;
view(270,90);
text(0.935,-0.6,'0^\circ','Fontsize',15,'Fontname','Times New Roman','Fontweight','n')
X = [0.61 0.5];
Y = [0.9 0.915];
annotation('arrow',X,Y,'Linewidth',2);
set(gca,'Linewidth',2,'Fontname','Times New Roman');
text(-0.92,-0.6,'180^\circ','Fontsize',15,'Fontname','Times New Roman','Fontweight','n')
X = [0.61 0.5];
Y = [0.13 0.12];
annotation('arrow',X,Y,'Linewidth',2);
set(gca,'Linewidth',2,'Fontname','Times New Roman');
grid off;
box on;
axis square;
shading flat;
```

```
figure(2)
hold on
contourf(Xi,-Yi,alpha_Ave,20,'LineStyle','none')
colorbar;
colormap(jet)
caxis([-20 20]);
xlabel('\ity','Fontsize',12,'Fontname','Times New Roman','Fontweight','n','LineStyle',
'none');
ylabel('\itx','Fontsize',12,'Fontname','Times New Roman','Fontweight','n','LineStyle',
'none');
%title('Swirl Angle','Fontsize',15,'Fontname','Times New
Roman','Fontweight','n','LineStyle','none');
c = colorbar;
c.FontSize = 12;
c.Title.String = '\alpha(degrees)';
c.Title.FontSize = 15;
view(270,90);
text(0.935,-0.6,'0^\circ','Fontsize',15,'Fontname','Times New Roman','Fontweight','n')
X = [0.61 0.5];
Y = [0.9 0.915];
annotation('arrow',X,Y,'Linewidth',2);
set(gca,'Linewidth',2,'Fontname','Times New Roman');
text(-0.92,-0.6,'180^\circ','Fontsize',15,'Fontname','Times New Roman','Fontweight','n')
X = [0.61 0.5];
Y = [0.13 0.12];
annotation('arrow',X,Y,'Linewidth',2);
set(gca,'Linewidth',2,'Fontname','Times New Roman');
grid off;
box on;
axis square;
shading flat;
```

C.2 Isolated Y-duct Coefficients from [1]

```
%% Coefficient Calculations
% Courtney Rider
% March 11 2021
clear all
close all
% clc

%% Import Data
Duc = 4; % not 0 = baseline, 3 = FC3, 4 = FC4

if Duc ==0
    StitchedLocation = '01_Sept_2020_Baseline\AeroprobeData_Smooth'; %File location to stitched files
    Duc = '16149-1_AeroPressure_Baseline_TP_'; %S-duct geometry in file name
elseif Duc ==3
    StitchedLocation = '05_August_2020_FC3\AeroprobeData_Smooth'; %File location to stitched files
    Duc = '16149-1_AeroPressure_FC3_TP_'; %S-duct geometry in file name
elseif Duc ==4
    StitchedLocation = 'AeroprobeData_Smooth'; %File location to stitched files
    Duc = '16149-1_AeroPressure_Round-InletM0.80_TP_'; %S-duct geometry in file name
end

Angle = 30; %Angle inbetween traverse in degrees (000,030,060,090,120,150,180)
StartAngle = 000; %Begining angle in degrees
EndAngle = 330; %Final swept angle in degrees
P_inf = 14.7556; % Atmospheric pressure in PSI average of 100.8 and 101.2

n = 30000; %Steps to center of duct

%%
% 1 - time
% 5 - u(ft/s)
% 6 - v(ft/s)
% 7 - w(ft/s)
% 8 - Velocity(ft/s)
% 9 - Mach
% 10 - Density(lb/ft^3)
% 11 - Po(psi)
% 12 - Ps(psi)
% 13 - To(C)
% 14 - Ts(C)
% 15 - Cone(deg)
% 16 - Roll(deg)
% 17 - Pitch(deg)
% 18 - Yaw(deg)
% 19 - Error

%% Coefficients
P02 = zeros(n,length(StartAngle:Angle:EndAngle));
Ps2 = zeros(n,length(StartAngle:Angle:EndAngle));
alpha = zeros(n,length(StartAngle:Angle:EndAngle));
SI_U = zeros(n,length(StartAngle:Angle:EndAngle));
SI_V = zeros(n,length(StartAngle:Angle:EndAngle));

for j = 1:EndAngle/Angle+1
    % Get angle and run number in the format needed for file name
    p = (j-1) * Angle;
    if p==0
        Agl = '000';
    elseif p<100&&p>10
        Agl = ['0',num2str(p)];
    else
        Agl = num2str(p);
    end

    % Import data
    nameStitched = [num2str(StitchedLocation),'\',num2str(Duc),'_A',num2str(Agl),'_T_','.txt']; % Post processed file name
```

```
    StitchedData = importdata(nameStitched);

    % Average Data
    P02(:,j) = StitchedData(:,11);
    Ps2(:,j) = StitchedData(:,12);
    alpha(:,j) = atan(StitchedData(:,7)./StitchedData(:,5))*180/pi;
    % Uncertainty values for SI
    SI_V(:,j) = StitchedData(:,7).^2./(StitchedData(:,5).^2 + StitchedData(:,7).^2);
    SI_U(:,j) = - StitchedData(:,5).^2./(StitchedData(:,5).^2 + StitchedData(:,7).^2);

end

%% AVERAGE TO 1000 Points radially
n1 = 1000;
Stitched = zeros(n,size(StitchedData,2));

%% AREA AVERAGE
R = 2; % inches, outer radius of duct at AIP
ro = linspace(R, R/n, n);
ri = linspace(R-R/n, 0, n);
A_Sec_Ave = pi*(ro.^2 - ri.^2)*Angle/(EndAngle+Angle);

A_Total = sum(A_Sec_Ave)*(EndAngle+Angle)/Angle;

P02_AAve = zeros(n1,size(P02,2));
Ps2_AAve = zeros(n1,size(P02,2));
alpha_AAve = zeros(n1,size(P02,2));
SI_U_AAve = zeros(n1,size(P02,2));
SI_V_AAve = zeros(n1,size(P02,2));

for i = 1:n1
    a = (i-1)*n/n1 +1;
    b = i*n/n1;
    for j = 1:size(P02,2)
        P02_AAve(i,j) = sum(A_Sec_Ave(a:b) * P02(a:b,j));
        Ps2_AAve(i,j) = sum(A_Sec_Ave(a:b) * Ps2(a:b,j));
        alpha_AAve(i,j) = sum(A_Sec_Ave(a:b) * alpha(a:b,j));
        SI_U_AAve(i,j) = sum(A_Sec_Ave(a:b) * SI_U(a:b,j));
        SI_V_AAve(i,j) = sum(A_Sec_Ave(a:b) * SI_V(a:b,j));
    end
end


%% Determining the P02j for each sector
sector = 360/60; % 6 sectors at the AIP
P02j_AAve = zeros(1,size(P02_AAve,2));

k = 1;
% ************* THIS IS BASED ON USING AN ANGLE OF 30 ***************
if Angle ~= 30
    error('Update P02j calculation. It is set up for angle of 30 deg only')
end

for i = 1:size(P02j_AAve,2)
    if i < size(P02_AAve,2)-2
        P02j_AAve(i) = sum(P02_AAve(:,i)*0.5 + P02_AAve(:,i+1) + P02_AAve(:,i+2)*0.5);
    elseif i == size(P02_AAve,2)-2
        P02j_AAve(i) = sum(P02_AAve(:,i)*0.5 + P02_AAve(:,i+1) + P02_AAve(:,1)*0.5);
    elseif i == size(P02_AAve,2)-1
        P02j_AAve(i) = sum(P02_AAve(:,i)*0.5 + P02_AAve(:,k) + P02_AAve(:,k+1)*0.5);
    else
        P02j_AAve(i) = sum(P02_AAve(:,k)*0.5 + P02_AAve(:,k) + P02_AAve(:,k+1)*0.5);
        k = k+1;
    end
end

A_Sector = A_Total/sector;
%% Outputs and Uncertainties:
P_max = 5; %psi
```

```
u_max = 3.5; %in/s
v_max = 3.5; %in/s
nDAQ = 600;
w_u = .01*u_max/sqrt(n);
w_vtheta = .01*v_max/sqrt(n);

w_Psx = .0005*5/sqrt(nDAQ);
w_Ps1 = .0005*5/sqrt(nDAQ);
w_P01 = .01*P_max/sqrt(n); %CHANGE???***
w_P0j = .01*P_max/sqrt(n)/sqrt(3);
w_Ps2 = .01*P_max/sqrt(n);
w_P02ik = .01*P_max/sqrt(n);
w_P02i = .01*P_max/sqrt(n);
w_P02 = .01*P_max/sqrt(n);

%% Distortion Coefficient - DC(60)
Ps2_bar = sum(sum(Ps2_AAve))/A_Total;
P02_bar = sum(sum(P02_AAve))/A_Total;
P02j_bar = P02j_AAve/A_Sector;

Cdis = (P02_bar - P02j_bar)/(P02_bar - Ps2_bar);

Cdis_P02 = (P02j_bar - Ps2_bar)./(P02_bar - Ps2_bar).^2;
Cdis_P0j = 1/(Ps2_bar - P02_bar);
Cdis_Ps2 = (P02_bar - P02j_bar)/(P02_bar - Ps2_bar)^2;
w_Cdis = sqrt((Cdis_P02*w_P02).^2 + (Cdis_P0j*w_P0j).^2 + (Cdis_Ps2*w_Ps2).^2 );
[Dis, I] = max(Cdis);

fprintf('Circumferential distortion coefficient: DC(60) = %.5f +/- %.5f in sector %.0f\n'
,Dis, w_Cdis(I),I);
A2 = Angle * I;
A1 = A2 - 60;
fprintf('Total number of sectors %.0f, it is at an angle of %.0f to %.0f degrees \n',size
(Cdis, 2),A1,A2)

%% Radial Distortion Coefficient (DPRPmax)
clear ro ri
RadialPoints = 5;
% AREA AVERAGE
A_Radial = A_Total/RadialPoints;
ro = R;
for i = 1:RadialPoints
    ri(i) = sqrt(ro(i)^2 - A_Radial/pi);
    ro(i+1) = ri(i);
end

step_x = R/size(P02_AAve,1); % Step distance in inches
P02i_AAve = zeros(RadialPoints,1);
P02ik_AAve = zeros(RadialPoints,size(P02_AAve,2));
for j = 1:length(ri)
    for i = 1:size(P02_AAve,1)
        if ro(j) >= R - step_x*i && R - step_x*i > ri(j)
            P02i_AAve(j) = P02i_AAve(j) + sum(P02_AAve(i,:));
            P02ik_AAve(j,:) = P02ik_AAve(j,:) + P02_AAve(i,:);
        end
    end
end

P02i_bar = P02i_AAve/A_Radial;
P02ik_bar = P02ik_AAve/(A_Radial*Angle/(EndAngle+Angle));

Cr = (P02_bar - P02i_bar)/P02_bar;

Cr_P02 = P02i_bar/P02_bar;
Cr_P02i = -1/P02_bar;

w_Cr = sqrt((Cr_P02*w_P02).^2 + (Cr_P02i*w_P02i).^2);

[r_coef, I] = max(Cr);
```

```
fprintf('Radial distortion coefficient: DRPR max = %.5f +/- %.5f\n',r_coef,w_Cr(I));
fprintf('located in the %.0f ring, counting from outside in, total of %.0f rings\n',I,
size(Cr,1));

%% Angular Distortion Coefficient DPCPave
a = 0;
b = 0;
c = 0;
w_a = 0;
w_c = 0;

for i =1:size(P02ik_bar,1)
    for k = 1:size(P02ik_bar,2)
        if P02ik_bar(i,k) < P02i_bar(i)
            a = a + P02ik_bar(i,k)/P02i_bar(i);
            b = b + 1;

            Ctheta_P02ik = -1/P02i_bar(i);
            Ctheta_P02i = P02ik_bar(i,k)/(P02i_bar(i)^2);
            w_a = w_a + sqrt((Ctheta_P02ik*w_P02ik)^2 + (Ctheta_P02i*w_P02i)^2);
        else
            a = a + 0;
            b = b + 0;
        end
    end
    if a == 0 && b ==0
        c = c + 1;
    else
        c = c + 1 - (a/b);
        w_c = w_c + w_a/sqrt(k);

    end
    a = 0;
    b = 0;
    w_a = 0;
end
w_c = w_c/sqrt(i);
Ctheta = c/i;
fprintf('Angular distortion coefficient: DPCPave = %.5f +/- %.5f\n',Ctheta, w_c);

%% Total Pressure Coefficient
PI = P02_bar/P_inf;

Pi_P02 = 1/P_inf;
Pi_P01 = -P02_bar/(P_inf^2);

w_Pi = sqrt((Pi_P02*w_P02)^2 + (Pi_P01*w_P01)^2);

fprintf('Total Pressure Loss coefficient: Pi = %.5f +/- %.5f\n',PI,w_Pi);

%% Swirl Index
SI_Index = sum(sum(abs(alpha_AAve)))/A_Total;
SI_U = sum(sum(SI_U_AAve))/A_Total*180/pi;
SI_V = sum(sum(SI_V_AAve))/A_Total*180/pi;

w_SI = sqrt((SI_V*w_vtheta)^2+(SI_U*w_u)^2);
fprintf('Average swirl index: SI = %.5f degrees +/- %.5f \n',SI_Index,w_SI)

%% SWIRL DIRECTIVITY SD
SD = (sum(sum(alpha_AAve))/A_Total)/SI_Index;

w_SS = w_SI;
SS_SD = 1/SI_Index;
SI_SD = -(sum(sum(alpha_AAve))/A_Total)/SI_Index^2;

w_SD = sqrt((SS_SD*w_SS)^2+(SS_SD*w_SS)^2 + (SI_SD*w_SI)^2);

fprintf('Swirl directivity: SD = %.5f +/- %.5f \n',SD,w_SD)

```

```
%% SWIRL PAIRS SP
S = (sum(alpha_AAve))/(A_Total*Angle/(EndAngle+Angle));
S = sort(S);
I = find(S<0);

if sum(abs(S(I(1):I(end)))) > sum(abs(S(I(end)+1:end)))
    a = I(1);
    b = I(end);
else
    a = I(end) + 1;
    b = length(S);
end

SP = SI_Index/(sum(abs(S(a:b)))/(b-a));
SI_SP = 1/sum(abs(S(a:b)));
SS_SP = -SI_Index/sum(abs(S(a:b)))^2;

w_SP = sqrt((SI_SP*w_SI)^2+(b-a)*(SS_SP*w_SS)^2);
fprintf('Swirl Pairs: SP = %.5f +/- %.5f  \n',SP,w_SP)


%% Bulk swirl
BULK = sum(sum(alpha_AAve))/A_Total;

fprintf('Average bulk flow angle: alpha = %.5f degrees +/- %.5f \n',BULK,w_SI)
```

C.3 Internal Aerodynamics Model Contour Plot

```python
import pandas as pd
import numpy as np
import matplotlib.pyplot as plt
import math as mt
from scipy.interpolate import griddata
import matplotlib.image as mpimg
#Ben Gilbart 2024

#File Locations

file1 = ''
file2 = ''
file3 = ''
file4 = ''
file5 = ''
file6 = ''

#Atmospheric pressure [KPa]

P0 = 14.714

#data is read from inner to outer at the AIP
#begin

radii = np.array([0.35355, 0.61235, 0.79055, 0.9354
])
angles = np.array([0, 15, 30, 45, 60, 75])
i_vals = [0, 1, 2, 3, 4, 5]
n_vals = [0, 1, 2, 3]

Txvals = []
Tyvals = []
theta_values = []
r_values = []
pres = []

file_list = [file1, file2, file3, file4, file5,
file6]

#reading pressure data from the 0 deg arm between 0
 and 90 deg
```

```
39 for i in i_vals:
40     for n in n_vals:
41         x_val = mt.cos(mt.radians(angles[i]))*radii
   [n]
42         y_val = mt.sin(mt.radians(angles[i]))*radii
   [n]
43         Txvals.append(x_val)
44         Tyvals.append(y_val)
45         file = file_list[i]
46         p_val = float((pd.read_csv(file_list[i],
   header=None, nrows=1, usecols=[n]).iloc[0, :].
   tolist())[0])
47         pres.append(p_val/P0)
48         theta_values.append(mt.radians(angles[i]))
49         r_values.append(radii[n])
50
51 #reading pressure data from the 90 deg arm between
   90 and 180 deg
52 for i in i_vals:
53     for n in n_vals:
54         x_val = mt.cos(mt.radians(angles[i])+mt.pi/
   2)*radii[n]
55         y_val = mt.sin(mt.radians(angles[i])+mt.pi/
   2)*radii[n]
56         Txvals.append(x_val)
57         Tyvals.append(y_val)
58         file = file_list[i]
59         p_val = float((pd.read_csv(file_list[i],
   header=None, nrows=1, usecols=[n+4]).iloc[0, :].
   tolist())[0])
60         pres.append(p_val / P0)
61         theta_values.append(mt.radians(angles[i])+
   mt.pi/2)
62         r_values.append(radii[n])
63
64 #reading pressure data from the 180 deg arm between
    180 and 270 deg
65 for i in i_vals:
66     for n in n_vals:
67         x_val = mt.cos(mt.radians(angles[i])+mt.pi
   )*radii[n]
```

```
68          y_val = mt.sin(mt.radians(angles[i])+mt.pi
    )*radii[n]
69          Txvals.append(x_val)
70          Tyvals.append(y_val)
71          file = file_list[i]
72          p_val = float((pd.read_csv(file_list[i],
    header=None, nrows=1, usecols=[n+8]).iloc[0, :].
    tolist())[0])
73          pres.append(p_val / P0)
74          theta_values.append(mt.radians(angles[i
    ]) + mt.pi)
75          r_values.append(radii[n])
76
77  #reading pressure data from the 270 deg arm
    between 270 and 360 deg
78  for i in i_vals:
79      for n in n_vals:
80          x_val = mt.cos(mt.radians(angles[i])+3*mt.
    pi/2)*radii[n]
81          y_val = mt.sin(mt.radians(angles[i])+3*mt.
    pi/2)*radii[n]
82          Txvals.append(x_val)
83          Tyvals.append(y_val)
84          file = file_list[i]
85          p_val = float((pd.read_csv(file_list[i],
    header=None, nrows=1, usecols=[n+12]).iloc[0, :].
    tolist())[0])
86          pres.append(p_val / P0)
87          theta_values.append(mt.radians(angles[i
    ]) + 3*mt.pi / 2)
88          r_values.append(radii[n])
89
90  middlep = (pres[0]+pres[4]+pres[8]+pres[12]+pres[
    16]+pres[20]+pres[24]+pres[28]+pres[32]+pres[36]+
    pres[40]+pres[44]+pres[48]+pres[52]+pres[56]+pres[
    60]+pres[64]+pres[68]+pres[72]+pres[76]+pres[80]+
    pres[84]+pres[88]+pres[92])/24
91  pres.append(middlep)
92  r_values.append(0)
93  Txvals.append(0)
94  Tyvals.append(0)
```

```
 95
 96 # Create a regular grid in polar coordinates
 97 theta_grid, r_grid = np.meshgrid(np.linspace(0, 2*
    np.pi, 100), np.linspace(0, max(r_values), 400))
 98
 99 # Convert polar grid to Cartesian coordinates
100 x_grid = r_grid * np.cos(theta_grid)
101 y_grid = r_grid * np.sin(theta_grid)
102
103 # Perform 2D interpolation using griddata
104 z_grid = griddata((Txvals, Tyvals), pres, (x_grid
    , y_grid), method='cubic')
105
106 #limit the data
107 z_grid = np.clip(z_grid, 0.7, 1.0)
108
109 # Create a polar contour plot for interpolated
    data
110 fig, ax = plt.subplots(subplot_kw={'projection': '
    polar'})
111 contour_levels = np.linspace(0.7, 1, 130)
112 contour = ax.contourf(theta_grid, r_grid, z_grid,
    cmap='jet', levels=contour_levels, vmin = 0.7,
    vmax = 1)
113
114 # Add colorbar for contour plot
115 colorbar_contour = plt.colorbar(contour, label='
    Pressure recovery', orientation='vertical', shrink
     = 0.6, pad=0.1)
116 colorbar_contour.set_ticks([0.7, 0.75, 0.8, 0.85,
    0.90, 0.95, 1.0])
117
118 # Set label orientation to be horizontal along the
     top
119 colorbar_contour.set_label('$\overline{\pi}$',
    rotation=0, labelpad=-35, y=1.1, fontsize = 15)
120
121 ax.set_yticklabels([])  # Remove radial axis
    labels
122 ax.set_yticks([])  # Remove radial axis ticks
123
```

```
124 #orientation
125 img_ax = fig.add_axes([0.7, 0.77, 0.25, 0.25])
126 img = mpimg.imread('')  #path to image
127 img_ax.imshow(img)
128 img_ax.axis('off')
129
130 ax.set_theta_offset(np.pi/2)  # Offset angle to
    start from the top
131 ax.set_theta_direction(-1)
132
133 # Show the plot
134 plt.show()
135
```

C.4 Internal Aerodynamics Model Coefficients

```
 1 import pandas as pd
 2 import numpy as np
 3 import math as mt
 4 #Ben Gilbart 2024
 5
 6 #File Locations (in order from 0 to 75 degrees)
 7
 8 file1 = ''
 9 file2 =''
10 file3 =''
11 file4 =''
12 file5 =''
13 file6 =''
14
15 P0 = 14.714 #Atmospheric pressure [psi]
16 Ps = 13.546 #static pressure [psi]
17 Psstddev = 0.047307085 #static pressure stndard
   deviation[psi]
18
19 #uncertainties
20
21 dP0 = 0.0145038
22
23 #data is read from the inner to the outer at the
   AIP
24
25 #begin
26
27 radii = np.array([0.35355, 0.61235, 0.79055, 0.9354
   ])
28 angles = np.array([0, 15, 30, 45, 60, 75])
29 i_vals = [0, 1, 2, 3, 4, 5]
30 n_vals = [0, 1, 2, 3]
31
32 theta_values = []
33 r_values = []
34 pres = []
35 stndevs = []
36
37 file_list = [file1, file2, file3, file4, file5,
   file6]
```

```
38
39 orderedpres = np.zeros((24, 4))
40 orderedsigma = np.zeros((24, 4))
41
42 #reading pressure data from the 0 deg arm between 0
    and 90 deg
43 for i in i_vals:
44     for n in n_vals:
45         file = file_list[i]
46         pres.append(float((pd.read_csv(file_list[i
   ], header=None, nrows=1, usecols=[n]).iloc[0, :].
   tolist())[0]))
47         stndevs.append(float((pd.read_csv(file_list
   [i], header=None, nrows=2, usecols=[n]).iloc[1, :].
   tolist())[0]))
48         theta_values.append(mt.radians(angles[i]))
49         r_values.append(radii[n])
50         orderedpres[i, n] = float((pd.read_csv(
   file_list[i], header=None, nrows=1, usecols=[n]).
   iloc[0, :].tolist())[0])
51         orderedsigma[i, n] = float((pd.read_csv(
   file_list[i], header=None, nrows=2, usecols=[n]).
   iloc[1, :].tolist())[0])
52
53 #reading pressure data from the 90 deg arm between
   90 and 180 deg
54 for i in i_vals:
55     for n in n_vals:
56         file = file_list[i]
57         pres.append(float((pd.read_csv(file_list[i
   ], header=None, nrows=1, usecols=[n+4]).iloc[0, :].
   tolist())[0]))
58         stndevs.append(float((pd.read_csv(file_list
   [i], header=None, nrows=2, usecols=[n]).iloc[1, :].
   tolist())[0]))
59         theta_values.append(mt.radians(angles[i])+
   mt.pi/2)
60         r_values.append(radii[n])
61         orderedpres[i+6, n] = float((pd.read_csv(
   file_list[i], header=None, nrows=1, usecols=[n+4]).
   iloc[0, :].tolist())[0])
```

```
62          orderedsigma[i+6, n] = float((pd.read_csv(
   file_list[i], header=None, nrows=2, usecols=[n]).
   iloc[1, :].tolist())[0])
63
64 #reading pressure data from the 180 deg arm
   between 180 and 270 deg
65 for i in i_vals:
66      for n in n_vals:
67          file = file_list[i]
68          pres.append(float((pd.read_csv(file_list[i
   ], header=None, nrows=1, usecols=[n+8]).iloc[0
   , :].tolist())[0]))
69          stndevs.append(float((pd.read_csv(
   file_list[i], header=None, nrows=2, usecols=[n]).
   iloc[1, :].tolist())[0]))
70          theta_values.append(mt.radians(angles[i
   ]) + mt.pi)
71          r_values.append(radii[n])
72          orderedpres[i+12, n] = float((pd.read_csv(
   file_list[i], header=None, nrows=1, usecols=[n+8
   ]).iloc[0, :].tolist())[0])
73          orderedsigma[i+12, n] = float((pd.read_csv
   (file_list[i], header=None, nrows=2, usecols=[n]).
   iloc[1, :].tolist())[0])
74
75 #reading pressure data from the 270 deg arm
   between 270 and 360 deg
76 for i in i_vals:
77      for n in n_vals:
78          file = file_list[i]
79          pres.append(float((pd.read_csv(file_list[i
   ], header=None, nrows=1, usecols=[n+12]).iloc[0
   , :].tolist())[0]))
80          stndevs.append(float((pd.read_csv(
   file_list[i], header=None, nrows=2, usecols=[n]).
   iloc[1, :].tolist())[0]))
81          theta_values.append(mt.radians(angles[i
   ]) + 3*mt.pi / 2)
82          r_values.append(radii[n])
83          orderedpres[i+18, n] = float((pd.read_csv(
   file_list[i], header=None, nrows=1, usecols=[n+12
```

```
 83 ]).iloc[0, :].tolist())[0])
 84         orderedsigma[i+18, n] = float((pd.read_csv
    (file_list[i], header=None, nrows=2, usecols=[n]).
    iloc[1, :].tolist())[0])
 85
 86 # Total pressure recovery
     ------------------------------------------------
    ------------------------------------------------
    ----
 87
 88 P02 = sum(pres) / len(pres)
 89 sigmaP02 = sum(stndevs) / len(stndevs)
 90 pibar= P02/P0
 91 epibar = mt.sqrt((P02/(-P0**2)*dP0)**2 + (1/P0*mt.
    sqrt(sigmaP02**2+(0.0005*P02)**2))**2)
 92
 93 eloss = mt.sqrt((-1*epibar)**2)
 94
 95 print(f"Total pressure recovery = {round(pibar, 4)
    } +- {round(epibar,5)}")
 96 print(f"Total pressure loss = {round(1-pibar, 4)}
     +- {round(eloss,5)}")
 97
 98 #DPRPmax
     ------------------------------------------------
    ------------------------------------------------
    ----
 99
100 r1 = []
101 r2 = []
102 r3 = []
103 r4 = []
104
105 s1 = []
106 s2 = []
107 s3 = []
108 s4 = []
109 ringstdev = []
110 Avgringpres = []
111 DPRP =[]
112
```

```
113 #data put into a matrix with radial position first
     column, angular position second collumn, pressure
     value 3rd collumn, stdev 4th collumn
114 matrix = np.hstack((np.array(r_values).reshape(-1
    , 1), np.array(theta_values).reshape(-1, 1), np.
    array(pres).reshape(-1, 1), np.array(stndevs).
    reshape(-1, 1)))
115
116 for row in matrix:
117     if row[0] == radii[0]:
118         r1.append(row[2])
119         s1.append(row[3])
120     elif row[0] == radii[1]:
121         r2.append(row[2])
122         s2.append(row[3])
123     elif row[0] == radii[2]:
124         r3.append(row[2])
125         s3.append(row[3])
126     elif row[0] == radii[3]:
127         r4.append(row[2])
128         s4.append(row[3])
129
130 # avg ring pressures from inner ring to outer ring
131 Avgringpres.append(sum(r1) / len(r1))
132 Avgringpres.append(sum(r2) / len(r2))
133 Avgringpres.append(sum(r3) / len(r3))
134 Avgringpres.append(sum(r4) / len(r4))
135
136 ringstdev.append(sum(s1) / len(s1))
137 ringstdev.append(sum(s2) / len(s2))
138 ringstdev.append(sum(s3) / len(s3))
139 ringstdev.append(sum(s4) / len(s4))
140
141 for value in Avgringpres:
142     DPRP.append((P02-value)/P02)
143
144 P0i = np.argmin(Avgringpres)
145
146 sigmaP0i = ringstdev[np.argmax(DPRP)]
147
148 eDPRP = mt.sqrt((P0i/(P02**2)*mt.sqrt(sigmaP02**2
```

```
148 +(0.0005*P02)**2))**2 + (-1/P02*mt.sqrt(sigmaP0i**
    2+(0.0005*P0i)**2))**2)
149
150 print(f'The DPRPmax is {round(DPRP[np.argmax(DPRP
    )], 4)} +- {round(eDPRP, 4)} located in ring
    number {np.argmax(DPRP)+1} from the centre')
151
152 #DPCPavg
     ------------------------------------------------
    ------------------------------------------------
    ----
153
154 intvals = []
155 n1 = []
156 d1 = []
157 n2 = []
158 d2 = []
159 n3 = []
160 d3 = []
161 n4 = []
162 d4 = []
163
164 #uncertainty arrays
165
166 AN = []
167 AD = []
168 BN = []
169 BD = []
170 CN = []
171 CD = []
172 DN = []
173 DD = []
174
175 #combining the pressure values from each ring into
     a single matrix where each collumn represents a
    ring from left to right inner to outer
176 ring_pres_vals= np.hstack((np.array(r1).reshape(-1
    , 1), np.array(r2).reshape(-1, 1), np.array(r3).
    reshape(-1, 1), np.array(r4).reshape(-1, 1)))
177
178 ring_stdev_vals= np.hstack((np.array(s1).reshape(-
```

```
178 1, 1), np.array(s2).reshape(-1, 1), np.array(s3).
    reshape(-1, 1), np.array(s4).reshape(-1, 1)))
179
180 #indexes through each pressure value within a
    given ring and appends a value for the numerator
    or denomenator, repeats for all rings
181 for col_index in range(len(ring_pres_vals[0])):
182     for row_index in range(len(ring_pres_vals)):
183             if col_index == 0:
184                 if ring_pres_vals[row_index][
    col_index] < Avgringpres[col_index]:
185                     n1.append(ring_pres_vals[
    row_index][col_index]/Avgringpres[col_index])
186                     d1.append(1)
187                     AN.append(mt.sqrt((1/(
    Avgringpres[col_index])*mt.sqrt(ringstdev[
    col_index]**2+(0.0005*P02)**2))**2 + (-
    ring_pres_vals[row_index][col_index]/(Avgringpres[
    col_index]**2)*mt.sqrt(ring_stdev_vals[row_index][
    col_index]**2 + (0.0005*P02)**2))**2))
188                     AD.append(0)
189                 elif ring_pres_vals[row_index][
    col_index] >= Avgringpres[col_index]:
190                     n1.append(0)
191                     d1.append(0)
192                     AN.append(0)
193                     AD.append(0)
194
195             elif col_index == 1:
196                 if ring_pres_vals[row_index][
    col_index] < Avgringpres[col_index]:
197                     n2.append(ring_pres_vals[
    row_index][col_index] / Avgringpres[col_index])
198                     d2.append(1)
199                     BN.append(mt.sqrt((1/(
    Avgringpres[col_index])*mt.sqrt(ringstdev[
    col_index]**2+(0.0005*P02)**2))**2 + (-
    ring_pres_vals[row_index][col_index]/(Avgringpres[
    col_index]**2)*mt.sqrt(ring_stdev_vals[row_index][
    col_index]**2 + (0.0005*P02)**2))**2))
200                     BD.append(0)
```

```
201                 elif ring_pres_vals[row_index][
    col_index] >= Avgringpres[col_index]:
202                     n2.append(0)
203                     d2.append(0)
204                     BN.append(0)
205                     BD.append(0)
206 
207             elif col_index == 2:
208                 if ring_pres_vals[row_index][
    col_index] < Avgringpres[col_index]:
209                     n3.append(ring_pres_vals[
    row_index][col_index] / Avgringpres[col_index])
210                     d3.append(1)
211                     CN.append(mt.sqrt((1/(
    Avgringpres[col_index])*mt.sqrt(ringstdev[
    col_index]**2+(0.0005*P02)**2))**2 + (-
    ring_pres_vals[row_index][col_index]/(Avgringpres[
    col_index]**2)*mt.sqrt(ring_stdev_vals[row_index][
    col_index]**2 + (0.0005*P02)**2))**2))
212                     CD.append(0)
213                 elif ring_pres_vals[row_index][
    col_index] >= Avgringpres[col_index]:
214                     n3.append(0)
215                     d3.append(0)
216                     CN.append(0)
217                     CD.append(0)
218 
219             elif col_index == 3:
220                 if ring_pres_vals[row_index][
    col_index] < Avgringpres[col_index]:
221                     n4.append(ring_pres_vals[
    row_index][col_index] / Avgringpres[col_index])
222                     d4.append(1)
223                     DN.append(mt.sqrt((1/(
    Avgringpres[col_index])*mt.sqrt(ringstdev[
    col_index]**2+(0.0005*P02)**2))**2 + (-
    ring_pres_vals[row_index][col_index]/(Avgringpres[
    col_index]**2)*mt.sqrt(ring_stdev_vals[row_index][
    col_index]**2 + (0.0005*P02)**2))**2))
224                     DD.append(0)
225                 elif ring_pres_vals[row_index][
```

```
225 col_index] >= Avgringpres[col_index]:
226                     n4.append(0)
227                     d4.append(0)
228                     DN.append(0)
229                     DD.append(0)
230
231 val1 = 1 - sum(n1)/sum(d1)
232 val2 = 1 - sum(n2)/sum(d2)
233 val3 = 1 - sum(n3)/sum(d3)
234 val4 = 1 - sum(n4)/sum(d4)
235
236 DPCPavg = 1/4 * (val1+val2+val3+val4)
237
238 EN1 = np.sqrt(np.sum(np.array(AN)**2))
239 ED1 = np.sqrt(np.sum(np.array(AD)**2))
240
241 EN2 = np.sqrt(np.sum(np.array(BN)**2))
242 ED2 = np.sqrt(np.sum(np.array(BD)**2))
243
244 EN3 = np.sqrt(np.sum(np.array(CN)**2))
245 ED3 = np.sqrt(np.sum(np.array(CD)**2))
246
247 EN4 = np.sqrt(np.sum(np.array(DN)**2))
248 ED4 = np.sqrt(np.sum(np.array(DD)**2))
249
250
251 ER1 = mt.sqrt((-1/sum(d1)*EN1)**2 + (sum(n1)/(sum(
    d1)**2)*ED1)**2)
252 ER2 = mt.sqrt((-1/sum(d2)*EN2)**2 + (sum(n2)/(sum(
    d2)**2)*ED2)**2)
253 ER3 = mt.sqrt((-1/sum(d3)*EN3)**2 + (sum(n3)/(sum(
    d3)**2)*ED3)**2)
254 ER4 = mt.sqrt((-1/sum(d4)*EN4)**2 + (sum(n4)/(sum(
    d4)**2)*ED4)**2)
255
256 EDPCP = mt.sqrt((0.25*ER1)**2 + (0.25*ER2)**2 + (0
    .25*ER3)**2 + (0.25*ER4)**2)
257
258 print(f'DPCPavg = {round(DPCPavg,4)} +- {round(
    EDPCP, 5)}')
259
```

```
260 # DC(60
    ) ----------------------------------------------
    ----------------------------------------------
    -----
261
262 # stitch two copies of ordered (by angle) pressure
     array in order to determine if the DC(60) occurs
    at the end of the data ie 0 deg area
263 doubled_matrix = np.vstack((orderedpres,
    orderedpres.copy()))
264 doubled_sigmamatrix = np.vstack((orderedsigma,
    orderedsigma.copy()))
265
266 # Initialize variables to track minimum average
    and corresponding indices
267 min_average = float('inf')
268 min_indices = None
269
270 # Iterate through the matrix to find the minimum
    average
271 for row_start in range(48-3):
272     current_average = np.mean(doubled_matrix[
    row_start:row_start+4, 0:4])
273     current_sigma = np.mean(doubled_sigmamatrix[
    row_start:row_start+4, 0:4])
274     if current_average < min_average:
275         min_average = current_average
276         sigmaP0j = current_sigma
277         min_indices = (row_start, row_start+3)
278
279 if min_indices[1] > 23:
280     indexend = min_indices[1]-24
281 else:
282     indexend = min_indices[1]
283
284 DC60 = (P02-min_average)/(P02-Ps)
285
286 eDC60 = mt.sqrt(((min_average-Ps)/((P02-Ps)**2)*mt
    .sqrt(sigmaP02**2 + (0.0005*P02)**2))**2 + (-1/(
    P02-Ps)*mt.sqrt(sigmaP0j**2 + (0.0005*P02)**2))**2
     + (-(-1*(P02-min_average)/((P02-Ps)**2))*mt.sqrt(
```

```
286 Psstddev**2+(0.0005*Ps)**2))**2)
287
288 print(f"DC(60) = {round(DC60, 5)} +- {round(eDC60
    , 5)} occuring between {min_indices[0]*15} degrees
     and {indexend*15+15} degrees looking upstream")
289
290
291
292
293
```